Karlsruhe Institute of Technology

Magnetic ordering in the Kondo lattice

Zur Erlangung des akademischen Grades eines

Doktors der Naturwissenschaften

von der KIT-Fakultät für Physik
des Karlsruher Instituts für Technologie (KIT)

genehmigte

Dissertation

von

Matthias Keßler, M. Sc.

Tag der mündlichen Prüfung: 10. Februar 2023
1. Referent: Priv.-Doz. Dr. Robert Eder
2. Korreferent: Prof. Dr. Jörg Schmalian

Abstract

Although the complicated interaction between electrons makes it impossible to directly calculate the properties of realistic condensed systems, for large classes of metallic compounds this problem has essentially been "solved": their behavior is qualitatively described by Landau's *Fermi liquid theory* (which postulates that the electron interaction ultimately amounts to little more than a readjustment of a few numerical parameters compared to a noninteracting system), and approximations based on *density functional theory* (which describes the system not through individual electrons, but only through the total electron density) are always increasing in quantitative accuracy.

However, for other materials (known under the umbrella term of *strongly correlated*) these general-purpose methods can fail, sometimes even spectacularly. While such systems have been known for almost a hundred years, they have only more recently come to the forefront of research with the discovery of high-temperature superconductors in the 1980s. Since then, these materials have mostly evaded theoretical understanding. Not quite as well-known, but equally interesting and difficult to explain are *heavy fermion systems*, which form the subject of this thesis in the form of the much simplified *Kondo lattice model* (KLM). To deal with the strong interactions in the system, we use a specialized ansatz tuned to the specifics of the model, the *bond fermion method*, which allows for the calculation of quasiparticle dynamics and magnetic properties.

The structure of the thesis is as follows: Chapter 1 gives a basic introduction into Kondo physics, heavy fermion systems, and the KLM. Chapter 2 then presents the bond fermion method. We extend the method by combining it with the *Gutzwiller approximation*, and then apply it to the KLM on a square lattice in Chapters 3 and 4. Finally, in Chapter 5 we investigate the effect of *geometric frustration* by performing a similar calculation on the triangular lattice. Chapter 6 forms the conclusion.

Some elements of this thesis are based on published articles, for which the thesis author acted as first author and contributed a significant majority of the work. Parts of Chapter 2 (specifically, Secs. 2.4, 2.5, and 2.7) and Chapter 3 are based on Ref. [57]. Chapter 5 is based on Ref. [56].

Contents

1 Introduction to Kondo physics and heavy fermions

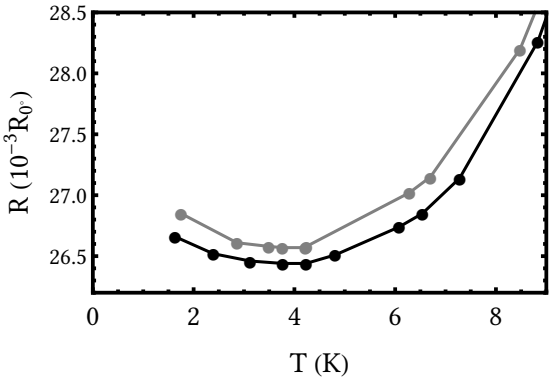

Figure 1.1: The resistance of two Au samples measured by de Haas et al., normalized to the resistance at 0°C [29].

1.1 Kondo effect

This thesis is aimed at theoretical study of heavy fermion systems. However, we will first give a short introduction into the related topic of dilute magnetic impurities in nonmagnetic host metals. This serves to introduce many of the concepts important for heavy fermion compounds (for example *Kondo screening*) in a simpler setting. Furthermore, this gives some historical context and motivation for the continued study of heavy fermions and other strongly correlated materials. The content of this section is based on Hewson's much more comprehensive treatment [47].

1.1.1 Resistance minimum

It was first discovered by de Haas et al. [29] that the electrical resistivity of (impure) gold samples shows an unexpected minimum at a low but finite temperature (Fig. 1.1). As was common knowledge at the time, the two most important sources of electrical resistivity are impurity scattering (ρ_{imp}) and electron-phonon scattering (ρ_{ph}), while electron-electron scattering ($\rho_{\text{e-e}}$) is significant at low temperatures. None of these mechanisms are expected to behave non-monotonically: in the usual case, ρ_{imp} is almost independent

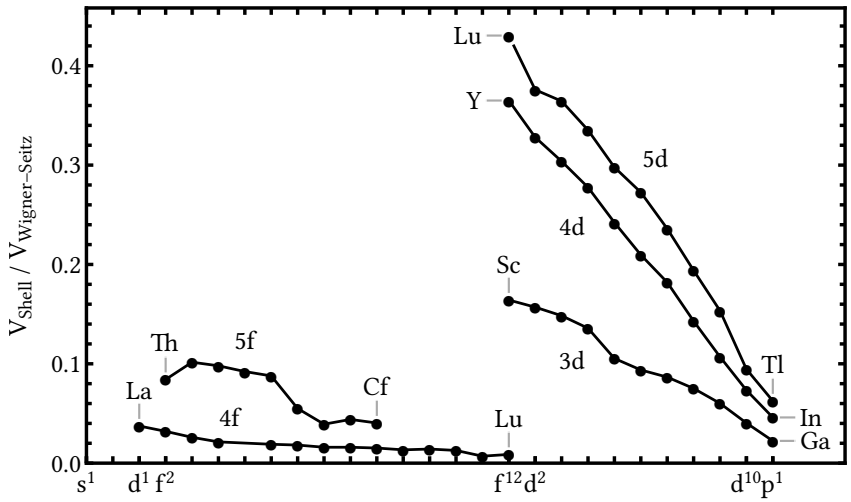

Figure 1.2: Ratio of the atomic d- (f-) shell volume and the Wigner-Seitz cell volume in a solid, as compiled by van der Marel and Sawatzky [74].

of temperature, while the number of thermally excited phonons and the phase space available for electron-electron scattering (and thus ρ_{ph} and $\rho_{\mathrm{e-e}}$) is proportional to some power of T. As a consequence, the resistance minimum remained a mystery for several decades.

Later research found that the existence of a resistance minimum was correlated with the appearance of magnetic impurities formed by transition metals, which can be detected by their a characteristic Curie-Weiss contribution to the magnetic susceptibility ($\chi_{\mathrm{CW}} \propto 1/T$). For example, in series of Mo-Nb alloys, the strength of the (Fe-impurity) magnetic moment showed a clear relation to the size of the resistance minimum [23, 99]. Once the experimental link between magnetism and resistance anomaly was experimentally established, Kondo [60] quickly provided a simple theoretical calculation explaining the minimum. We will retrace this calculation shortly, but first we must discuss the origin of the magnetic moments and their interaction with the conduction electrons.

1.1.2 Anderson and Kondo impurity models

The local magnetic moments responsible for the resistance minimum are a consequence of *strong correlation*, which forms a large and diverse research topic. Going back to the very beginnings of the subject, the elements most often associated with such phenomena are transition metals and rare earths; for example, the transition metal oxide NiO was the first compound found to be a *Mott insulator*, a system expected to conduct based on band theory but insulating in practice [18]. Much later, high-temperature superconductivity was first discovered by Bednorz and Müller in compounds featuring strongly correlated copper oxide layers [14].

The reason for these extraordinary features lies in the strong Coulomb repulsion associated with these elements. In compounds, transition metals[1] (rare earths) exhibit partially filled 3d- (4f-) shells of relatively small spatial extent when compared to the inter-ionic lattice constant. As shown in Fig. 1.2, this ratio generally trends downwards towards the right of the periodic table due to the increased nuclear charge (and decreased atomic radius). However, the 3d-series Sc-Ga (4f-series La-Lu) have noticeably smaller shells than other d- (f-) elements. Roughly speaking, this is because 3d and 4f shells are the lowest-energy states with $l = 2$ or $l = 3$, respectively. Their electron wave functions are thus already orthogonal to those of the lower-lying electrons due to their angular wave functions $Y_{l,m}$, so that the radial wave function can be compressed further.

The strongly correlated nature of these orbital results in the formation of local magnetic moments analogous to Hund's rule in the gaseous phase. The special feature here is that the 3d- or 4f-orbitals are sufficiently close in energy to the rest of the conduction band that hybridization effects appear: there is thus a competition between the local (effectively magnetic) interaction and tunneling. The simplest model that includes both of these phenomena is the *Anderson impurity model* [5].

Forgetting about the orbital degeneracy associated with the quantum number m and taking only a single band of conduction electrons, we can model a transition metal or rare earth impurity by the Hamiltonian

$$H_{\text{Anderson}} = H_t + H_V + H_f, \tag{1.1}$$

$$H_t = \sum_{\mathbf{k}\sigma} \epsilon_{\mathbf{k}} c^\dagger_{\mathbf{k}\sigma} c_{\mathbf{k}\sigma}, \tag{1.2}$$

$$H_V = \frac{1}{\sqrt{N}} \sum_{\mathbf{k}\sigma} \left[V_{\mathbf{k}} f^\dagger_\sigma c_{\mathbf{k}\sigma} + \text{h.c.} \right], \tag{1.3}$$

$$H_f = \epsilon_f \sum_\sigma f^\dagger_\sigma f_\sigma + U f^\dagger_\uparrow f_\uparrow f^\dagger_\downarrow f_\downarrow. \tag{1.4}$$

Here, $c^\dagger_{\mathbf{k}\sigma}$ creates a conduction electron with momentum $\mathbf{k}$ and spin σ. $\epsilon_{\mathbf{k}}$ is the band energy describing the hopping. $f^\dagger_\sigma$ creates an impurity electron[2]. N is the total number of sites (or equivalently, the total number of allowed momenta $\mathbf{k}$). ϵ_f is the energy of the localized orbital, and U models the Coulomb interaction of the partially filled shell. Note that conduction electrons are assumed to have negligible interaction, or can be thought of as already renormalized in the Fermi liquid sense. $V_{\mathbf{k}}$ describes the hybridization strength between conduction electron and the f-level.

The correlation effects in the system are caused by the interplay of U and $V_{\mathbf{k}}$. If $U = 0$, the system is non-interacting and the ground state is a Slater determinant wave function.

[1] Here meaning specifically 3d-elements.

[2] We call this an f-electron for consistency with later chapters, which will mostly concern themselves with rare earth compounds.

If $V_{\mathbf{k}} = 0$ ($H_V = 0$), the f-orbital is completely decoupled and can easily be solved. The eigenstates of H_f have zero, one, or two electrons, with eigenvalues

$$H_f |0\rangle = 0, \tag{1.5}$$

$$H_f |\sigma\rangle = \epsilon_f, \tag{1.6}$$

$$H_f |\uparrow\downarrow\rangle = E_{\uparrow\downarrow} |0\rangle = \left(2\epsilon_f + U\right) |\uparrow\downarrow\rangle . \tag{1.7}$$

Depending on the values of ϵ_f and U, any of these states can be the ground state of the system.

With hybridization turned on, the Anderson impurity is highly nontrivial. While there are some exact numerical solutions [48, 114] (and even analytic results using the Bethe ansatz [108]), we will only perform some much simpler calculations. As we are mostly interested in magnetic effects, the Anderson Hamiltonian can be simplified: following Schrieffer and Wolff [47, 100], we will isolate the spin interactions of the system to arrive at the *Kondo impurity model*.

We first specialize to the most interesting parameter region of the Anderson model. Assuming that the ground state of the f-orbital is widely separated from its excited states (small $V_{\mathbf{k}}$), charge fluctuations are strongly suppressed and any excitations of the f-orbital are very short-lived. If the ground state is either $|0\rangle$ or $|\uparrow\downarrow\rangle$, this is where the story ends: simple perturbation theory will give adequate results, as the f-orbital is effectively non-dynamic. In contrast, when $|\sigma\rangle$ is the ground state, we have a remaining spin degeneracy: even if the charge excitations themselves are short-lived, there are two possible ground states to return to, so that the f-orbital is still dynamic. A specific choice of parameters that achieves this is the *symmetric Anderson model* with

$$U \gg |V_{\mathbf{k}}|, \tag{1.8}$$

$$\epsilon_f = -\frac{U}{2}. \tag{1.9}$$

Due to the ground state degeneracy, simple perturbation theory fails (note that there is no matrix element linking $|\uparrow\rangle$ and $|\downarrow\rangle$ directly). However, we can still use the smallness of $V_{\mathbf{k}}$ to our advantage, using the *Schrieffer-Wolff transformation*. Up to second order in $V_{\mathbf{k}}$, there are two types of fluctuations (shown in Fig. 1.3): the f-electron can tunnel into the conduction band (intermediate state $|0\rangle$) with its place then taken by a c-electron, or the c- and f-electrons tunnel in the opposite order (intermediate state $|\uparrow\downarrow\rangle$). As demonstrated, this can induce a spin-flip of the localized and the conduction electrons; we should accordingly expect a spin-spin interaction to remain even if the charge dynamics of the f-orbital are suppressed by the interaction.

Following Hewson, we formulate the Schrieffer-Wolff transformation by examining the Schrödinger equation in matrix form:

$$H_{\text{Anderson}} |\Psi\rangle = E |\Psi\rangle \Leftrightarrow \begin{pmatrix} H_0 & H_{0\sigma} & 0 \\ H_{\sigma 0} & H_\sigma & H_{\sigma\uparrow\downarrow} \\ 0 & H_{\uparrow\downarrow\sigma} & H_{\uparrow\downarrow} \end{pmatrix} = E \begin{pmatrix} |\Psi_0\rangle \\ |\Psi_\sigma\rangle \\ |\Psi_{\uparrow\downarrow}\rangle \end{pmatrix}. \tag{1.10}$$

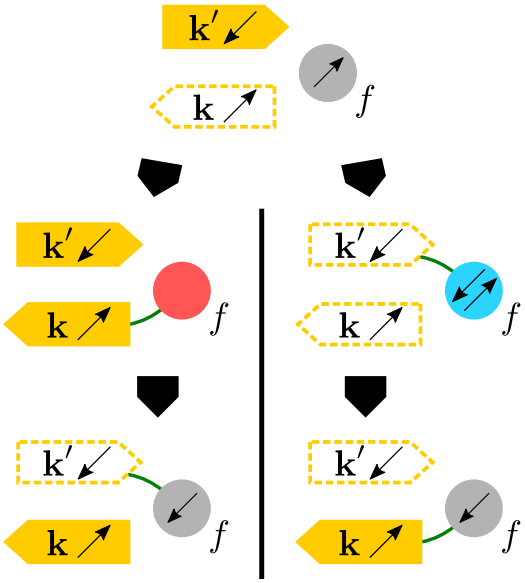

Figure 1.3: Spin-flip scattering on an Anderson impurity through a second-order process. An incoming $|\mathbf{k}' \downarrow\rangle$-electron (full yellow arrow) is scattered into the unoccupied $|\mathbf{k} \uparrow\rangle$-state (dashed yellow arrow). Hopping processes are denoted by a green line. On the left side, the intermediate (middle) state has has an empty f-orbital (red). On the right side, the intermediate state has a double occupation (blue). The final (bottom) state is the same in both cases, with the spin of the f-electron flipped compared to the starting state.

We have explicitly split the Hamiltonian and the wave function depending on the occupation of the f-orbital. The diagonal elements (H_0, etc.) correspond to H_t and H_f, as they leave each subspace invariant, while the off-diagonal ones ($H_{0\sigma}$, etc.) correspond to H_V, which changes the f-occupation. We can solve the Schrödinger equation for $|\Psi_0\rangle$ and $|\Psi_{\uparrow\downarrow}\rangle$ and reinsert them, which gives

$$\left[H_\sigma + H_{\sigma 0}\frac{1}{E - H_0}H_{0\sigma} + H_{\sigma\uparrow\downarrow}\frac{1}{E - H_{\uparrow\downarrow}}H_{\uparrow\downarrow\sigma}\right]|\Psi_\sigma\rangle = E\,|\Psi_\sigma\rangle\,. \tag{1.11}$$

The first term in the bracket is the unperturbed Hamiltonian, while the other two correspond to each of the (short-lived) excitations mentioned above. As E appears on both sides, we have not yet simplified anything. For this we write

$$H_{\sigma 0}\frac{1}{E - H_0}H_{0\sigma}|\Psi_\sigma\rangle = \frac{1}{N}\sum_{\mathbf{k}\sigma\mathbf{k}'\sigma'} V_\mathbf{k} f_\sigma^\dagger c_{\mathbf{k}\sigma}\frac{1}{E - H_0}V_{\mathbf{k}'}^* c_{\mathbf{k}'\sigma'}^\dagger f_{\sigma'}|\Psi_\sigma\rangle \tag{1.12}$$

$$= \frac{1}{N}\sum_{\mathbf{k}\sigma\mathbf{k}'\sigma'}\frac{V_\mathbf{k} V_{\mathbf{k}'}^*}{\epsilon_f - \epsilon_{\mathbf{k}'}} f_\sigma^\dagger c_{\mathbf{k}\sigma} c_{\mathbf{k}'\sigma'}^\dagger f_{\sigma'}|\Psi_\sigma\rangle + O(V_\mathbf{k}^4). \tag{1.13}$$

We have simplified the denominator through

$$(H_0 - E)c_{\mathbf{k}'\sigma'}^\dagger f_{\sigma'}|\Psi_\sigma\rangle = (\epsilon_{\mathbf{k}'} - \epsilon_f)c_{\mathbf{k}'\sigma'}^\dagger f_{\sigma'}|\Psi_\sigma\rangle + O(V_\mathbf{k}^2), \tag{1.14}$$

as to zeroth order $|\Psi_\sigma\rangle$ is an eigenstate of H_σ (with an unperturbed Fermi sea and a singly occupied f-orbital) and E the unperturbed energy, so the change in energy $(H_0 - E)$ after applying $c^\dagger_{\mathbf{k}'\sigma'} f_{\sigma'}$ comes from adding the c-electron $(+\epsilon_{\mathbf{k}'})$ and removing the f-electron $(-\epsilon_f)$. This approximation is valid as long as ϵ_f is well-separated from $\epsilon_{\mathbf{k}}$, note the divergence in (1.13) otherwise.

A similar computation for the $H_{\Uparrow\Downarrow}$-term leads to the *Kondo* (or *s-d*) *impurity model* [47]

$$H_{\text{Kondo}} = H_t + H_J + H_K, \tag{1.15}$$

$$H_J = \frac{1}{N}\sum_{\mathbf{k}\mathbf{k}'} J_{\mathbf{k}\mathbf{k}'} \mathbf{S}^c_{\mathbf{k}\mathbf{k}'} \mathbf{S}^f, \tag{1.16}$$

$$H_K = \frac{1}{N}\sum_{\mathbf{k}\mathbf{k}'} K_{\mathbf{k}\mathbf{k}'} c^\dagger_{\mathbf{k}} c_{\mathbf{k}'}, \tag{1.17}$$

$$J_{\mathbf{k}\mathbf{k}'} = 2V^*_{\mathbf{k}} V_{\mathbf{k}'} \left[\frac{1}{\epsilon_{\mathbf{k}} - \epsilon_f} + \frac{1}{U + \epsilon_f - \epsilon_{\mathbf{k}'}}\right], \tag{1.18}$$

$$K_{\mathbf{k}\mathbf{k}'} = \frac{V^*_{\mathbf{k}'} V_{\mathbf{k}}}{2} \left[\frac{1}{\epsilon_{\mathbf{k}} - \epsilon_f} - \frac{1}{U + \epsilon_f - \epsilon_{\mathbf{k}'}}\right], \tag{1.19}$$

$$c_{\mathbf{k}} = \begin{pmatrix} c_{\mathbf{k}\uparrow} & c_{\mathbf{k}\downarrow} \end{pmatrix}^\intercal, \tag{1.20}$$

$$\mathbf{S}^c_{\mathbf{k}\mathbf{k}'} = c^\dagger_{\mathbf{k}} \frac{\boldsymbol{\tau}}{2} c_{\mathbf{k}'}. \tag{1.21}$$

H_t remains unchanged from the Anderson Hamiltonian, wheres H_J and H_K respectively describe the spin-dependent and spin-independent scattering (H_J is the *Kondo interaction*). $\boldsymbol{\tau}$ is the vector of Pauli matrices, so that $\mathbf{S}^c_{\mathbf{k}\mathbf{k}'}$ describes the conduction electron spin ($\mathbf{S}^f$ is defined analogously for the localized electron).

Usually, one assumes that $|\epsilon_f|$ and U are much greater than the bandwidth of conduction electrons, so that we can neglect $\epsilon_{\mathbf{k}}$ and $\epsilon_{\mathbf{k}'}$ in the denominators of (1.18) and (1.19). For the symmetric Anderson model, this gives the traditional expressions

$$J_{\mathbf{k}\mathbf{k}'} = \frac{8V^*_{\mathbf{k}} V_{\mathbf{k}'}}{U}, \tag{1.22}$$

$$K_{\mathbf{k}\mathbf{k}'} = 0. \tag{1.23}$$

From now on we take $V_{\mathbf{k}} = V = \text{const.}$ and thus $J_{\mathbf{k}\mathbf{k}'} = J = \text{const.}$, corresponding to a strongly localized impurity. One sees that $J > 0$, so that the Kondo interaction between conduction electrons and the localized spin is *antiferromagnetic*.

1.1.3 Perturbation theory

In its simplified form, the Kondo model admits a variety of analytical approaches. However, it is still powerful enough to explain nontrivial features of magnetic impurities, such as the relationship between the resistance minimum and Curie-Weiss behavior. Naturally, one of the first things to try is to expand in the interaction parameter. While most advanced texts on condensed matter physics focus on diagrammatic perturbation theory,

this approach is not directly applicable to the Kondo impurity. Unlike boson or fermion operators, expectation values of the f-spin cannot be decoupled through Wick's theorem. While there are some limited ways around this, many of the curious features are already visible from Kondo's third-order perturbation theory results [60], which we will derive here.

The resistivity is determined by the scattering rate, which to low order can be calculated through time-dependent perturbation theory. The transition rate from an initial state $|i\rangle$ to a (different) final state $|f\rangle$ is given by

$$\Gamma_{i\to f} = 2\pi\delta(E_f - E_i)\left|X_{i\to f} + Y_{i\to f} + \ldots\right|^2 \tag{1.24}$$

$$= 2\pi\delta(E_f - E_i)\left(\left|X_{i\to f}\right|^2 + 2\,\mathrm{Re}(X^*_{i\to f}Y_{i\to f}) + \ldots\right), \tag{1.25}$$

$$X_{i\to f} = \langle f|V|i\rangle\,, \tag{1.26}$$

$$Y_{i\to f} = \sum_j \frac{\langle f|V|j\rangle\ \langle j|V|i\rangle}{E_f - E_j + i\eta}. \tag{1.27}$$

Here, E_i etc. are the unperturbed energies and V is the perturbation operator (H_J in our case). $X_{i\to f}$ and $Y_{i\to f}$ are the lowest-order contributions, respectively proportional to J and J^2: note that the first term of (1.25) is Fermi's golden rule, with the other term a third-order correction.

As the initial state we insert a single electron with momentum $\mathbf{k}$ and spin σ_c into a "background",

$$|i\rangle = \left|\mathbf{k}\sigma_c\sigma_f\Omega\right\rangle. \tag{1.28}$$

Here σ_f denotes the state of the f-spin and Ω that of the other conduction electrons, which will have to be averaged over a thermal distribution later on. The final states have the form

$$|f\rangle = \left|\mathbf{k}'\sigma_c'\sigma_f'\Omega\right\rangle, \tag{1.29}$$

with the background unchanged. Arbitrarily fixing $\sigma_c = \uparrow$, the total scattering rate from $\mathbf{k}$ to $\mathbf{k}'$ is

$$\Gamma_{\mathbf{k}\to\mathbf{k}'} = \left\langle \Gamma_{\uparrow\uparrow\to\uparrow\uparrow} + \Gamma_{\uparrow\downarrow\to\uparrow\downarrow} + \Gamma_{\uparrow\downarrow\to\downarrow\uparrow}\right\rangle_T /2. \tag{1.30}$$

The notation $\uparrow\uparrow\to\uparrow\uparrow$, etc. refers to the initial and final states of σ_c and σ_f. Other scattering processes are forbidden by spin conservation. The angle brackets denote the thermal average, and the final division by two is the average over the initial σ_f (both spin directions are equally likely).

We have to calculate each Γ separately according to (1.25). For each case, the lowest order is given by the golden rule term of (1.26). From the amplitudes in H_J we find

$$X_{\uparrow\uparrow\to\uparrow\uparrow} = \frac{J}{4N}, \tag{1.31}$$

$$X_{\uparrow\downarrow\to\uparrow\downarrow} = -\frac{J}{4N}, \tag{1.32}$$

$$X_{\uparrow\downarrow\to\downarrow\uparrow} = \frac{J}{2N}. \tag{1.33}$$

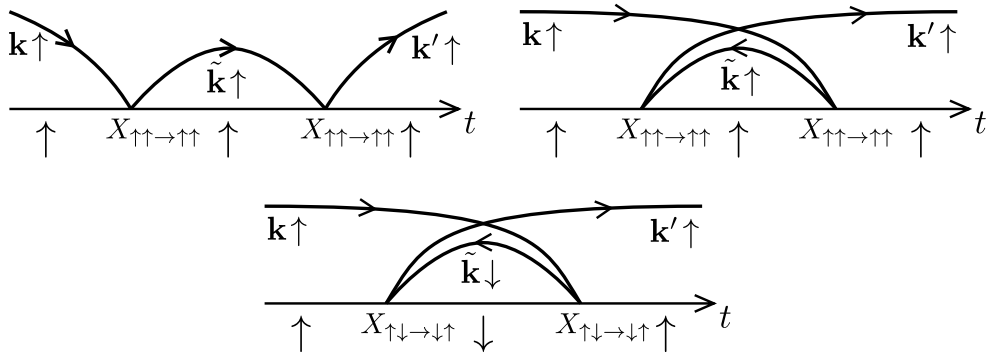

Figure 1.4: Diagrams contributing to $Y_{\uparrow\uparrow\to\uparrow\uparrow}$. Conduction electrons are associated with fermion lines (a hole corresponding to a line running backwards), with the state of the local moment spin written on the time axis. Each scattering event must conserve the total spin. Additionally scattering between parallel spin directions is associated with a factor $X_{\uparrow\uparrow\to\uparrow\uparrow}$, spin-flip scattering with $X_{\uparrow\downarrow\to\downarrow\uparrow}$, and scattering between antiparallel spins (not shown) with $X_{\uparrow\downarrow\to\uparrow\downarrow}$. Notice that a hypothetical fourth diagram (with an intermediate spin-flip but without a particle-hole excitation) is forbidden by spin conservation.

These expressions do not depend on T, so they cannot explain the resistance anomaly. Mathematically, they are more or less equivalent to scattering on a nonmagnetic impurity. For the temperature dependence, we need to go beyond the golden rule.

While we have mentioned that normal diagrammatic perturbation theory is not applicable to the Kondo model, terms in the perturbation series can still be associated with their own (nonstandard) diagrams. For example, the diagrams contributing to $Y_{\uparrow\uparrow\to\uparrow\uparrow}$ are shown in Fig. 1.4. There are two classes of diagrams: in the first class, the $\mathbf{k}$-electron scatters into a an unoccupied state $\tilde{\mathbf{k}}$ and then again into the final state $\mathbf{k}'$. In the second class, a Fermi sea electron $\tilde{\mathbf{k}}$ scatters into $\mathbf{k}'$ and its place is taken by $\mathbf{k}$. Starting from (1.27), it is straightforward to calculate each diagram and sum them up, giving

$$Y_{\uparrow\uparrow\to\uparrow\uparrow} = X^2_{\uparrow\uparrow\to\uparrow\uparrow}(I_1 + I_2) + X^2_{\uparrow\downarrow\to\downarrow\uparrow} I_2, \tag{1.34}$$

$$I_1 = \sum_{\tilde{\mathbf{k}}} \frac{1 - n_{\tilde{\mathbf{k}}}}{\epsilon_{\mathbf{k}} - \epsilon_{\tilde{\mathbf{k}}}}, \tag{1.35}$$

$$I_2 = \sum_{\tilde{\mathbf{k}}} \frac{n_{\tilde{\mathbf{k}}}}{\epsilon_{\mathbf{k}} - \epsilon_{\tilde{\mathbf{k}}}}. \tag{1.36}$$

I_1 and I_2 are factors corresponding to each class of diagram: $n_{\tilde{\mathbf{k}}}$ is the occupation probability of the intermediate state, which must be either unoccupied or occupied depending on the class of diagram. When later averaged over a thermal distribution, $n_{\tilde{\mathbf{k}}}$ will turn into a Fermi function. From (1.25) one sees that only the real part of the sums are required, so they should be understood as principal value sums.

What sets this result apart from a nonmagnetic impurity is the appearance of a lone I_2 in the second term of (1.34), which is associated with spin-flip scattering. For a nonmagnetic

impurity, the result is completely proportional to $I_1 + I_2$, which does not depend on $n_{\tilde{\mathbf{k}}}$, and thus not on T.

Carefully considering every possible diagram, we can calculate

$$Y_{\uparrow\uparrow\to\uparrow\uparrow} = X^2_{\uparrow\uparrow\to\uparrow\uparrow}(I_1 + I_2) + X^2_{\uparrow\downarrow\to\downarrow\uparrow} I_2, \tag{1.37}$$

$$Y_{\uparrow\downarrow\to\uparrow\downarrow} = X^2_{\uparrow\downarrow\to\uparrow\downarrow}(I_1 + I_2) + X^2_{\uparrow\downarrow\to\downarrow\uparrow} I_2, \tag{1.38}$$

$$Y_{\uparrow\downarrow\to\downarrow\uparrow} = 2X_{\uparrow\downarrow\to\downarrow\uparrow} X_{\uparrow\downarrow\to\uparrow\downarrow} I_1 + 2X_{\uparrow\downarrow\to\downarrow\uparrow} X_{\uparrow\uparrow\to\uparrow\uparrow} I_2. \tag{1.39}$$

Inserting each of the three contributions into (1.25) and summing them up as in (1.30), we get the scattering rate

$$\Gamma_{\mathbf{k}\to\mathbf{k}'} = 2\pi\delta(E_f - E_i)\frac{3J^2}{16N^2}\left(1 + \frac{J}{N}\langle I_2 - I_1\rangle_T\right), \tag{1.40}$$

$$\frac{1}{N}\langle I_2 - I_1\rangle_T = \frac{1}{N}\sum_{\tilde{\mathbf{k}}}\frac{2f(\epsilon_{\tilde{\mathbf{k}}}) - 1}{\epsilon_{\mathbf{k}} - \epsilon_{\tilde{\mathbf{k}}}} = \frac{1}{N}\sum_{\tilde{\mathbf{k}}}\frac{-\tanh\left(\frac{\epsilon_{\tilde{\mathbf{k}}}}{2T}\right)}{\epsilon_{\mathbf{k}} - \epsilon_{\tilde{\mathbf{k}}}}. \tag{1.41}$$

As the summand decays away from the Fermi energy (which we set to zero), we approximate the band as flat. This gives

$$\frac{1}{N}\langle I_2 - I_1\rangle_T \approx \rho\int_{-D}^{D} \mathrm{d}\epsilon \frac{\tanh\left(\frac{\epsilon}{2T}\right)}{\epsilon} \approx 2\rho\ln\left(\frac{D}{T}\right), \tag{1.42}$$

where we assumed $|\epsilon_{\mathbf{k}}| < T$, which is the energy range relevant for electrical transport. Otherwise T should be replaced by $|\epsilon_{\mathbf{k}}|$ in the final expression. To derive this result, note that the integrand is $\propto \epsilon^{-1}$ for most of the integration range, with the divergence cut off by D and T for large and small ϵ respectively. We insert this expression into (1.40) and integrate over all final momenta $\mathbf{k}'$, which gives another factor of ρ. The final result for the scattering rate for is

$$\Gamma_{\text{Kondo}} = \frac{3}{8N}J^2\rho\left(1 + 2J\rho\ln\left(\frac{D}{T}\right)\right). \tag{1.43}$$

If the system contains N_{imp} well-separated impurities, we can simply multiply this result by N_{imp} (the scattering rate is then proportional to the impurity density N_{imp}/N, as is physically reasonable).

(1.43) gives an adequate explanation of the resistance minimum. The third-order term gives a positive contribution to the scattering rate $\propto \ln(D/T)$, which increases at low temperatures. If we add the phonon contribution (usually $\propto T^5$), the total resistance ρ_{tot} should thus have the form

$$\rho_{\text{tot}} = A_{\text{ph}}T^5 + \rho_{\text{imp},0} + \rho_{\text{imp},1}\ln\left(\frac{D}{T}\right). \tag{1.44}$$

which has a minimum at

$$T_{\text{min}} = \left(\frac{\rho_{\text{imp},1}}{5A_{\text{ph}}}\right)^{\frac{1}{5}}. \tag{1.45}$$

However, it is clear that this cannot be the full picture. Namely, the correction is divergent at low temperatures; from comparing the relative sizes of the two terms in (1.43), it appears that our perturbative result becomes inapplicable below

$$T_K \sim D e^{-\frac{1}{2J\rho}}, \tag{1.46}$$

which is known as the *Kondo temperature*. The problem of calculating the various electrical and magnetic response functions (which suffer from similar divergences) below the Kondo temperature is known as the *Kondo problem*.

1.1.4 Bound state

Kondo's calculation was soon followed by higher-order expansions, which allow for a resummation of certain classes of terms (most famously Abrikosov's "parquet" method [1]). The results of these methods are generally even more pathological than (1.44), as divergences appear not just at $T = 0$, but already at $T = T_K$. The expression for the Kondo temperature hints at the reason for this: T_K cannot be represented as a power series in J, suggesting that nonperturbative calculations may be required.

The difficulties at low temperatures arise from the formation of a bound state: as the interaction in H_J is antiferromagnetic, it favors configurations where conduction electron spins and the local moment compensate each other and form spin-0 singlet states, in a process called *Kondo screening*. For the compensating electron, the local moment corresponds to an effective attractive potential, resulting in a stable bound state.

This is demonstrated by probably the simplest nonperturbative ansatz, the variational wave function of Yosida [117] (which is analogous to Cooper's earlier calculation for attractive electron-electron interactions [25]). The wave function consists of a filled Fermi sea ($T = 0$), above which a single electron is added to compensate the local moment. In the language of the previous section, this state is

$$|\psi\rangle = \sum_{\mathbf{k}} \psi_{\mathbf{k}} |\mathbf{k}\rangle, \tag{1.47}$$

$$|\mathbf{k}\rangle = \frac{1}{\sqrt{2}} (|\mathbf{k}\uparrow\downarrow \Omega\rangle - |\mathbf{k}\downarrow\uparrow \Omega\rangle \tag{1.48}$$

$\psi_{\mathbf{k}}$ are variational parameters (and normalized to unity). The momentum sum is taken only over empty states ($\epsilon_{\mathbf{k}} > 0$). The matrix elements of the Hamiltonian are

$$\langle \mathbf{k}' | H_t | \mathbf{k} \rangle = \delta_{\mathbf{k}\,\mathbf{k}'} (\epsilon_{\mathbf{k}} + E_\Omega), \tag{1.49}$$

$$\langle \mathbf{k}' | H_J | \mathbf{k} \rangle = -\frac{3}{4}\frac{J}{N}, \tag{1.50}$$

$$E_{\text{var}} = \langle \psi | H_{\text{Kondo}} | \psi \rangle = E_\Omega + \sum_{\mathbf{k}} \epsilon_{\mathbf{k}} \psi_{\mathbf{k}}^2 - \frac{3}{4}\frac{J}{N} \sum_{\mathbf{k}\mathbf{k}'} \psi_{\mathbf{k}} \psi_{\mathbf{k}'}, \tag{1.51}$$

where E_Ω is the (kinetic) energy of the Fermi sea and we calculated the variational energy in the final line. Minimizing this gives the (effectively one-particle) Schrödinger equation

$$E_S \psi_{\mathbf{k}} = \epsilon_{\mathbf{k}} \psi_{\mathbf{k}} - \frac{3}{4}\frac{J}{N}\sum_{\mathbf{k}'} \psi_{\mathbf{k}'}, \tag{1.52}$$

$$E_S = E_{\text{var}} - E_\Omega. \tag{1.53}$$

E_S is the energy of the singlet. Solving (1.52) for $\psi_{\mathbf{k}}$ and then summing over $\mathbf{k}$, we get

$$1 = \frac{3}{4} J \sum_{\mathbf{k}} \frac{1}{\epsilon_{\mathbf{k}} - E_S} \approx \frac{3}{4} J\rho \ln\left(\frac{D}{-E_S}\right), \tag{1.54}$$

$$\Rightarrow E_S = -De^{-\frac{4}{3J\rho}}. \tag{1.55}$$

E_S is indeed negative, so that a bound state exists for arbitrarily small J. While the coefficient in the exponent depends on the specific approximation used, the resemblance to our earlier result for T_K is obvious. This supports the earlier assertion: below T_K, the local moment is bound in a singlet state with vanishing total spin. When $T \sim |E_S| \sim T_K$, the bound state vanishes: intuitively, the (exponentially small) binding energy corresponds to a large time scale between repeated scatterings of the local moment and its "partner electron". By the time the partner returns, the local moment may already have had its spin flipped by scattering with other, thermally excited electrons, thus disturbing the delicate singlet attraction. Once the bound state is completely destroyed, perturbation theory becomes applicable.

If one were to redo the same calculation with a nonmagnetic attractive potential, one would also find a bound state. However, the interpretation would be different: as the impurity does not have a "memory", there is no loss of temporal coherence at higher temperatures. The interesting feature of the Kondo impurity is the *crossover* between two qualitatively different states, which is not associated with the breaking of a physical symmetry.

1.2 Lattice Systems

Following the discussion in the previous sections, it is natural to wonder what happens when the assumption of dilute impurities is violated. For example, how do compounds with a regular lattice of local moments behave? For rare earth compounds there are roughly three regimes [47], depending on the energy difference between the f-electron orbitals and the conduction band. In the "normal" regime, they are located so far away from the Fermi surface that the Kondo coupling can be disregarded, and Kondo physics are not important[3]. This is usually the case for transition metal compounds or pure rare earth systems. The other two regimes are anomalous. If the f-electron levels are very close to (or inside) the conduction band, there are strong charge fluctuations and the system is in the *mixed valence* regime. While this by itself forms a large body of research, we

[3] If there is any c-f-interaction, it is usually a consequence of direct exchange and thus *ferromagnetic*.

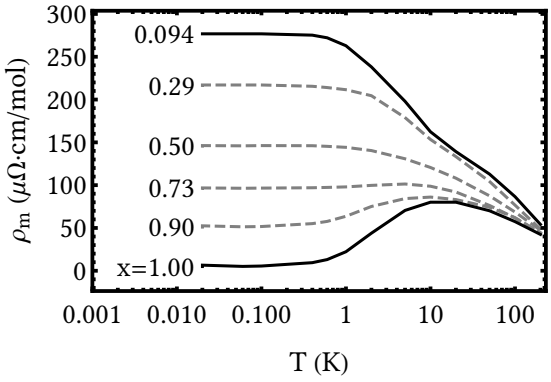

Figure 1.5: The magnetic resistivity ρ_m (i.e., the difference in resistivity between $Ce_xLa_{1-x}Cu_6$ and pure $LaCu_6$) per mole Ce, as found by Sumiyama et al. [107].

are more interested in the third regime, with a moderate separation between f-orbitals and the conduction band. There, one finds an (apparent) lattice analogue of the Kondo effect, so that such systems are referred to as *Kondo lattices*.

1.2.1 Coherence and heavy fermions

To keep in with our discussion of the impurity models, let us begin with a resistance anomaly. $Ce_xLa_{1-x}Cu_6$ is a classic example of a Kondo lattice, and its resistance curve is found in Fig. 1.5 [107]. Lanthanum is nonmagnetic, so that the resistance associated with the magnetic moments (located on the Cerium ions) can be found by subtracting the $x = 0$ (pure $LaCu_6$) resistance. At small-to-moderate doping, the results can be explained by the single-impurity Kondo effect of the previous chapter; upon lowering the temperature, the resistance increases before levelling off at a few K (the Kondo temperature).

However, at large doping $x \approx 1$ (pure $CeCu_6$), something surprising happens: the magnetic contribution to the resistance, which was responsible for the minimum of the *total* resistance, itself has a maximum at a finite temperature. Indeed, the resistance per Cerium ion decreases with the Cerium concentration. The position of this maximum is referred to as the *coherence temperature* T^*, and is usually interpreted as the onset of *coherent scattering*. An intuitive picture of this is the following: In the previous chapter, we viewed the magnetic ions as localized impurities in an otherwise periodic background. However, at $x = 1$ and $T = 0$, the system should be a lattice of screened Cerium ions, so that the screened magnetic ions *are* the periodic background. Thus, since the system is ordered, the current should be carried by Bloch states formed from excitations of the (singulet) screening states, whose residual resistivity is proportional to the *other* impurities of the system. This picture breaks down at the coherence temperature T^*, as then the screening states are so short lived that the local magnetic moments can be viewed as "effectively disordered", at which point usual Kondo physics apply. The transition can loosely be identified as a lattice analogue of the Kondo effect, which is further supported by magnetic susceptibility measurements where a Curie law is recovered at high temperatures (Fig. 1.6).

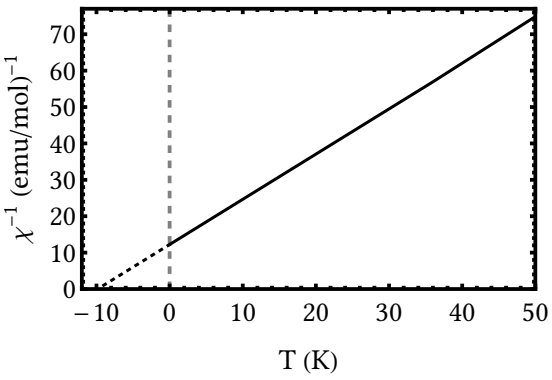

Figure 1.6: The inverse magnetic susceptibility per Cerium atom ($\chi = \chi_{CeCu_6} - \chi_{LaCu_6}$) as found by Onuki and Komatsubara [88]. At large temeperatures χ^{-1} is linear at T, but saturates at a finite value for $T \to 0$ (the extrapolated Curie temperature is negative).

The low-temperature state has other anomalous qualities. The specific heat is given by

$$C = \gamma T, \tag{1.56}$$

as for a normal Fermi liquid, but with an extraordinarily large coefficient γ: typical metals have $\gamma \sim 1$ in units of $\mathrm{mJ/mol\,K^2}$ (Copper has around 0.7 [26], for example), but $CeCu_6$ shows $\gamma \approx 1400$ [37]. γ gives an estimate of the density of states, or (in Fermi liquid theory) the effective mass $m^* \propto \gamma$; although there is no strict cutoff, phases with γ greater than a few tens are referred to as *heavy fermion systems*. The heavy fermion state can also coexist with other kinds of order, even when "traditional" theory would forbid this. For example, although magnetic impurities suppress conventional superconductivity, experiments have found a whole range of heavy fermion superconductors. The textbook example of this is $CeCu_2Si_2$ ($\gamma \sim 1000$) [104, 105], which becomes superconducting below $T_c = 0.6\,\mathrm{K}$. In such superconductors, the mass enhancement can also be estimated from the specific heat discontinuity at T_c, which gives a similarly huge value (implying that the supercurrent is really carried by the heavy fermions).

At this time, no theoretical models adequately explain the anomalous behavior of the Kondo lattices, which includes not only large masses and superconductivity, but also a large variety of magnetically ordered states. This is not even mentioning the possible breakdown of Fermi liquid theory (and thus heavy fermion behavior) in some critical regions, which more recently has become an active field of research [24]. Our own research will focus on the interplay of heavy fermion physics with magnetic order, in a much simplified setting.

1.2.2 Periodic Anderson and Kondo lattice models

The most basic theoretical models that show heavy fermion physics are the *periodic Anderson* and *Kondo lattice models* [47]. Similar to the Kondo impurity, the Kondo lattice

model is derived as the limit of the somewhat more "realistic" periodic Anderson model, which reads (in real space)

$$H_{\mathrm{PAM}} = H_t + H_V + H_f, \tag{1.57}$$

$$H_t = -\sum_{\mathbf{k}\sigma} t_{\mathbf{R}\mathbf{R}'} c^\dagger_{\mathbf{R}\sigma} c_{\mathbf{R}'\sigma}, \tag{1.58}$$

$$H_V = V \sum_{\mathbf{R}\sigma} \left[f^\dagger_{\mathbf{R}\sigma} c_{\mathbf{R}\sigma} + \mathrm{h.c.} \right], \tag{1.59}$$

$$H_f = \epsilon_f \sum_{\mathbf{R}\sigma} f^\dagger_{\mathbf{R}\sigma} f_{\mathbf{R}\sigma} + U \sum_{\mathbf{R}} f^\dagger_{\mathbf{R}\uparrow} f_{\mathbf{R}\uparrow} f^\dagger_{\mathbf{R}\downarrow} f_{\mathbf{R}\downarrow}. \tag{1.60}$$

Simply put, instead of a single isolated impurity, an f-orbital is attached to every lattice site. $t_{\mathbf{R}\mathbf{R}'}$ is the hopping parameter. The parameters V, ϵ_f, and U have the same meaning as in the impurity case. In momentum space, we get (assuming translation invariance, i.e. $t_{\mathbf{R}\mathbf{R}'} = t_{\mathbf{R}-\mathbf{R}'}$)

$$H_{\mathrm{PAM}} = \sum_{\mathbf{k}\sigma} \begin{pmatrix} c^\dagger_{\mathbf{k}\sigma} & f^\dagger_{\mathbf{k}\sigma} \end{pmatrix} \begin{pmatrix} \epsilon_{\mathbf{k}} & V \\ V & \epsilon_f \end{pmatrix} \begin{pmatrix} c_{\mathbf{k}\sigma} \\ f_{\mathbf{k}\sigma} \end{pmatrix} + U \sum_{\mathbf{R}} f^\dagger_{\mathbf{R}\uparrow} f_{\mathbf{R}\uparrow} f^\dagger_{\mathbf{R}\downarrow} f_{\mathbf{R}\downarrow}, \tag{1.61}$$

$$\epsilon_{\mathbf{k}} = -\sum_{\mathbf{R}} e^{-i\mathbf{k}(\mathbf{R}-\mathbf{R}')} t_{\mathbf{R}-\mathbf{R}'}. \tag{1.62}$$

This representation is especially useful in the weakly interacting case.

For large U, one can do the same calculation as in Sec. 1.1.2 to project out states with zero or two f-electrons. This projection is applied to every site, resulting in a lattice of spin-1/2 moments, which are coupled to the conduction electrons through an exchange interaction. The result is the Kondo lattice model,

$$H_{\mathrm{KLM}} = H_t + H_J, \tag{1.63}$$

$$H_J = J \sum_{\mathbf{R}} \mathbf{S}^c_{\mathbf{R}} \mathbf{S}^f_{\mathbf{R}}. \tag{1.64}$$

As before, $J = 8V^2/U$.

1.2.3 Fermi surface

We start with some of the properties of the periodic Anderson model, which can readily be solved in two limits. The first is the noninteracting system with $U \to 0$. In this case, (1.61) is quadratic, so we can immediately calculate the ground state and the quasiparticle energies by diagonalizing the 2×2 band structure matrix. Setting $\epsilon_f = 0$ (the symmetric case), we get two bands with energies

$$E^{\pm}_{\mathbf{k}\sigma} = \frac{\epsilon_{\mathbf{k}}}{2} \pm \sqrt{V^2 + \frac{\epsilon^2_{\mathbf{k}}}{4}}. \tag{1.65}$$

This is shown in Fig. 1.7 (a), for a one-dimensional system with $\epsilon_{\mathbf{k}} = -2t\cos(k)$. The other simple limit is vanishing hybridization $V \to 0$, in which case c- and f-electrons

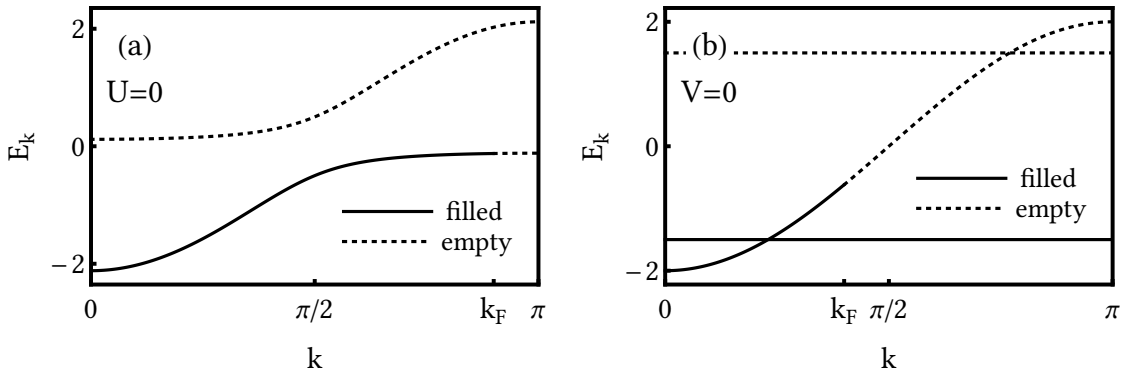

Figure 1.7: Possible band structures for the periodic Anderson model in one dimension, with $n_e = 1.8$ and $t = 1$.

(a) $U = 0$ and $V = 0.5t$. The Fermi energy lies in the lower band, with $k_F = \pi \frac{n_e}{2}$. For $n_e = 2$, the system becomes insulating.

(b) $V = 0$ and $U = 3t$. $n_c = n_e - 1$ electrons are located in a partially filled mobile band, while the other $n_f = 1$ are stuck in a flat lower Hubbard band. $k_F = \pi \frac{n_c}{2}$.

are completely decoupled. The result of this is shown in Fig. 1.7 (b): the quasiparticle bands are simply the original band $\epsilon_{\mathbf{k}}$, and a set of *Hubbard bands* for f-electrons. Note that $V \to 0$ can be implemented in the Kondo lattice model through $J \to 0$, but no such equivalence exists for $U \to 0$ (as then the perturbation theory used to derive the Kondo model no longer applies).

A very significant difference between the two limits is the position of the Fermi surface. While for $U \to 0$ (Fig. 1.7 (b)) we have $k_F \approx \pi/2$ (as for a system that does not have f-electrons at all, with $n_c = n_e - 1$ the conduction electron density), for $V \to 0$ (Fig. 1.7 (a)) we have $k_F \approx \pi$. The two limits thus cannot be adiabatically connected, i.e. we cannot "interpolate" between them.

This dichotomy is of experimental importance. When imaging the Fermi surfaces of real compounds, they oftentimes match well with density functional theory (DFT) calculations, despite of the strong correlations in the f-orbitals. The catch is that, depending on the exact compound and the external parameters, one may need to perform *two different* kinds of DFT calculation: Sometimes the f-orbitals can be simply be regarded as "frozen", i.e. as part of the ionic core of each lattice site (e.g. Ref. [42]); this type of calculation corresponds to $V \to 0$. Other times the f-electrons must be regarded as mobile and taking part in hopping processes (e.g. Ref. [101]); as this implicitly assumes weak correlations, such a calculation corresponds to $U \to 0$. Colloquially, this is referred to as *f-electron delocalization*. Phases with heavy quasiparticles are usually associated with such "delocalized" Fermi surfaces: however, the calculations do not actually reproduce the large masses, only the geometry and volume of the Fermi surface is predicted correctly. Note that this behavior should not be confused with the mixed valence compounds men-

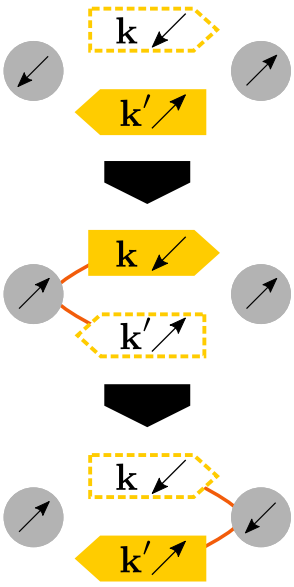

Figure 1.8: Schematic depiction of the RKKY interaction. An electron with momentum $\mathbf{k}'$ from the Fermi sea is scattered from a f-spin into an unoccupied state $\mathbf{k}$, and is then scattered back into $\mathbf{k}'$ from a different f-spin. This leads to an effective nonlocal spin-spin interaction.

tioned in the opening section, as no real evidence for charge fluctuations are found; the apparent delocalization seems to be a correlation effect.

In common parlance, the two types of Fermi surfaces are also referred to as *large* ($U \to 0$) and *small* ($V \to 0$). These terms are derived from a supposed connection to *Luttinger's theorem* [72, 73], which states that the volume of the Fermi surface is the same as that of the noninteracting system, *even in the presence of interactions*. Fig. 1.7 (a) has a "large" Fermi surface, because its k_F is the same as if we had used the original bands $\epsilon_{\mathbf{k}}$ and simply filled them up with *both* c- and f-electrons. The f-electrons can thus be seen as "contributing to the Fermi surface". While we will also use the terms "large" and "small", we must advise some caution, as this is only a description of the *experimental* Fermi surface (as one would find through e.g. quantum oscillation experiments). The *mathematical* definition of the Fermi surface (as used in the proof of Luttinger's theorem) also counts completely filled bands, which do not show up in quantum oscillations. In this sense, the f-electrons thus always "contribute" and the volume of both systems in Fig. 1.7 is actually *the same*. This goes even for the Kondo lattice model, where the f-electrons are in some sense completely theoretical [89]. If we thus, for example, describe a Fermi surface as "small", we only mean that it superficially resembles (and would show a similar experimental signature to) the original Fermi surface of a system without f-electrons; the actual form of the band structure away from the Fermi energy can be quite different.

1.2.4 Magnetic order

In addition to the Fermi surface dynamics described above, we are also interested in magnetic order, which is usually investigated in the Kondo lattice model. The main reason

the lattice models are much more complicated than the impurity systems is *intersite correlations*. The most important such effect is the *RKKY* (Ruderman-Kittel-Kasuya-Yosida) interaction [55, 98, 116], which is illustrated in Fig. 1.8: Scattering of conduction electrons on an f-spin can transfer angular momentum from site to site, resulting in an effective intersite interaction. As first described by Doniach [31], the periodic Anderson and Kondo lattices are governed by two competing phenomena: a statically screened spin cannot take part in RKKY processes, so that the Kondo effect and magnetic interaction at least partially exclude each other.

Based on this reasoning, Doniach then argued for the existence of a magnetic phase transition in the Kondo lattice model. For small J, the strength of the Kondo effect is essentially given by the Kondo temperature $T_K = De^{-\frac{1}{2J\rho}}$, whereas second-order perturbation theory implies that the RKKY interaction is proportional to J^2 (as two spin-flip scattering processes are involved). For $J \to 0$, the RKKY interaction should thus dominate, resulting in a magnetically ordered phase[4]. For large J, this reasoning breaks down. Instead, conduction electrons are tightly bound to each spin (assuming there is one screening electron per spin, i.e. $n_c = 1$), in a lattice analogue of the Yosida bound state of Sec. 1.1.4. The $J \to \infty$ ground state is a product of localized singlets

$$|\Psi\rangle = \prod_{\mathbf{R}} \frac{1}{\sqrt{2}} \left[c^\dagger_{\mathbf{R}\uparrow} f^\dagger_{\mathbf{R}\downarrow} - c^\dagger_{\mathbf{R}\downarrow} f^\dagger_{\mathbf{R}\uparrow} \right] |0\rangle \,, \tag{1.66}$$

with $|0\rangle$ the vacuum. Each singlet contributes an energy $-\frac{3}{4}J$, so that there is an energy gap $\propto J$ that suppresses intersite effects.

From this absence of magnetism at large J, we should expect a phase transition for intermediate J (with $J\rho \sim 1$). This is the region we wish to investigate with the bond fermion method.

[4] The sign of the RKKY interaction is in principle arbitrary and oscillates with distance, usually results in antiferromagnetic order near half-filling.

2 The bond fermion method

2.1 Introduction

The bond fermion method is a conceptually simple approach to the Kondo lattice model, and consists of an expansion around the (exact) $J \to \infty$ limit introduced at the end of the previous chapter. The usefulness of this strong-coupling limit was first pointed out by Lacroix [65], who demonstrated the equivalence of the $J = \infty$ Kondo lattice with the $U = \infty$ Hubbard model. In this limit, the Hubbard model allows only empty (hole) sites that have vanishing spin, and singly occupied sites that carry a spin-1/2. Double occupations are forbidden due to infinite repulsion. Hopping simply exchanges an empty site with a singly occupied site.[1]

For the Kondo lattice at $J = \infty$, sites in a singlet state can be considered "empty" (they have spin-0). At $n_c = 1$, all sites are singlet sites, which would correspond to $n_c = 0$ in the Hubbard model. If we have $n_c < 1$ in the Kondo lattice model, the remaining $1 - n_c$ sites have an empty c-orbital and thus an uncoupled f-electron; as this has a remaining spin-1/2 degree of freedom, these sites can be seen "occupied" by an effective fermion (a *bond fermion*)[2]. Multiple bond fermions cannot occupy the same site, as the result would not correspond to any physical state, so here we too must forbid double occupancy. Hopping processes are shown in Fig. 2.1; c-electron hopping exchanges a singlet site and a site with an empty c-orbital, so we can interpret it in terms of bond fermion hopping (in the opposite direction).

What we thus find is that we can relate the strong-coupling Kondo lattice to the strong-coupling Hubbard model by the replacement

$$n_c \to 1 - n_c. \tag{2.1}$$

This is a nice result, as it allows us to transfer results from the Hubbard model to the Kondo lattice. For example, Nagaoka's theorem states that at $U = \infty$, the Hubbard model with a single hole is ferromagnetic [83]. Thus, the Kondo lattice at $J = \infty$ with only a single conduction electron must be ferromagnetic as well.

The natural question to ask is whether one can extend this to the case of finite J. Necessarily, this is significantly more complicated. Singlets can spontaneously break up through electron hopping: if an electron hops from one singlet to another, two excitations are generated. One site is left empty, while the other is doubly occupied. We thus need to

[1] We assume $n_c \leq 1$ for the conduction electron density. For $n_c \geq 1$, the roles of empty and doubly occupied sites exchanged (*particle-hole symmetry*): here, it is *empty* sites that are forbidden to minimize the interaction energy.

[2] Again, $n_c \geq 1$ can be treated analogously by exchanging empty sites with doubly occupied sites (in the Kondo lattice model, both carry a spin-1/2).

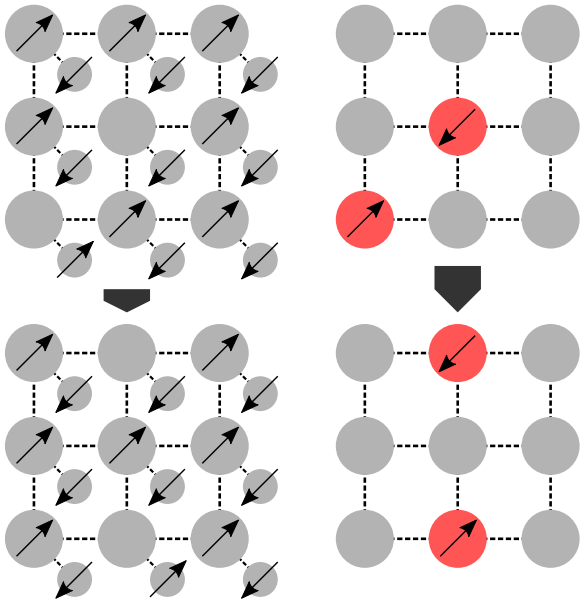

Figure 2.1: The correspondence between the Kondo lattice (left) and bond fermions (right). On most sites, c-electrons (large circles) and f-electrons (small circles) form singlets, illustrated through the opposite-pointing spins. These correspond to empty sites in the bond fermion description. Sites without a c-electron correspond to hole-like bond fermions (red), the spin is carried by the f-electron. Hopping of a c-electron is equivalent to hopping of the bond fermion in the opposite direction.

introduce two species of bond fermions, one for each type of excited state. The described hopping process then corresponds to a pair production of bond fermions (Fig. 2.2). Further, one may have to take spin-1 (triplet) states into account: as triplets carry a spin, they are important for the formation of magnetically ordered states. Note that $J < \infty$ corresponds in no way to the $U < \infty$ Hubbard model: bond fermions are forbidden from occupying the same site by their very nature, independent of J. For example, there is no way to make sense of a site occupied by both a "hole fermion" and a "double occupancy" fermion at the same time.

After Lacroix, bond operators for the Kondo lattice were used by Sigrist et al. to investigate the one-dimensional case [103]. They proved that this system orders ferromagnetically for any nonzero doping ($n_c \neq 1$) and large but finite J. Some years later the idea was picked up again by Eder et al. as an approximate technique to describe the band structure and gap evolution at more moderate $J \sim t$ [34, 35]. This is the inception of the bond fermion method as we will use it. Jurecka and Brenig successfully applied the technique to the antiferromagnetic phase transition at half-filling [53], followed by a similar calculation by Eder et al. [33] for the doped case.

Bond fermions have been introduced in somewhat different ways each time, but there are generally two formulations. One can be viewed as an *operator formulation*, where the bond particles are constructed in an extended Hilbert space augmented with additional constraints [32, 53, 103]. Alternatively, there is what we refer to as the *wave function*

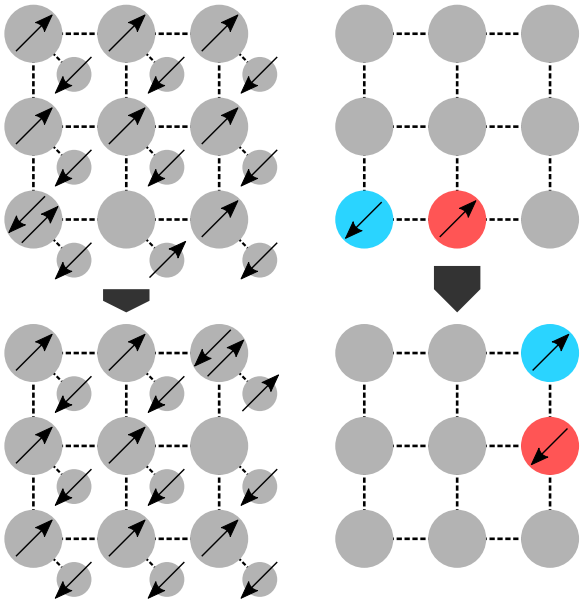

Figure 2.2: Pair creation and annihilation of bond fermions, which is allowed for $J < \infty$. In the bottom left of the grid, a double-occupancy bond fermion (blue) and a hole bond fermion of opposite spin annihilate into two singlets. In the top right, two bond fermions are spontaneously created from two singlet sites.

formulation, where one tries to stay generally in the "physical" Hilbert space, and the bond fermions can be seen as a shorthand to calculate expectation values [34, 35]. This is the view we will present here. While these presentations are all compatible with each other, each suggests its own approximations at some stage of the calculation. We will try to elucidate how these approaches can be interpreted as different methods to implement the constraint of no double occupancy, and also present our own method (an adaptation of the Gutzwiller approximation).

2.2 Variational wave function

It is now time to make the previous section's arguments precise. The local Hilbert space of each site $\mathbf{R}$ of the (single-band, spin-1/2) Kondo lattice consists of eight states. Explicitly, they are

$$|S\rangle_{\mathbf{R}} = \frac{1}{\sqrt{2}} c^\dagger_{\mathbf{R}}\, i\tau_y\, f^*_{\mathbf{R}}\, |0\rangle_{\mathbf{R}}\,, \tag{2.2}$$

$$|\mathbf{T}\rangle_{\mathbf{R}} = \frac{1}{\sqrt{2}} c^\dagger_{\mathbf{R}}\, \boldsymbol{\tau} i\tau_y\, f^*_{\mathbf{R}}\, |0\rangle_{\mathbf{R}}\,, \tag{2.3}$$

$$|A_\sigma\rangle_{\mathbf{R}} = f^\dagger_{\mathbf{R}\sigma}\, |0\rangle_{\mathbf{R}}\,, \tag{2.4}$$

$$|B_\sigma\rangle_{\mathbf{R}} = f^\dagger_{\mathbf{R}\sigma} c^\dagger_{\mathbf{R}\uparrow} c^\dagger_{\mathbf{R}\downarrow}\, |0\rangle_{\mathbf{R}}\,. \tag{2.5}$$

Here we used $|0\rangle_{\mathbf{R}}$ to denote the vacuum state of site $\mathbf{R}$, in which neither the localized nor the conduction electron states are occupied. $f^*_{\mathbf{R}}$ is to be understood as $(f^\dagger_{\mathbf{R}})^\intercal$, i.e. the as the column vector of creation operators.

The conduction orbital is empty (fully occupied) in the two $|A_\sigma\rangle_{\mathbf{R}}$ ($|B_\sigma\rangle_{\mathbf{R}}$) states, so they will correspond to the bond fermions of the introduction. $|S\rangle_{\mathbf{R}}$ is the singlet (ground) state and does not carry a spin; $|\mathbf{T}\rangle_{\mathbf{R}}$ is the vector of excited states, which form a spin-1 triplet. This is also the eigenbasis of the Kondo interaction, with eigenvalues

$$J\mathbf{S}^c_{\mathbf{R}}\mathbf{S}^f_{\mathbf{R}}\,|A_\sigma\rangle_{\mathbf{R}} = J\mathbf{S}^c_{\mathbf{R}}\mathbf{S}^f_{\mathbf{R}}\,|B_\sigma\rangle_{\mathbf{R}} = 0, \tag{2.6}$$

$$J\mathbf{S}^c_{\mathbf{R}}\mathbf{S}^f_{\mathbf{R}}\,|S\rangle_{\mathbf{R}} = -\frac{3}{4}J\,|S\rangle_{\mathbf{R}}\,, \tag{2.7}$$

$$J\mathbf{S}^c_{\mathbf{R}}\mathbf{S}^f_{\mathbf{R}}\,|\mathbf{T}\rangle_{\mathbf{R}} = \frac{1}{4}J\,|\mathbf{T}\rangle_{\mathbf{R}}\,. \tag{2.8}$$

The strategy is now to construct a variational wave function in this new basis. For this, we choose a local "vacuum" state $|\Omega\rangle_{\mathbf{R}}$, along with a set of "creation operators" for our bond particles. Specifically, we will use

$$|\Omega\rangle_{\mathbf{R}} = s_{\mathbf{R}}\,|S\rangle_{\mathbf{R}} + \mathbf{t}_{\mathbf{R}}\,|\mathbf{T}\rangle_{\mathbf{R}}\,, \tag{2.9}$$

$$1 = |s|^2_{\mathbf{R}} + |\mathbf{t}|^2_{\mathbf{R}}. \tag{2.10}$$

While for $J \gg t$ the singlet state ($\mathbf{t}_{\mathbf{R}} = 0$) is appropriate, we want to describe magnetic phases at moderate J. $\mathbf{t}_{\mathbf{R}}$ effectively corresponds to the local magnetic moment, so we can implement magnetic ordering through different choices of $\mathbf{t}_{\mathbf{R}}$.

The creation operators are similar to the ones introduced by Hubbard [50] and given by

$$a^\dagger_{\mathbf{R}\sigma} = |A_\sigma\rangle\langle\Omega|_{\mathbf{R}}\,, \tag{2.11}$$

$$b^\dagger_{\mathbf{R}\sigma} = |B_\sigma\rangle\langle\Omega|_{\mathbf{R}}\,, \tag{2.12}$$

where the operator on the right-hand side acts only on the state at $\mathbf{R}$ while leaving all other sites unchanged. Further, they are taken to anticommute at different sites: $|A_\sigma\rangle\langle\Omega|_{\mathbf{R}}$ and $|B_\sigma\rangle\langle\Omega|_{\mathbf{R}}$ change the fermion number by one, so these operators are "fermionic" in nature[3]. The a- and b-fermions form spin-1/2 doublets, which we collect in the operator vectors

$$a_{\mathbf{R}} = \begin{pmatrix} a_{\mathbf{R}\uparrow} & a_{\mathbf{R}\downarrow} \end{pmatrix}^\intercal, \tag{2.13}$$

$$b_{\mathbf{R}} = \begin{pmatrix} b_{\mathbf{R}\uparrow} & b_{\mathbf{R}\downarrow} \end{pmatrix}^\intercal. \tag{2.14}$$

The variational basis $|i\rangle$ consists of all possible product states

$$|i\rangle = \bigotimes_{\mathbf{R}} |i\rangle_{\mathbf{R}}\,, \tag{2.15}$$

$$|i\rangle_{\mathbf{R}} \in \left\{|\Omega\rangle_{\mathbf{R}}\,,\ |A_\sigma\rangle_{\mathbf{R}}\,,\ |B_\sigma\rangle_{\mathbf{R}}\right\}. \tag{2.16}$$

[3] Technically speaking, the right-hand sides of (2.11–2.12) should include a Jordan-Wigner type factor to enforce this anti-commutativity.

These are precisely the states we generate by applying the fermion creation operators (2.11–2.12) to the vacuum state

$$|\Omega\rangle = \bigotimes_{\mathbf{R}} |\Omega\rangle_{\mathbf{R}} \,. \tag{2.17}$$

Trial states are linear combinations of the $|i\rangle$. The utility of the bond fermions is that they allow for a transparent and intuitive notation when calculating expectation values in this (noncomplete) basis.

It should be kept in mind that the bond fermions are not technically fermions, but instead *hard-core fermions*. When applied to the same site, they do not have the expected anti-commutation relations. For example, (2.11–2.12) imply

$$a^\dagger_{\mathbf{R}\sigma} b_{\mathbf{R}\sigma} = |A_\sigma\rangle\langle\Omega|_{\mathbf{R}} \; |\Omega\rangle\langle B_\sigma|_{\mathbf{R}} = |A_\sigma\rangle\langle B_\sigma|_{\mathbf{R}} \,, \tag{2.18}$$

$$b_{\mathbf{R}\sigma} a^\dagger_{\mathbf{R}\sigma} = |\Omega\rangle\langle B_\sigma|_{\mathbf{R}} \; |A_\sigma\rangle\langle\Omega|_{\mathbf{R}} = 0, \tag{2.19}$$

$$\Rightarrow a^\dagger_{\mathbf{R}\sigma} b_{\mathbf{R}\sigma} \neq -b_{\mathbf{R}\sigma} a^\dagger_{\mathbf{R}\sigma}. \tag{2.20}$$

Multiple occupancies are thus forbidden. This will lead to the equivalence to the $U = \infty$ Hubbard model discussed in the opening section. However, for now we should avoid commuting fermions on the same site to avoid any ambiguity.

For a given variational state $|\Psi\rangle$ (a superposition of the basis states $|i\rangle$ in (2.15)), we can evaluate expectation values of an (electron number conserving) single-site operator $O_{\mathbf{R}}$ by separately computing the contributions of each state:

$$\begin{aligned} \langle O_{\mathbf{R}} \rangle = {} & \omega_{\mathbf{R}} \, \langle \Omega | O_{\mathbf{R}} | \Omega \rangle_{\mathbf{R}} \\ & + \sum_{\sigma\sigma'} \langle a^\dagger_{\mathbf{R}\sigma} a_{\mathbf{R}\sigma'} \rangle \left\langle A_\sigma \middle| O_{\mathbf{R}} \middle| A_{\sigma'} \right\rangle_{\mathbf{R}} \\ & + \sum_{\sigma\sigma'} \langle b^\dagger_{\mathbf{R}\sigma} b_{\mathbf{R}\sigma'} \rangle \left\langle B_\sigma \middle| O_{\mathbf{R}} \middle| B_{\sigma'} \right\rangle_{\mathbf{R}} \end{aligned} \tag{2.21}$$

$$\omega_{\mathbf{R}} = 1 - \langle a^\dagger_{\mathbf{R}} a_{\mathbf{R}} \rangle - \langle b^\dagger_{\mathbf{R}} b_{\mathbf{R}} \rangle. \tag{2.22}$$

Simple angle brackets $\langle \cdot \rangle$ denote expectation values with respect to $|\Psi\rangle$. $\omega_{\mathbf{R}}$ is the probability that site $\mathbf{R}$ is in the "vacuum" state. Some useful expectation values are

$$\langle c^\dagger_{\mathbf{R}} c_{\mathbf{R}} \rangle = \omega_{\mathbf{R}} + 2\langle b^\dagger_{\mathbf{R}} b_{\mathbf{R}} \rangle \tag{2.23}$$

$$= 1 - \langle a^\dagger_{\mathbf{R}} a_{\mathbf{R}} \rangle + \langle b^\dagger_{\mathbf{R}} b_{\mathbf{R}} \rangle, \tag{2.24}$$

$$\langle \mathbf{S}^c_{\mathbf{R}} \mathbf{S}^f_{\mathbf{R}} \rangle = \omega_{\mathbf{R}} \left(-\frac{3}{4} |s_{\mathbf{R}}|^2 + \frac{1}{4} |\mathbf{t}_{\mathbf{R}}|^2 \right), \tag{2.25}$$

$$\langle \mathbf{S}^c_{\mathbf{R}} \rangle = \omega_{\mathbf{R}} \big(+ \mathrm{Re}[s^*_{\mathbf{R}} \mathbf{t}_{\mathbf{R}}] + \frac{i}{2} \mathbf{t}^*_{\mathbf{R}} \times \mathbf{t}_{\mathbf{R}} \big), \tag{2.26}$$

$$\langle \mathbf{S}^f_{\mathbf{R}} \rangle = \omega_{\mathbf{R}} \big(- \mathrm{Re}[s^*_{\mathbf{R}} \mathbf{t}_{\mathbf{R}}] + \frac{i}{2} \mathbf{t}^*_{\mathbf{R}} \times \mathbf{t}_{\mathbf{R}} \big) + \langle a^\dagger_{\mathbf{R}} \frac{\boldsymbol{\tau}}{2} a_{\mathbf{R}} \rangle + \langle b^\dagger_{\mathbf{R}} \frac{\boldsymbol{\tau}}{2} b_{\mathbf{R}} \rangle. \tag{2.27}$$

From (2.24) we can see that $a^\dagger_{\mathbf{R}}$ and $b^\dagger_{\mathbf{R}}$ have the expected effect on the electron number, respectively decreasing or increasing it by one. (2.25) gives us the Kondo interaction,

which is now a simple quadratic function of the fermion operators. An external magnetic field couples to the spin expectation values (2.26–2.27); in most actual calculations $s_{\mathbf{R}}$ and $\mathbf{t}_{\mathbf{R}}$ are real, so that the net total spin $(\mathbf{S}^c_{\mathbf{R}} + \mathbf{S}^f_{\mathbf{R}})$ is nonzero only in the fermion-like states.

To calculate the kinetic energy, we must also consider nonlocal electron bilinears, i.e. expectation values with $\mathbf{R} \neq \mathbf{R}'$. These effectively factorize, where each electron is separately transformed into a sum of bond fermions before taking the expectation value [32]:

$$\langle c^\dagger_{\mathbf{R}\sigma} c_{\mathbf{R}'\sigma'} \rangle = \sum_{\alpha\alpha'} W^*_{\mathbf{R}\sigma\alpha} W_{\mathbf{R}'\sigma'\alpha'} \langle v^\dagger_{\mathbf{R}\alpha} v_{\mathbf{R}'\alpha'} \rangle, \tag{2.28}$$

$$v_{\mathbf{R}} = \begin{pmatrix} a^\dagger_{\mathbf{R}\uparrow} & a^\dagger_{\mathbf{R}\downarrow} & b_{\mathbf{R}\uparrow} & b_{\mathbf{R}\downarrow} \end{pmatrix}^{\mathsf{T}}, \tag{2.29}$$

$$W_{\mathbf{R}} = \frac{1}{\sqrt{2}} \begin{pmatrix} [s^*_{\mathbf{R}} + \mathbf{t}^*_{\mathbf{R}} \boldsymbol{\tau}]\, i\tau_y & [-s_{\mathbf{R}} + \mathbf{t}_{\mathbf{R}} \boldsymbol{\tau}] \end{pmatrix}. \tag{2.30}$$

The combined vector $v_{\mathbf{R}}$ is indexed by Greek letters and contains both creation and annihilation operators. $W_{\mathbf{R}\sigma\alpha}$ is a 2×4 matrix, with the index α ranging over the four components of $v_{\mathbf{R}}$. The $W_{\mathbf{R}}$ are used to "translate" electron hopping expectation values into bond fermion hopping expectation values. Note that $\langle c^\dagger_{\mathbf{R}\sigma} c_{\mathbf{R}'\sigma'} \rangle$ contains not only terms corresponding to bond fermion propagation (of the form $\langle a^\dagger_{\mathbf{R}\sigma} a_{\mathbf{R}'\sigma'} \rangle$ and $\langle b^\dagger_{\mathbf{R}\sigma} b_{\mathbf{R}'\sigma'} \rangle$), but also bond fermion pair creation or annihilation ($\langle a^\dagger_{\mathbf{R}\sigma} b^\dagger_{\mathbf{R}'\sigma'} \rangle$ and $\langle a_{\mathbf{R}\sigma} b_{\mathbf{R}'\sigma'} \rangle$). These terms correspond to the spontaneous breaking of singlet bound states referred to in the opening section. To arrive at the above expression it is allowed to anticommute bond fermion operators, as they act on different sites.

(2.24–2.27) and (2.28) are enough to calculate the variational energy. For generality, we introduce leave open the possibility for an external magnetic field $\mathbf{B}$; the magnetic field Hamiltonian reads

$$H_{\mathbf{B}} = -\mathbf{B} \sum_{\mathbf{R}} \left(\mathbf{S}^c_{\mathbf{R}} + \mathbf{S}^f_{\mathbf{R}} \right). \tag{2.31}$$

The total variational energy is

$$\langle H \rangle = \langle H_J \rangle + \langle H_{\mathbf{B}} \rangle + \langle H_t \rangle \tag{2.32}$$

$$\langle H_J \rangle + \langle H_{\mathbf{B}} \rangle = \sum_{\mathbf{R}} \left[e_{\mathbf{R}} \left(\langle a^\dagger_{\mathbf{R}} a_{\mathbf{R}} \rangle + \langle b^\dagger_{\mathbf{R}} b_{\mathbf{R}} \rangle - 1 \right) - \frac{\mathbf{B}}{2} \left(\langle a^\dagger_{\mathbf{R}} \boldsymbol{\tau} a_{\mathbf{R}} \rangle + \langle b^\dagger_{\mathbf{R}} \boldsymbol{\tau} b_{\mathbf{R}} \rangle \right) \right], \tag{2.33}$$

$$e_{\mathbf{R}} = \frac{3J}{4} s^2_{\mathbf{R}} - \frac{J}{4} \mathbf{t}^2_{\mathbf{R}} - i\mathbf{B}(\mathbf{t}^*_{\mathbf{R}} \times \mathbf{t}_{\mathbf{R}}), \tag{2.34}$$

$$\langle H_t \rangle = -\sum_{\mathbf{R}\mathbf{R}'} t_{\mathbf{R}\mathbf{R}'} \left\langle v^\dagger_{\mathbf{R}} W^\dagger_{\mathbf{R}} W_{\mathbf{R}'} v_{\mathbf{R}'} \right\rangle. \tag{2.35}$$

$\langle H_J \rangle + \langle H_{\mathbf{B}} \rangle$ give the "local" contribution to the energy. $e_{\mathbf{R}}$ is the energy needed to destroy the background state on site $\mathbf{R}$ (and thus to create a bond fermion); the two terms proportional to J are the Kondo energy, and the term proportional to $\mathbf{B}$ the Zeeman energy of the background state (as mentioned, this usually vanishes).

There are two issues remaining. Obviously, one still has to handle the hard-core nature of the fermions somehow (the Kondo interaction has been taken care of). However, we

also have already implicitly introduced another approximation, as the basis (2.15) is not complete. For an exact mapping, one can in principle introduce boson operators that generate the remaining states, which contain one conduction electron and are orthogonal to $|\Omega\rangle_{\mathbf{R}}$ [32, 53]. These are the *triplet fluctuations*, which we will disregard. The main complications is that the expression for the hopping expectation values (2.28) must be modified: intuitively, a hopping bond fermion can leave a "string" of excited states in its wake. Such processes are described by terms cubic and quartic in the bond particle operators. While there have been some attempts to include these processes [32], we will content ourselves with our "static" approximation, i.e. that the effect of the triplet states is contained entirely within $|\Omega\rangle_{\mathbf{R}}$.

2.3 Gutzwiller approximation

There are multiple ways to deal with the hard-core condition on the bond fermions. We will first describe the *Gutzwiller approximation*, a classic method for strongly correlated systems. Two simpler schemes will be described and discussed afterwards.

First of all, we replace the hard-core fermions with normal fermions subject to an infinite interaction ($U = \infty$ Hubbard model), as this cannot change the observables of the system. One should think of this as an entirely different system that happens to give the same results, and where expectation values take the same form as calculated in the previous section (which fixed the true ordering of fermion operators). However, now anticommutations as in (2.20) are allowed: while an intermediate state may have two fermions and thus infinite energy, it is still part of the new Hilbert space, so the operator does not have to vanish. Naturally, we will use the same symbols for a, b, etc. in the new system.

The Gutzwiller wave function (and the associated Gutzwiller approximation) was originally developed for the Hubbard model [40]. The ground state is approximated by an uncorrelated (Slater determinant) wave function $|\Psi_0\rangle$, which is multiplied by a *Gutzwiller projection operator* P:

$$|\Psi_{\mathrm{G}}\rangle = P\,|\Psi_0\rangle\,, \tag{2.36}$$

$$P = \prod_{\mathbf{R}} P_{\mathbf{R}}. \tag{2.37}$$

The role of $P_{\mathbf{R}}$ is to reduce the weight of energetically unfavorable configurations on site $\mathbf{R}$. For example, Gutzwiller's ansatz for the Hubbard model had

$$P_{\mathbf{R}} = g^{c^\dagger_{\mathbf{R}\uparrow} c_{\mathbf{R}\uparrow} c^\dagger_{\mathbf{R}\downarrow} c_{\mathbf{R}\downarrow}} \tag{2.38}$$

with $0 \leq g \leq 1$ tuned to minimize the variational energy. A configuration with N_D double occupations is multiplied with a factor of g^{N_D}, which reduces the interaction energy (but will incur a cost in the kinetic energy). For $g = 1$ we have $P_{\mathbf{R}} = 1$, so that $|\Psi_0\rangle$ remains unmodified: the Gutzwiller ansatz thus includes Hartree-Fock theory as a limiting case. The strong-coupling limit is $g = 0$, in which double occupations are completely forbidden. We will use a similar $P_{\mathbf{R}}$, as we are also trying to eliminate double occupations. However, the

more complicated multiband form of the bond fermion Hamiltonian necessitates somewhat heavier machinery than Gutzwiller's original formalism. For systems with a more complicated interaction term, $P_{\mathbf{R}}$ would also be more complicated. For example, Lanatà et al. [68] applied the method to the Kondo lattice model by starting with a Slater determinant wave function of c- and f-electrons. The role of $P_{\mathbf{R}}$ was then twofold: First to project out double occupations of f-electrons (this part is taken care of automatically in the bond fermion method), and to optimize the interaction energy by increasing the weight of singlet configurations (and decreasing that of triplet configurations). Thus, while in both cases a Gutzwiller wave function is used, in spirit, their calculation is quite different from bond fermion theory.

When actually trying to calculate expectation values of a Gutzwiller wave function, it quickly becomes apparent that this task is far from trivial even in the comparatively simple case of (2.38). An exact evaluation is usually only possible for small systems using the variational Monte Carlo technique [22]. Still, one can often get a reasonable estimate using mostly analytic means; this is the domain of the Gutzwiller approximation, which was originally derived combinatorially [40]. However, this method is difficult to generalize, so that in most modern calculations a different formalism is used.

Metzner and Vollhardt [79] first demonstrated that expectation values of the Gutzwiller wave function with $P_{\mathbf{R}}$ as in (2.38) can be calculated exactly in the limit of a very large number of spatial dimensions. In this formalism, the Gutzwiller approximation consists of using the same expression for finite-dimensional lattices. Generally speaking, the same approximations can be derived by a *slave boson mean-field* scheme originally put forward by Kotliar and Ruckenstein [62]. The slave boson scheme is simpler in the sense that one often arrives at the correct result more quickly, but we here outline the infinite-dimensions version of the calculation as we feel it is closer in spirit to our own wave function based approach.

When the Gutzwiller approximation is applied to our bond fermion wave function, we must take care because of the presence of pairing terms $a^\dagger_{\mathbf{R}\sigma} b^\dagger_{\mathbf{R}'\sigma'}$ in the hopping term (2.28), which require a slight extension of the usual method. How to include such anomalous terms is described by Fabrizio [36] in the context of superconductivity. For the derivation of the method, we will loosely follow Strand [106]; however, we have generally tried to be more thorough in some regions that were mostly skimmed over, especially regarding the treatment of disconnected diagrams (for example, the revised diagram series introduced in Sec. 2.3.1.1 is original). This thoroughness goes at the cost of brevity: readers that are not interested in the technical details of the $d \to \infty$ limit are advised to skip to Sec. 2.3.4, where the main results (which turn out to be very simple) are presented.

2.3.1 Diagrammatic series and Gutzwiller conditions

We will present the Gutzwiller approximation in its general form before specializing to our simple hard-core interaction system later on. For now, it is enough to know that we are dealing with a system of fermions, and $P_{\mathbf{R}}$ is a generic local operator (despite the name, it is usually not a projection operator in the sense that $P_{\mathbf{R}}^2 \neq P_{\mathbf{R}}$). The only requirement is that $|\Psi_0\rangle$ and $P_{\mathbf{R}}$ conserve *fermion parity*: fermions should only be created or destroyed in

pairs (a property which we call *fermion-even*), so that the expectation value of a product of an odd number of fermion operators vanishes.

The expectation value of a generic fermion-even operator O is

$$\langle O \rangle = \frac{\langle P^\dagger O P \rangle_0}{\langle P^\dagger P \rangle_0}. \tag{2.39}$$

$\langle \cdot \rangle$ stands for an expectation value with respect to $|\Psi_G\rangle$ and $\langle \cdot \rangle_0$ for expectation values with respect to $|\Psi_0\rangle$ (which should be a normalized state). Fermion-evenness means that O is an product of evenly many fermion operators $q_{\mathbf{R}\alpha}$. The index α here ranges over both creation and annihilation operators: in the bond fermion context α is a tuple $(s\sigma)$ with a species index $s \in \{a, a^\dagger, b, b^\dagger\}$ and a spin index σ. This should not be confused with the Greek indices in (2.29), where the species index is restricted to $\{a^\dagger, b\}$.

Let us try to evaluate the numerator of (2.39) for the special case of a local operator $O_{\mathbf{R}}$ (that has all its constituent $q_{\mathbf{R}\alpha}$ acting on the same site). Local operators of interest are charge densities, spin densities, interaction energies, etc. We introduce the shorthand notation

$$Q_{\mathbf{R}} = P_{\mathbf{R}}^\dagger O_{\mathbf{R}} P_{\mathbf{R}}, \tag{2.40}$$

$$S_{\mathbf{R}} = P_{\mathbf{R}}^\dagger P_{\mathbf{R}} - 1. \tag{2.41}$$

Since the $P_{\mathbf{R}}$ commute at different sites, this yields

$$\langle P^\dagger O_{\mathbf{R}} P \rangle_0 = \langle Q_{\mathbf{R}} \prod_{\mathbf{R}' \neq \mathbf{R}} (1 + S_{\mathbf{R}'}) \rangle_0 \tag{2.42}$$

$$= \sum_{m \geq 0} \sum_{\substack{\mathbf{R}_1 < \ldots < \mathbf{R}_m \\ \mathbf{R}_i \neq \mathbf{R}}} \langle Q_{\mathbf{R}} S_{\mathbf{R}_1} \ldots S_{\mathbf{R}_m} \rangle_0 \tag{2.43}$$

$$= \sum_{m \geq 0} \frac{1}{m!} \sum_{\substack{\{\mathbf{R}_1 \ldots \mathbf{R}_m\} \\ \mathbf{R}_i \neq \mathbf{R}}} \langle Q_{\mathbf{R}} S_{\mathbf{R}_1} \ldots S_{\mathbf{R}_m} \rangle_0. \tag{2.44}$$

In the second line, the sum is taken over *ordered* tuples (the ordering of sites is arbitrary but should be fixed). In the third line we drop the ordering and instead divide by $m!$ (we use the $\{\cdot\}$ notation to mean that all summands should be unique; $\mathbf{R}$ is not summed over).

We can now try to evaluate the sum by means of Wick's theorem, for which we rewrite it as a diagrammatic series. Evaluating the series is difficult in general, but with slight restrictions on $P_{\mathbf{R}}$ we can eliminate many lower-order diagrams; the rest is then easily calculated in the limit of infinite dimensions.

To illustrate, let us look at the $m = 0$ and $m = 1$ terms in (2.44):

$$\langle P^\dagger O_{\mathbf{R}} P \rangle_0 = \langle Q_{\mathbf{R}} \rangle_0 + \sum_{\mathbf{R}' \neq \mathbf{R}} \left[\langle Q_{\mathbf{R}} \rangle_0 \langle S_{\mathbf{R}'} \rangle_0 + \langle \overbrace{Q_{\mathbf{R}} S_{\mathbf{R}'}} \rangle_0 + \langle \overbrace{Q_{\mathbf{R}} S_{\mathbf{R}'}} \rangle_0 + \ldots \right] + \sum_{m \geq 2} \ldots \tag{2.45}$$

We have organized the $m = 1$ contribution by the number of *Wick contractions* [112] between $Q_{\mathbf{R}}$ and $S_{\mathbf{R}'}$. The diagrams associated with each term are pictured in Fig. 2.3,

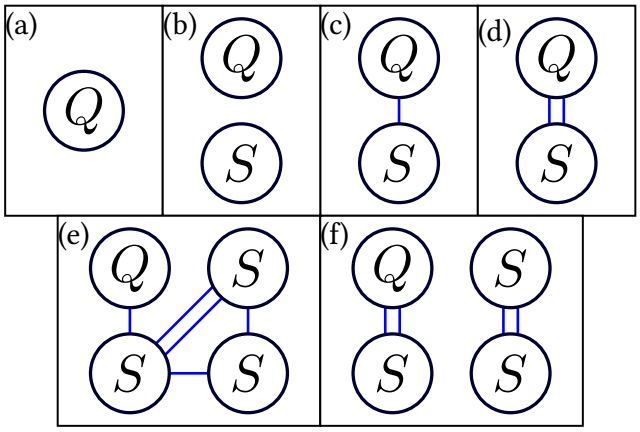

Figure 2.3: Examples of diagrams for the Gutzwiller wave function. (a–d) are the lowest order diagrams ($m \leq 1$). (e–f) have $m = 3$, with (e) connected and (f) disconnected.

which also shows some examples of higher-order ($m = 3$) diagrams. *Vertices* correspond to operators $Q_{\mathbf{R}}$, $S_{\mathbf{R}'}$, etc., and *blue lines* indicate one or more nonlocal Wick contractions[4]. The $m = 0$ diagram does not involve a lattice sum and can be directly calculated using only local expectation values. The $m = 1$ contribution is already more difficult, as it involves a sum over $\mathbf{R}'$. As we will see, these lattice sums are the main challenge that needs to be overcome.

2.3.1.1 Linked cluster theorem

The first thing we notice is that the diagram with zero contractions (Fig. 2.3 (b)) is a *disconnected* diagram, as it has two independent components. Experience with other diagrammatic expansions tells us that we should apply the *linked cluster theorem*: to calculate the expectation value $\langle O \rangle$, we also need to take into account the denominator of (2.39), which can be expanded in a similar diagrammatic series and cancels the contribution of the disconnected diagrams. A simple proof of the linked cluster theorem is through the *replica trick* [84]. Formally, we replicate our system (and our Gutzwiller wave function) n times by adding a replica index $1 \leq k \leq n$ to each site. Each replica is independent, so that only correlation functions with alike replica indices are nonvanishing. $\langle O_{\mathbf{R}} \rangle = \langle O_{1\mathbf{R}} \rangle_n$ is calculated on the first replica, where the notation on the right-hand side indicates that the expectation value is taken in the n-fold replicated space.

The main crux of the replica argument is that, since correlations between different replicas are zero, the replica index must be constant on each connected part of a diagram. However, the indices can be chosen independently for each connected part (except for the

[4] Since our operators $Q_{\mathbf{R}}$ and $S_{\mathbf{R}'}$ have a "substructure" (they consist of multiple fermion operators), the actual evaluation of a diagram also involves *local* contractions between e.g. the individual fermion operators that make up $Q_{\mathbf{R}}$. For example, Fig. 2.3 (c) does not specify exactly *which* fermion operators in $Q_{\mathbf{R}}$ and $S_{\mathbf{R}'}$ need to be contracted with each other. In effect, it represents a sum over all possible ways of contracting individual fermion operators, but under the restriction that *exactly one* of these contractions is nonlocal.

one attached to our operator $Q_{1\mathbf{R}}$), which results in a factor of n each time. We expand both the numerator and the denominator as power series in n, which gives

$$\langle O_{\mathbf{R}} \rangle = \langle O_{1\mathbf{R}} \rangle_n = \frac{\langle P^\dagger O_{1\mathbf{R}} P \rangle_{0,n}}{\langle P^\dagger P \rangle_{0,n}} = \frac{\sum \{\text{connected diagrams}\} + O(n)}{1 + O(n)} \tag{2.46}$$

$$= \sum \{\text{connected diagrams}\}. \tag{2.47}$$

In the first line, we used that all disconnected contributions to the numerator scale with at least n, whereas in the denominator, all terms except the empty diagram (with value 1 as the $|\Psi_0\rangle$ is normalized) contain factors of n. The second line follows by the following argument: As $\langle O_{\mathbf{R}} \rangle$ is clearly unchanged by adding independent replicas, the final expression in (2.46) can also not depend on n. We are then free to choose any value of n to evaluate the expression, and we get the second line by taking $n = 0$. For readers uncomfortable with this analytic continuation, we refer to the combinatorial proof [2], although in our case the replica trick is rigorous (both the numerator and denominator are finite sums, as long as the system itself has finite size).

Sadly, experience has failed us here, because we have not defined our diagram series carefully enough [19]. The issue lies in the summation restrictions of (2.44), which spoil the above argument: Since all summands must be unique, supposedly independent diagram parts can "block" each other. For example, without the summation restriction, our $m = 1$ disconnected diagram would simply be proportional to the total number of sites nN, as each replica contributes N sites. However, *only* on the first replica, we must have $\mathbf{R}' \neq \mathbf{R}$, so that the diagram is actually $\propto nN - 1$, which *does not* vanish for $n = 0$. Thus, taking $n = 0$ will not eliminate the disconnected diagrams in the numerator (although the denominator still goes to 1). Equivalently, the combinatorial proof requires diagrams to factorize, which would also need the summations to be unrestricted.

There are multiple ways to salvage the diagram series. For the Hubbard model, the Gutzwiller operator is simple enough that only a very slight reinterpretation of the diagrams is needed to make the linked cluster theorem apply [38]. For the more general calculation we are attempting, this simpler approach does not work. One option here is to simply accept that the theorem does not hold, but demonstrate that all the disconnected contributions vanish anyway (for infinite dimensions) [19]. Instead, we choose a different approach that we think is somewhat easier to reason about: as we will demonstrate, we can remove the summation restrictions by introducing new diagrams that effectively cancel the overcounted contributions. The linked cluster then applies and we only need to retain connected diagrams.

First of all, we note that since all sites were unique in our previous diagram series, we only ever drew blue lines between distinct sites. We are thus safe to associate each blue line with not only a Wick contraction, but also a redundant factor of $(1 - \delta_{\mathbf{R}_i \mathbf{R}_j})$. For example, Fig. 2.3 (c) is modified as

$$\langle \overbrace{Q_{\mathbf{R}} S_{\mathbf{R}'}} \rangle_0 \to (1 - \delta_{\mathbf{R}\mathbf{R}'}) \langle \overbrace{Q_{\mathbf{R}} S_{\mathbf{R}'}} \rangle_0. \tag{2.48}$$

Since $\mathbf{R} \neq \mathbf{R}'$ in the sum over sites, this does not change the result. The utility of this modification is that it explicitly removes contributions like $\langle \overbrace{Q_{\mathbf{R}} S_{\mathbf{R}}} \rangle_0$, which will appear once we relax the summation restriction.

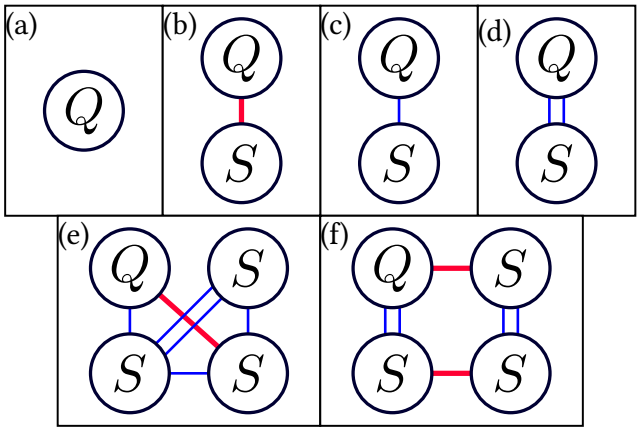

Figure 2.4: Connected diagrams in the revised series. (a–d) are the lowest order diagrams ($m \leq 1$). (e–f) have $m = 3$: Note that (e) is still a valid connected diagram if one were to remove the red line, whereas (f) would become disconnected.

It is important to understand that this modification is not enough to let us relax the summation restrictions, as all sites in a diagram that are not linked directly could still be the same. For example, in Fig. 2.3 (e), the top left site (which holds Q) must be different from the bottom left site, but could be the same as either of the sites on the right of the diagram. In particular, it also does not help with the disconnected diagrams. To completely remove the summation restrictions, we instead use the *inclusion-exclusion principle* known from combinatorics: for a general restricted sum we can write (writing $\mathbf{R}_0$ for $\mathbf{R}$ to simplify the notation; $\mathbf{R}_0$ is not summed over)

$$\sum_{\substack{\{\mathbf{R}_1 \ldots \mathbf{R}_m\} \\ \mathbf{R}_i \neq \mathbf{R}_0}} = \sum_{\mathbf{R}_1 \ldots \mathbf{R}_m} \prod_{0 \leq i < j \leq m} (1 - \delta_{\mathbf{R}_i \mathbf{R}_j}) \tag{2.49}$$

$$= \sum_{\mathbf{R}_1 \ldots \mathbf{R}_m} - \sum_{\mathbf{R}_1 \ldots \mathbf{R}_m} \sum_{\substack{(i,j) \\ \text{pairs}}} \delta_{\mathbf{R}_i \mathbf{R}_j} + \sum_{\mathbf{R}_1 \ldots \mathbf{R}_m} \sum_{\substack{(i,j),(k,l) \\ \text{pairs}}} \delta_{\mathbf{R}_i \mathbf{R}_j} \delta_{\mathbf{R}_k \mathbf{R}_l} + \ldots \tag{2.50}$$

In the first line we moved the restrictions from the *summation* to the *summand* by explicitly writing them out in a product. In the second line we then expanded this product[5]. The result can also be interpreted diagrammatically by associating each $\delta_{\mathbf{R}_i \mathbf{R}_j}$ with a *red line* between $\mathbf{R}_i$ and $\mathbf{R}_j$. The zeroth sum in (2.50) generates diagrams with zero red lines, the first sum diagrams with a single red line, etc. The resulting diagrams thus have two different kinds of lines (blue and red), where the red lines cancel the forbidden contributions introduced by relaxing the summation restriction on the $\mathbf{R}_i$.

With this modification, the linked cluster theorem applies. Diagrams are shown in Fig. 2.4. To reiterate, sites can be connected by

- one or more *blue lines* which imply Wick contractions and a factor of $(1 - \delta_{\mathbf{R}_i \mathbf{R}_j})$
- a single *red line* which implies a factor of $-\delta_{\mathbf{R}_i \mathbf{R}_j}$

[5] The "pairs" notation means that each 2-tuple of indices should be unique and ordered.

Since $(1-\delta_{\mathbf{R}_i\mathbf{R}_j})\delta_{\mathbf{R}_i\mathbf{R}_j} = 0$, there are *no* diagrams where a pair of sites is connected by both blue lines and a red line (indeed, this was the reason we introduced the extra factor $(1-\delta_{\mathbf{R}_i\mathbf{R}_j})$ to each blue line). From Fig. 2.4 (a–d), the lowest-order contributions to the expectation value are now

$$\langle O_{\mathbf{R}}\rangle = \langle Q_{\mathbf{R}}\rangle_0 + \sum_{\mathbf{R}'}\left[-\delta_{\mathbf{R}\mathbf{R}'}\langle Q_{\mathbf{R}}\rangle_0\langle S_{\mathbf{R}'}\rangle_0 + (1-\delta_{\mathbf{R}\mathbf{R}'})\langle \overbrace{Q_{\mathbf{R}}S_{\mathbf{R}'}}\rangle_0 + (1-\delta_{\mathbf{R}\mathbf{R}'})\langle \overbrace{\overbrace{Q_{\mathbf{R}}S_{\mathbf{R}'}}}\rangle_0 + \ldots\right] + \sum_{m\geq 2}\ldots \tag{2.51}$$

Note the negative sign of the red-line diagram, which corresponds to the $n = 0$ limit of the proportionality constant $nN - 1$ we mentioned earlier.

2.3.1.2 Eliminating low-order diagrams

Having laid a solid foundation, we should now actually evaluate some diagrams. The $m = 0$ contribution in (2.51) is trivial, so we will focus on the $m = 1$ sum, evaluating each term in order. Actually, we have some further leeway in reducing our workload. For example, the red-line diagram can be set to zero provided we properly modify our ansatz for the projection operator $P_{\mathbf{R}}$. This is called the *first Gutzwiller condition*[6], and is usually written as

$$\langle S_{\mathbf{R}}\rangle_0 = 0 \Leftrightarrow \langle P_{\mathbf{R}}^\dagger P_{\mathbf{R}}\rangle_0 = 1. \tag{2.52}$$

This constraint can be enforced by an appropriate rescaling of $P_{\mathbf{R}}$, so that this does not actually reduce our variational space[7]. In general, this means that every S in a diagram must have at least a single blue line originating from it.

For the next few terms, let us look at the general structure of Wick contractions. The $Q_{\mathbf{R}}$ and $S_{\mathbf{R}}$ can be written as fermionic polynomials (temporarily suppressing the site index):

$$Q = \sum_X Q_X H_X, \tag{2.53}$$

$$H_X = \prod_{\xi\in X} q_\xi. \tag{2.54}$$

Here, X stands for sets of indices $\{\alpha,\beta,\ldots\}$. Q_X are (complex) coefficients and H_X the monomials spanning the local operator space. The expansion of $S_{\mathbf{R}}$ is analogous. The

[6] Gutzwiller's original ansatz (2.38) for the Hubbard model may seem incompatible with (2.52) (and the second condition introduced later), but actually only needs a trivial modification to work with the current formalism. (2.38) assigns states with zero, one, and two electrons the respective weights 1, 1, and g, which will not fulfill the conditions unless $g = 1$. Instead, one should choose an ansatz with (as yet undetermined) weights p_0, p_1, and p_2. Two of these parameters can then be solved for using the Gutzwiller conditions, so that the final wave function will again have a single free parameter equivalent to g.

[7] It may seem like a waste of time to have introduced the red-line diagrams, only to immediately throw out the first problematic term using (2.52). The real utility in the red-line diagrams is that they will let us argue about higher-order diagrams (which are harder to get rid of) with a minimum amount of handwaving.

ξ-product in (2.54) should be taken in some fixed but in principle arbitrary "ascending" order.

To evaluate Wick contractions, we define operators with certain indices "removed": For the monomials, this means

$$H_X^{(\alpha\beta\ldots)} = \begin{cases} 0 & \{\alpha,\beta,\ldots\} \not\subseteq X \\ \pm \prod\limits_{\xi\in X\setminus\{\alpha,\beta,\ldots\}} q_\xi & \{\alpha,\beta,\ldots\} \subseteq X \end{cases} \tag{2.55}$$

The sign depends on the number of exchanges that would be needed to move the factor $q_\alpha q_\beta \ldots$ to the front of H_X. As an example, we have (assuming no two indices are the same)

$$H_{\{\alpha,\beta,\gamma\}} = q_\alpha q_\beta q_\gamma, \tag{2.56}$$
$$H^{(\beta)}_{\{\alpha,\beta,\gamma\}} = -q_\alpha q_\gamma, \tag{2.57}$$
$$H^{(\beta\gamma)}_{\{\alpha,\beta,\gamma\}} = q_\alpha, \tag{2.58}$$
$$H^{(\delta)}_{\{\alpha,\beta,\gamma\}} = 0. \tag{2.59}$$

Using this definition, the first-order contraction (Fig. 2.4 (c)) can be written as

$$\langle \overbrace{Q_{\mathbf{R}} S_{\mathbf{R}'}} \rangle_0 = -\sum_\alpha \sum_\beta \langle q_{\mathbf{R}\alpha} q_{\mathbf{R}'\alpha'} \rangle_0 \, \langle Q^{(\alpha)}_{\mathbf{R}} \rangle_0 \, \langle S^{(\alpha')}_{\mathbf{R}'} \rangle_0 = 0, \tag{2.60}$$

which vanishes as the expectation value of a fermion-odd operator is zero[8]. Analogously,

$$\langle S^{(\alpha)}_{\mathbf{R}} \rangle_0 = \langle S^{(\alpha\beta\gamma)}_{\mathbf{R}} \rangle_0 = \langle S^{(\alpha\beta\gamma\delta\epsilon)}_{\mathbf{R}} \rangle_0 = \ldots = 0. \tag{2.61}$$

Thus, the total number of blue lines attached to each vertex (be it Q or a S) in a diagram must be *even*.

The second-order contraction (Fig. 2.4 (d)) is

$$\langle \overbrace{\overbrace{Q_{\mathbf{R}} S_{\mathbf{R}'}}} \rangle_0 = -\sum_{\alpha\neq\beta} \sum_{\alpha'\neq\beta'} \langle q_{\mathbf{R}\alpha} q_{\mathbf{R}'\alpha'} \rangle_0 \, \langle q_{\mathbf{R}\beta} q_{\mathbf{R}'\beta'} \rangle_0 \, \langle Q^{(\alpha\beta)}_{\mathbf{R}} \rangle_0 \, \langle S^{(\alpha'\beta')}_{\mathbf{R}'} \rangle_0. \tag{2.62}$$

This term is nonzero in general. However, there is still a way around actually having to calculate this diagram, as long as we place further restrictions on our variational wave function. This is the *second Gutzwiller conditions*, from which it will follow that second-order contractions of $S_{\mathbf{R}}$ also vanish. The condition is

$$\langle S_{\mathbf{R}} q_{\mathbf{R}\alpha} q_{\mathbf{R}\beta} \rangle_0 = 0 \Leftrightarrow \langle P^\dagger_{\mathbf{R}} P_{\mathbf{R}} q_{\mathbf{R}\alpha} q_{\mathbf{R}\beta} \rangle_0 = \langle q_{\mathbf{R}\alpha} q_{\mathbf{R}\beta} \rangle_0. \tag{2.63}$$

[8] The negative sign in (2.60) appears because we need to move $q_{\mathbf{R}'\alpha'}$ past the fermion-odd $Q^{(\alpha)}_{\mathbf{R}}$ (of course, the sum vanishes anyway).

While (2.63) is a *local* constraint, it also has consequences for the *nonlocal* contraction (2.62). Specifically, using both Gutzwiller constraints we have

$$0 = \langle S_{\mathbf{R}} q_{\mathbf{R}\alpha} q_{\mathbf{R}\beta} \rangle_0 = \langle S_{\mathbf{R}} \rangle_0 \langle q_{\mathbf{R}\alpha} q_{\mathbf{R}\beta} \rangle_0 + \langle \overbrace{S_{\mathbf{R}} q_{\mathbf{R}\alpha}} q_{\mathbf{R}\beta} \rangle_0 \tag{2.64}$$

$$= -\sum_{\gamma \neq \delta} \langle q_{\mathbf{R}\alpha} q_{\mathbf{R}\gamma} \rangle_0 \langle q_{\mathbf{R}\beta} q_{\mathbf{R}\delta} \rangle_0 \langle S_{\mathbf{R}}^{(\gamma\delta)} \rangle_0, \tag{2.65}$$

Introducing the matrices $\mathfrak{q}$ and $\mathfrak{S}$ with entries $[\mathfrak{q}]_{\beta\delta} = \langle q_{\mathbf{R}\beta} q_{\mathbf{R}\delta} \rangle_0$ and $[\mathfrak{S}]_{\gamma\delta} = \langle S_{\mathbf{R}}^{(\gamma\delta)} \rangle_0$ (with zeros on the diagonal), we can rewrite the condition as a matrix equation

$$0 = \mathfrak{q} \mathfrak{S} \mathfrak{q}^{\mathsf{T}}. \tag{2.66}$$

$\mathfrak{q}$ is nonsingular except in degenerate cases[9]. For the product to result in the zero matrix, $\mathfrak{S}$ must then also be the zero matrix, resulting in

$$\langle S_{\mathbf{R}}^{(\alpha\beta)} \rangle_0 = 0. \tag{2.67}$$

Accordingly, the second-order contraction (2.62) vanishes.

With the Gutzwiller conditions, we have eliminated all diagrams where an S is connected by fewer than four blue lines. We could try introducing conditions to eliminate higher-order contractions, but this turns out to be too restrictive: while we mentioned that the first Gutzwiller condition does not actually constrain the available wave functions, the second condition does (this will be important later when we apply the approximation to the bond fermion problem). The next set of contractions is fourth-order, so that a new Gutzwiller condition would require us to place restrictions on $\langle q_{\mathbf{R}\alpha} q_{\mathbf{R}\beta} q_{\mathbf{R}\gamma} q_{\mathbf{R}\delta} \rangle_0$: However, interaction terms are also quartic, so that constraining such terms is the opposite of what we want. If we were to go even further, we would eventually accumulate enough constraints so that only $S_{\mathbf{R}} = 0$ ($P = 1$) can fulfill all of them, bringing us back to a standard Slater determinant wave function.

Luckily, further constraints are not needed. Diagrams with four or more blue lines are instead eliminated by going to infinite dimensions.

2.3.2 Infinite dimensions

The physical basis of an expansion in the number of spatial dimensions is that the strength of nonlocal correlations decreases with the coordination number z of the lattice. This is illustrated by the following thought experiment: Regard two neighboring sites $\mathbf{R}$ and $\mathbf{R}'$. An electron hops onto $\mathbf{R}$ and is involved in an interaction process. How likely is it that the electron then hops to $\mathbf{R}'$ and interacts again? If the lattice connectivity is $z \gg 1$, the vast majority of paths the electron can take will *never* lead it to $\mathbf{R}'$. It is much more likely that the next interactions on $\mathbf{R}'$ will involve a completely unrelated set of electrons: Correlations between $\mathbf{R}$ and $\mathbf{R}'$ go to zero.

[9] $\mathfrak{q}$ is related to the local density matrix $\langle q_{\mathbf{R}\alpha}^\dagger q_{\mathbf{R}\beta} \rangle_0$ by exchange of rows. The density matrix can always be diagonalized by a Bogoliubov transform, and its eigenvalues are the occupation numbers of the fermionic modes. As long as no fermionic modes are totally (un-) occupied, the matrix is positive definite and thus has full rank.

A logical idea spawning from this is that to calculate expectation values at $\mathbf{R}$, we may be able to replace the rest of the lattice by some simple "bath" whose only role is to provide a source (and sink) for electrons, $\mathbf{R}$ being the only site where we need to explicitly take correlations into account. This is the idea behind dynamical mean-field theory [51], which provides many exact solutions for infinite-dimensional lattices. A similar thought process can be applied to the Gutzwiller wave function: a Gutzwiller wave function where the projection operator only acts on a single site would be trivial to solve through Wick's theorem, as no lattice sum needs to be performed.

We should now try to make these arguments precise. Roughly speaking, the Gutzwiller approximation can be thought of as a controlled expansion in $\langle q_{\mathbf{R}\alpha} q_{\mathbf{R}'\alpha'} \rangle_0$. To derive the scaling of these expectation values for fairly generic $|\Psi_0\rangle$, it suffices to take as an example a single band of fermions on a hypercubic lattice. We first derive a useful identity: assuming electron number conservation, we can write (with $n^0_{\mathbf{R}} = \langle c^\dagger_{\mathbf{R}} c_{\mathbf{R}} \rangle_0$)

$$\langle c^\dagger_{\mathbf{R}} c_{\mathbf{R}} \sum_{\mathbf{R}'} c^\dagger_{\mathbf{R}'} c_{\mathbf{R}'} \rangle_0 = n^0_{\mathbf{R}} N_e \tag{2.68}$$

$$= \sum_{\mathbf{R}'} \left[\langle c^\dagger_{\mathbf{R}} c_{\mathbf{R}} \rangle_0 \langle c^\dagger_{\mathbf{R}'} c_{\mathbf{R}'} \rangle_0 + \langle c^\dagger_{\mathbf{R}} c_{\mathbf{R}'} \rangle_0 \langle c_{\mathbf{R}} c^\dagger_{\mathbf{R}'} \rangle_0 \right] \tag{2.69}$$

$$= n^0_{\mathbf{R}} N_e + \sum_{\mathbf{R}'} \langle c^\dagger_{\mathbf{R}} c_{\mathbf{R}'} \rangle_0 (\delta_{\mathbf{R}\mathbf{R}'} - \langle c^\dagger_{\mathbf{R}'} c_{\mathbf{R}} \rangle_0) \tag{2.70}$$

$$= n^0_{\mathbf{R}} N_e + n^0_{\mathbf{R}} (1 - n^0_{\mathbf{R}}) + \sum_{\mathbf{R}' \neq \mathbf{R}} \left| \langle c^\dagger_{\mathbf{R}} c_{\mathbf{R}'} \rangle_0 \right|^2, \tag{2.71}$$

$$\Rightarrow \sum_{\mathbf{R}' \neq \mathbf{R}'} \left| \langle c^\dagger_{\mathbf{R}} c_{\mathbf{R}'} \rangle \right|^2 = n^0_{\mathbf{R}} (1 - n^0_{\mathbf{R}}) \tag{2.72}$$

The expectation value is calculated in two different ways. In the first line (2.68) we used that $\sum_{\mathbf{R}'} c^\dagger_{\mathbf{R}'} c_{\mathbf{R}'}$ is the operator of the total electron number, of which $|\Psi_0\rangle$ is an eigenstate with eigenvalue N_e. In (2.69) we instead evaluate the expectation value using Wick's theorem, where we explicitly separated the local and nonlocal contributions in (2.71).

The right-hand side of (2.72) is bounded, so the left-hand side must be as well. As a consequence, the sum over each "shell" of constant $l = \left|\mathbf{R} - \mathbf{R}'\right|$ (the norm taken in Manhattan distance, so that the shell corresponds to the l-nearest-neighbors) can also be bounded separately. As the number of neighbors increases in high dimensions, the correlation functions must decrease in turn.

The number of sites of each shell scales somewhat counterintuitively for large d. Experience might lead one to expect the that shell size scales $\sim l^{d-1}$, analogous to the surface area of a d-dimensional ball with radius l. However, this relation only holds for $l \gg d$, while we are in the opposite limit. For a typical $\mathbf{l} = \mathbf{R} - \mathbf{R}'$, the vast majority (specifically, $d - l \approx d \gg 1$) of the components l_i will be 0, while l of the components will be ± 1. Choosing these l components and multiplying by 2^l for each choice of sign, we get the approximate scaling

$$2^l \binom{d}{l} \approx 2^l \frac{d^l}{l!} \sim d^l. \tag{2.73}$$

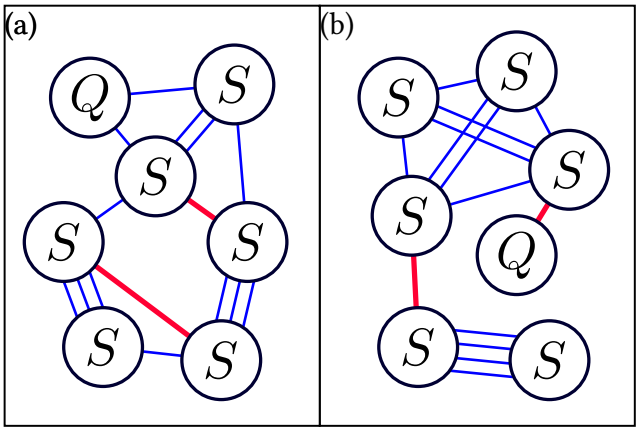

Figure 2.5: Two example diagrams of high order. The important difference is that Q is attached either through (a) two blue lines or (b) a red line.

As we are only interested in the leading d-dependence, we disregard d-independent terms[10]. As a result, we find that

$$\left|\langle c^\dagger_{\mathbf{R}} c_{\mathbf{R}'}\rangle_0\right| \sim d^{-\frac{|\mathbf{R}-\mathbf{R}'|}{2}}. \tag{2.74}$$

This rapid decay is the central feature of the infinite-dimensional limit, and will be used to eliminate the remaining nontrivial diagrams[11]. The same scaling relation as (2.74) can of course be derived for $\langle q_{\mathbf{R}\alpha} q_{\mathbf{R}'\alpha'}\rangle_0$ for any multiband system as well.

Let us first look at what this result means for the rest of the $m = 1$ term in the diagram series. A $2p$-order contraction gives us $2p$ factors of $d^{-\frac{l}{2}}$, so the sum is

$$\sum_{\mathbf{R}'\neq\mathbf{R}} \sum_{p\geq p_0} \langle \overbrace{Q_{\mathbf{R}} S_{\mathbf{R}'}}^{\times 2p}\rangle_0 \sim \sum_{l\geq 1} d^l \sum_{p\geq p_0} d^{-pl} \approx \sum_{l\geq 1} d^l d^{-p_0 l} \approx d^{1-p_0} \longrightarrow 0, \tag{2.75}$$

where we replaced the sum over sites by a sum over shells, with a factor d^l for the size of each shell. The sum vanishes because $p_0 = 2$ (lower-order diagrams were removed through the Gutzwiller conditions): the decay of the correlation functions wins out over the increase in shell sizes.

It only remains to demonstrate that the rest of the diagram series (with $m > 1$) behaves the same way. Two typical diagrams are shown in Fig. 2.5. These diagrams are leading-order, in the sense that each S has exactly four blue lines attached to it (if we were to remove any blue lines the diagram would be identically zero, and if we were to add any

[10] The exact number of l-nearest neighbors, valid for any d and l, is the hypergeometric sum $\sum_k \binom{d}{k}\binom{l-1}{k-1}2^k = 2d\ {}_2F_1(1-d, 1-l; 2; 2)$, the factors in the sum respectively corresponding to the number of ways to choose k nonzero components, the number of ways to distribute l steps over these components, and the factor for each sign.

[11] Of course, a small degree of isotropy is assumed in (2.74), meaning that $\left|\langle c^\dagger_{\mathbf{R}} c_{\mathbf{R}'}\rangle_0\right|$ should not vary too much on each individual shell. For example, if the wave function is taken to be a product of one-dimensional chains, increasing the number of dimensions will not influence the correlation functions inside each chain, and the scaling does not apply.

further ones it would vanish more quickly for $d \to \infty$). The only conceptual difference is the connection of Q: in diagram (a), Q has two blue lines (the minimum possible number) attached to it, while in (b) it has a red line attached to it.

Let us first consider diagram (a). Similar to the $m = 1$ case, there are essentially two competing effects for $d \to \infty$: correlation functions decrease, but the number of l-nearest-neighbors increases (note that the actual number of diagrams does not depend on the dimension). It remains to show that the first effect is stronger than the second. For this, the exact structure of the diagram is irrelevant. We start by counting blue lines. As there are two lines attached to Q and four to each S, the total number of blue lines is

$$B = \frac{2 + 4m}{2} = 1 + 2m. \tag{2.76}$$

Since the correlation functions rapidly decrease with distance, we can focus on the case where each blue line links nearest-neighbor sites (see for example (2.75), where the $l = 1$ term gave the leading contribution). We then get a factor of $d^{-\frac{1}{2}}$ for every line, or $d^{-B/2}$ in total.

Now for the combinatorial factor. We imagine placing down the S-vertices one by one. If an S *does not* have any red lines leading to it, we can put it at any nearest-neighbor site of a previously placed vertex; counting the number of nearest neighbors, we get a factor of $\sim d$. If it *does* have a red line attached to it, its position is fixed and the factor is unity. As a result, the total combinatorial factor is d^C, where

$$C = m - R \tag{2.77}$$

and R the number of red lines.

Putting these ingredients together, the diagram scales as

$$d^{C-B/2} = d^{m-R-\frac{1+2m}{2}} = d^{-\frac{1}{2}-R} \lesssim d^{-\frac{1}{2}} \to 0. \tag{2.78}$$

Here, the value of $R \geq 0$ is irrelevant. The analysis for diagram (b) is similar: The differences are that $B = 2m$, but that in turn we *must have* $R \geq 1$, so that diagram (b) also vanishes. In general, the only contribution that remains in infinite dimensions is the trivial $m = 0$ diagram, so that

$$\langle O_{\mathbf{R}} \rangle = \langle P_{\mathbf{R}}^\dagger O_{\mathbf{R}} P_{\mathbf{R}} \rangle_0. \tag{2.79}$$

2.3.3 Nonlocal expectation values

The above procedure lets us calculate local expectation values. However, a typical Hamiltonian also requires hopping expectation values of the form $\langle q_{\mathbf{R}\alpha} q_{\mathbf{R}'\alpha'} \rangle$ with $\mathbf{R} \neq \mathbf{R}'$. While we have demonstrated that such expectation values goes to zero, this *does not* mean that the kinetic energy vanishes, as the number of neighboring sites diverges in turn (for a thorough calculation of the kinetic energy in the Hubbard model in infinite dimensions see Ref. [79]). Our goal is to isolate the leading term, that is, we need the slowest-vanishing contribution as $d \to \infty$.

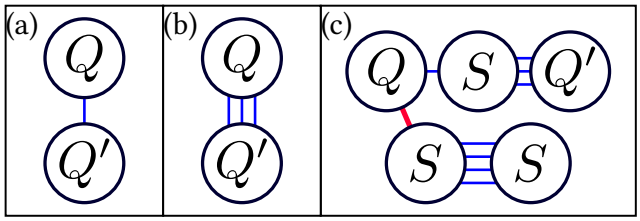

Figure 2.6: Example diagrams for the expansion of a nonlocal expectation value. The vertices Q and Q' here correspond to $Q_{\mathbf{R}\alpha}$ and $Q_{\mathbf{R}'\alpha'}$.

Luckily, we can introduce a similar diagram series as for the local expectation values, after which most arguments can be reused. Introducing the new set of operators

$$O_{\mathbf{R}\alpha} = P_{\mathbf{R}}^\dagger q_{\mathbf{R}\alpha} P_{\mathbf{R}}, \tag{2.80}$$

the diagram series now has *two* fixed vertices instead of one, and is shown in Fig. 2.6. As the $Q_{\mathbf{R}}$ are fermion-odd, they need to be connected by an odd number of blue lines. By analogous arguments as before, the lowest-order diagram in infinite dimensions is thus Fig. 2.6 (a), so that the final result is

$$\langle q_{\mathbf{R}\alpha} q_{\mathbf{R}'\alpha'} \rangle = \langle \overbrace{Q_{\mathbf{R}\alpha} Q_{\mathbf{R}'\alpha'}} \rangle_0. \tag{2.81}$$

2.3.4 Final result

To summarize, expectation values of the Gutzwiller wave function can be calculated exactly on infinite-dimensional lattices, provided the *Gutzwiller conditions*

$$\langle P_{\mathbf{R}}^\dagger P_{\mathbf{R}} \rangle_0 = 1, \tag{2.82}$$

$$\langle P_{\mathbf{R}}^\dagger P_{\mathbf{R}} q_{\mathbf{R}\alpha} q_{\mathbf{R}\beta} \rangle_0 = \langle q_{\mathbf{R}\alpha} q_{\mathbf{R}\beta} \rangle_0 \tag{2.83}$$

are enforced. Local expectation values are calculated as

$$\langle O_{\mathbf{R}} \rangle = \langle P_{\mathbf{R}}^\dagger O_{\mathbf{R}} P_{\mathbf{R}} \rangle_0, \tag{2.84}$$

which can be used to calculate particle densities, spin densities, interaction energies, etc. For $\mathbf{R} \neq \mathbf{R}'$ correlation functions vanish in infinite dimensions, but the leading term can be calculated as

$$\langle q_{\mathbf{R}\alpha} q_{\mathbf{R}'\alpha'} \rangle = \langle P_{\mathbf{R}}^\dagger q_{\mathbf{R}\alpha} P_{\mathbf{R}} P_{\mathbf{R}'}^\dagger q_{\mathbf{R}'\alpha'} P_{\mathbf{R}'} \rangle_0^1. \tag{2.85}$$

The superscript "1" on the expectation value indicates that one should only retain terms with a single Wick contraction between $\mathbf{R}$ and $\mathbf{R}'$, as higher-order contractions are subleading (while terms of all orders are nonzero for finite d, higher-order contractions should still be disregarded for a consistent expansion around the infinite-dimensional limit).

Finally, it is also important to understand that, except in special cases,

$$\langle q_{\mathbf{R}\alpha} q_{\mathbf{R}\beta} \rangle = \langle P_{\mathbf{R}}^\dagger q_{\mathbf{R}\alpha} q_{\mathbf{R}\beta} P_{\mathbf{R}}^\dagger \rangle_0 \neq \langle P_{\mathbf{R}}^\dagger P_{\mathbf{R}}^\dagger q_{\mathbf{R}\alpha} q_{\mathbf{R}\beta} \rangle_0 = \langle q_{\mathbf{R}\alpha} q_{\mathbf{R}\beta} \rangle_0, \tag{2.86}$$

since $q_{\mathbf{R}\beta}$ and $P_{\mathbf{R}}$ are not guaranteed to commute.

The expectation values (2.84–2.85) are usually reasonable approximations even in finite-dimensional lattices. While it is in theory possible to calculate corrections of order d^{-1}, to our knowledge this has only actually been carried out for the Hubbard model, where the diagram series can be simplified [38]. For our purposes, this does not seem necessary: the three sources of error are the restriction of the Hilbert space to the bond fermion subspace, the Gutzwiller variational ansatz, and the expansion in infinite dimensions. The first error will almost certainly be the largest for moderate J, which is where we expect most of the interesting magnetic dynamics. A more sophisticated treatment of the hard-core constraint than the Gutzwiller approximation is likely only worth it for $J \to \infty$, where the bond fermion approximation itself becomes exact.

The expressions in (2.82–2.85) are in principle easy to evaluate, since they do not contain any lattice sums. However, practical implementation can be challenging. For a system with F local fermion degrees of freedom, $P_{\mathbf{R}}$ is a complex matrix of size $2^F \times 2^F$. With a completely general ansatz for $P_{\mathbf{R}}$, one then has around $2 \cdot 4^F$ real parameters to optimize, not counting $|\Psi_0\rangle$.

For this general problem, we refer to the sophisticated algorithms developed in the literature [20, 69]. Luckily, in many situations it is possible to get reasonable results even with a much more restricted ansatz for $P_{\mathbf{R}}$. For example, Yao et al. [115] have $P_{\mathbf{R}}$ diagonal (in the fermion's natural basis), which reduces the number of parameters to 2^F and leads to a very efficient numerical solution. In our case the situation is even simpler, and much of the calculation can be performed analytically.

2.4 Gutzwiller approximation for bond fermion theory

The role of the Gutzwiller projection operator in our case is to project onto states with 0 or 1 bond fermions on each site. While this still leaves some leeway, we will further assume $P_{\mathbf{R}}$ to be hermitian ($P^\dagger = P$) and conserve the electron number: consequently, $P_{\mathbf{R}}$ should give zero when applied to a state with 2 or more bond fermions, and not mix between a- and b-fermions (a- and b-states have different electron amounts). However, it can still influence the relative weights of a- and b-states, or influence the magnetic moment (terms like $a^\dagger_{\mathbf{R}\uparrow} a_{\mathbf{R}\downarrow}$ are allowed in $P_{\mathbf{R}}$, and in fact needed to fulfill the Gutzwiller conditions).

We can now start using the results of the previous section. The first ingredient is to insert $a^\dagger_{\mathbf{R}\sigma} b^\dagger_{\mathbf{R}\tilde{\sigma}}$ into (2.83). This gives

$$\langle P^2_{\mathbf{R}} a^\dagger_{\mathbf{R}\sigma} b^\dagger_{\mathbf{R}\tilde{\sigma}} \rangle_0 = \langle a^\dagger_{\mathbf{R}\sigma} b^\dagger_{\mathbf{R}\tilde{\sigma}} \rangle_0. \tag{2.87}$$

The left-hand side is identically zero, as $a^\dagger b^\dagger$ creates a forbidden state that is projected out. However, the right-hand side is generally nonzero and may be energetically favorable were it not for the hard-core condition, as (2.32) contains pairing terms[12]. To satisfy the condition, we thus need to put a constraint on $|\Psi_0\rangle$:

$$0 = \langle a_{\mathbf{R}\sigma} b_{\mathbf{R}\tilde{\sigma}} \rangle_0 = \langle a^\dagger_{\mathbf{R}\sigma} b^\dagger_{\mathbf{R}\tilde{\sigma}} \rangle_0. \tag{2.88}$$

[12] These pairing terms are *nonlocal*, but without the hard-core constraint they would also cause nonvanishing *local* expectation values in the ground state.

This shows that (2.83) is indeed nontrivial to implement[13]. In practice, (2.88) is either automatically fulfilled because of some symmetry, or can be explictly enforced through a set of Lagrange multipliers $\Lambda_{\sigma\tilde{\sigma}}$ corresponding to each choice of spins in (2.88); how this works will be shown in Sec. 2.7.

We can now calculate $P_{\mathbf{R}}$ explicitly. While this usually involves minimizing the Gutzwiller variational energy, the simple form of the projection together with the Gutzwiller conditions allows us to solve for all remaining parameters. The calculation is easiest in the ($|\Psi_0\rangle$-dependent) eigenbasis of the local density matrix

$$\rho_{\mathbf{R}} = \begin{pmatrix} \rho_{\mathbf{R}a} & 0 \\ 0 & \rho_{\mathbf{R}b} \end{pmatrix}, \tag{2.89}$$

$$\rho_{\mathbf{R}a} = \begin{pmatrix} \langle a^\dagger_{\mathbf{R}\uparrow} a_{\mathbf{R}\uparrow}\rangle_0 & \langle a^\dagger_{\mathbf{R}\uparrow} a_{\mathbf{R}\downarrow}\rangle_0 \\ \langle a^\dagger_{\mathbf{R}\downarrow} a_{\mathbf{R}\uparrow}\rangle_0 & \langle a^\dagger_{\mathbf{R}\downarrow} a_{\mathbf{R}\downarrow}\rangle_0 \end{pmatrix}. \tag{2.90}$$

$\rho_{\mathbf{R}b}$ is defined similarly. There are no cross-terms $\langle a^\dagger_{\mathbf{R}\sigma} b_{\mathbf{R}\tilde{\sigma}}\rangle$, as this would violate electron conservation. We introduce a four-component fermion vector $\xi_{\mathbf{R}}$ as

$$\begin{pmatrix} a_{\mathbf{R}\uparrow} \\ a_{\mathbf{R}\downarrow} \\ b_{\mathbf{R}\uparrow} \\ b_{\mathbf{R}\downarrow} \end{pmatrix} = U_{\mathbf{R}} \xi_{\mathbf{R}}, \tag{2.91}$$

$$U_{\mathbf{R}} = \begin{pmatrix} U_{\mathbf{R}a} & 0 \\ 0 & U_{\mathbf{R}b} \end{pmatrix}, \tag{2.92}$$

$$\langle \xi^\dagger_{\mathbf{R}i} \xi_{\mathbf{R}j}\rangle_0 = \langle N_{\mathbf{R}i}\rangle_0 \delta_{ij}, \tag{2.93}$$

$$N_{\mathbf{R}i} = \xi^\dagger_{\mathbf{R}i} \xi_{\mathbf{R}i}. \tag{2.94}$$

While $\rho_{\mathbf{R}a}$ and $\rho_{\mathbf{R}b}$ can be diagonalized independently, we have combined them here to simplify the notation; the former two components of ξ correspond to a, the latter to b. The Latin indices i, j, are used to differentiate ξ from the vector v of Sec. 2.2, which contains both creation and annihilation operators, whereas ξ only holds annihilation operators. The unitary matrices $U_{\mathbf{R}a}$ and $U_{\mathbf{R}b}$ hold the eigenvectors of $\rho_{\mathbf{R}a}$ and $\rho_{\mathbf{R}b}$; more physically speaking, they are the two-dimensional spin-rotation matrices that respectively rotate the spins of the a- and b-fermions to the z-axis. In a general setting, these rotations do not have to be the same, as the spin polarizations of the a- and b-fermions can be different.

[13] For a nonhermitian $P_{\mathbf{R}}$, (2.88) could be avoided. In the hermitian case, the Gutzwiller operator acting on a forbidden state needs to give zero (schematically, $P\,|\text{forbidden}\rangle = 0$). This is not true for a nonhermitian operator, as then we only need $P\,|\text{forbidden}\rangle \propto |\text{allowed}\rangle$ (such a term would have to violate bond fermion number conservation, but *not necessarily* electron conservation). One can convince oneself that the left-hand side of (2.87), $\langle P^\dagger_{\mathbf{R}} P_{\mathbf{R}} a^\dagger_{\mathbf{R}\sigma} b^\dagger_{\mathbf{R}\tilde{\sigma}}\rangle_0$, is then nonzero in general. However, $\langle a^\dagger_{\mathbf{R}\sigma} b^\dagger_{\mathbf{R}\tilde{\sigma}}\rangle = \langle P^\dagger_{\mathbf{R}} a^\dagger_{\mathbf{R}\sigma} b^\dagger_{\mathbf{R}\tilde{\sigma}} P_{\mathbf{R}}\rangle_0$ (see (2.84)) would still vanish, as implied by the hard-core interaction.
Including such terms would make the analysis more complicated for questionable gain (the main error will likely always be in the bond fermion mapping itself, not in the Gutzwiller approximation). Our choice of $P_{\mathbf{R}}$ (and $|\Psi_0\rangle$) is the minimal one that still allows for magnetic polarization of the bond fermions.

In this diagonal basis, the second Gutzwiller condition implies a similarly diagonal form for $P_{\mathbf{R}}$, meaning that it can be written solely in terms of the number operators $N_{\mathbf{R}i}$[14]:

$$P_{\mathbf{R}} = p_{\mathbf{R}0} \prod_i \overline{N}_{\mathbf{R}i} + \sum_i p_{\mathbf{R}i}\, N_{\mathbf{R}i} \prod_{j\neq i} \overline{N}_{\mathbf{R}j}, \tag{2.95}$$

$$\overline{N}_{\mathbf{R}i} = 1 - N_{\mathbf{R}i}. \tag{2.96}$$

The first term is a projector onto the empty state at $\mathbf{R}$, while each term in the sum projects onto a state with exactly one ξ at $\mathbf{R}$. $p_{\mathbf{R}0}$ and the $p_{\mathbf{R}i}$ are parameters that we need to solve for. This is done by explicitly computing the expectation values in the Gutzwiller conditions (2.82–2.83), which after substituting (2.95) result in the system of equations

$$p_{\mathbf{R}0}^2 \prod_i \langle \overline{N}_{\mathbf{R}i}\rangle_0 + \sum_i p_{\mathbf{R}i}^2 \langle N_{\mathbf{R}i}\rangle_0 \prod_{j\neq i} \langle \overline{N}_{\mathbf{R}j}\rangle_0 = 1, \tag{2.97}$$

$$p_{\mathbf{R}i}^2 \langle N_{\mathbf{R}i}\rangle_0 \prod_{j\neq i} \langle \overline{N}_{\mathbf{R}j}\rangle_0 = \langle N_{\mathbf{R}i}\rangle_0. \tag{2.98}$$

The first line is the result of the first Gutzwiller condition; the second line follows from inserting $\xi^\dagger_{\mathbf{R}i}\xi_{\mathbf{R}i}$ into the second Gutzwiller condition. Another straightforward computation then gives

$$p_{\mathbf{R}0}^2 = \left(1 - \sum_i \langle N_{\mathbf{R}i}\rangle_0\right)\left(\prod_i \langle \overline{N}_{\mathbf{R}i}\rangle_0\right)^{-1}, \tag{2.99}$$

$$p_{\mathbf{R}i}^2 = \left(\prod_{j\neq i} \langle \overline{N}_{\mathbf{R}j}\rangle_0\right)^{-1}, \tag{2.100}$$

so that $P_{\mathbf{R}}$ is determined completely.

We can evaluate expectation values of the Gutzwiller state using (2.84–2.85). For this we only need quadratic expectation values, as the variational energy (2.32) does not contain any quartic terms (the hard-core condition is taken care of by form of the Gutzwiller operator). Furthermore, it turns out that the local quadratic expectation values are completely unchanged from the uncorrelated state. For $i = j$ we have

$$\langle N_{\mathbf{R}i}\rangle = \langle P_{\mathbf{R}} N_{\mathbf{R}i} P_{\mathbf{R}}\rangle_0 = \langle P_{\mathbf{R}}^2 N_{\mathbf{R}i}\rangle_0 = \langle N_{\mathbf{R}i}\rangle_0, \tag{2.101}$$

as $N_{\mathbf{R}i}$ commutes with $P_{\mathbf{R}}$ because of (2.95). For $i \neq j$ we get

$$\langle \xi^\dagger_{\mathbf{R}i}\xi_{\mathbf{R}j}\rangle = \langle P_{\mathbf{R}}\xi^\dagger_{\mathbf{R}i}\xi_{\mathbf{R}j}P_{\mathbf{R}}\rangle_0 = 0 = \langle \xi^\dagger_{\mathbf{R}i}\xi_{\mathbf{R}j}\rangle_0, \tag{2.102}$$

The second expression vanishes because, counting the contributions of the $P_{\mathbf{R}}$ as well, the indices i and j appear an odd number of times. Accordingly, in every Wick contraction

[14] The only other terms that project on the allowed subspace and conserve the electron number would be $p_{12}\xi^\dagger_1\xi^\dagger_2\overline{N}_3\overline{N}_4$, $p_{34}\xi^\dagger_3\xi^\dagger_4\overline{N}_1\overline{N}_2$, and their complex conjugates, where p_{12} and p_{34} are undetermined parameters (we suppressed the site index). Inserting e.g. $\xi^\dagger_2\xi_1$ into the second Gutzwiller can then be shown to give $0 = \langle\xi^\dagger_2\xi_1\rangle_0 = \langle P^2\xi^\dagger_2\xi_1\rangle_0 \propto p_{12} \Rightarrow p_{12} = 0$.

there must be a factor $\langle \xi^\dagger_{\mathbf{R}i} \xi_{\mathbf{R}k} \rangle_0$ with $i \neq k$ that vanishes by (2.93). The same holds for anomalous terms, so that all in all we have

$$\langle q_{\mathbf{R}\alpha} q_{\mathbf{R}\beta} \rangle = \langle q_{\mathbf{R}\alpha} q_{\mathbf{R}\beta} \rangle_0. \tag{2.103}$$

The q can stand for any ξ, or for any a or b by reversing the unitary transformation.

The nonlocal terms are slightly more work. For these, we need the operators

$$P_{\mathbf{R}} \xi_{\mathbf{R}i} P_{\mathbf{R}} = p_{\mathbf{R}i} p_{\mathbf{R}0} \xi_{\mathbf{R}i} \prod_{j \neq i} \overline{N}_{\mathbf{R}j}. \tag{2.104}$$

The right-hand side follows easily from $\xi_{\mathbf{R}i} \overline{N}_{\mathbf{R}i} = 0$ and similar relations. (2.85) then gives

$$\langle \xi^\dagger_{\mathbf{R}i} \xi_{\mathbf{R}'i'} \rangle = \langle P_{\mathbf{R}} \xi^\dagger_{\mathbf{R}i} P_{\mathbf{R}} P_{\mathbf{R}'} \xi_{\mathbf{R}'i'} P_{\mathbf{R}'} \rangle^1_0 \tag{2.105}$$

$$= \left[p_{\mathbf{R}i} p_{\mathbf{R}0} \prod_{j \neq i} \langle \overline{N}_{\mathbf{R}j} \rangle_0 \right] \left[p_{\mathbf{R}'i'} p_{\mathbf{R}'0} \prod_{j' \neq i'} \langle \overline{N}_{\mathbf{R}'j'} \rangle_0 \right] \langle \xi^\dagger_{\mathbf{R}i} \xi_{\mathbf{R}'i'} \rangle_0 \tag{2.106}$$

$$= \sqrt{\zeta}_{\mathbf{R}i} \sqrt{\zeta}_{\mathbf{R}'i'} \langle \xi^\dagger_{\mathbf{R}i} \xi_{\mathbf{R}'i'} \rangle_0, \tag{2.107}$$

$$\sqrt{\zeta}_{\mathbf{R}i} = \sqrt{\frac{1 - \sum_j \langle N_{\mathbf{R}j} \rangle_0}{1 - \langle N_{\mathbf{R}i} \rangle_0}}. \tag{2.108}$$

It follows from (2.104) that $\xi^\dagger_{\mathbf{R}i}$ and $\xi_{\mathbf{R}'i'}$ need to be contracted with each other. Thus, the hopping expectation values are *renormalized* (by renormalization factors $\sqrt{\zeta}$) compared to the uncorrelated wave function. The same is true for the anomalous hopping terms:

$$\langle \xi_{\mathbf{R}i} \xi_{\mathbf{R}'i'} \rangle = \sqrt{\zeta}_{\mathbf{R}i} \sqrt{\zeta}_{\mathbf{R}'i'} \langle \xi_{\mathbf{R}i} \xi_{\mathbf{R}'i'} \rangle_0. \tag{2.109}$$

It is instructive to check some limiting values of $\sqrt{\zeta}$. For example, the hopping renormalizes to zero when the bond fermion density (the sum in the numerator) becomes unity. On the other hand, if only a single one of the $\langle N_{\mathbf{R}i} \rangle$ is finite, then numerator and denominator cancel and the hopping is not renormalized at all. This is also expected because alike fermions do not interact. Note that the expression in (2.108) is the same as the renormalization in Kotliar and Ruckenstein's slave boson theory when applied to a system with four fermion degrees of freedom [62].

It is now time to reverse the unitary transformation and go back to a and b. We define the spin- and species-dependent renormalization matrix $\sqrt{Z}_{\mathbf{R}}$ as

$$\sqrt{Z}_{\mathbf{R}} = U_{\mathbf{R}} \sqrt{\zeta}_{\mathbf{R}} U^\dagger_{\mathbf{R}} = \begin{pmatrix} \sqrt{Z}_{\mathbf{R}a} & 0 \\ 0 & \sqrt{Z}_{\mathbf{R}b} \end{pmatrix}, \tag{2.110}$$

where $\sqrt{\zeta}_{\mathbf{R}}$ is the matrix with the $\sqrt{\zeta}_{\mathbf{R}i}$ on the diagonal. $\sqrt{Z}_{\mathbf{R}a}$ and $\sqrt{Z}_{\mathbf{R}b}$ are again two-dimensional matrices, as a- and b-fermions are not mixed. This allows us to calculate inter-site expectation values of the bond fermions as

$$\langle a^\dagger_{\mathbf{R}\sigma} a_{\mathbf{R}'\sigma'} \rangle = \sum_{\tilde{\sigma}\tilde{\sigma}'} \left[\sqrt{Z}^\dagger_{\mathbf{R}a} \right]_{\tilde{\sigma}\sigma} \left[\sqrt{Z}_{\mathbf{R}'a} \right]_{\sigma'\tilde{\sigma}'} \langle a^\dagger_{\mathbf{R}\tilde{\sigma}} a_{\mathbf{R}'\tilde{\sigma}'} \rangle_0, \tag{2.111}$$

$$\langle a^\dagger_{\mathbf{R}\sigma} b^\dagger_{\mathbf{R}'\sigma'} \rangle = \sum_{\tilde{\sigma}\tilde{\sigma}'} \left[\sqrt{Z}^\dagger_{\mathbf{R}a} \right]_{\tilde{\sigma}\sigma} \left[\sqrt{Z}^\dagger_{\mathbf{R}'b} \right]_{\tilde{\sigma}'\sigma'} \langle a^\dagger_{\mathbf{R}\tilde{\sigma}} b^\dagger_{\mathbf{R}'\tilde{\sigma}'} \rangle_0, \tag{2.112}$$

etc.

Finally, we can write down the energy (2.32) of the Gutzwiller state. The forms of H_J and $H_{\mathbf{B}}$ are unchanged as they only involve local expectation values. From (2.111-2.112), we get for the hopping Hamiltonian

$$\langle H_t \rangle = -\sum_{\mathbf{R}\mathbf{R}'} t_{\mathbf{R}\mathbf{R}'} \left\langle v_{\mathbf{R}}^\dagger \sqrt{\overline{Z}}_{\mathbf{R}}^\dagger W_{\mathbf{R}}^\dagger W_{\mathbf{R}'} \sqrt{\overline{Z}}_{\mathbf{R}'} v_{\mathbf{R}'} \right\rangle_0, \tag{2.113}$$

$$\sqrt{\overline{Z}}_{\mathbf{R}} = \begin{pmatrix} \sqrt{Z}^*_{\mathbf{R}a} & 0 \\ 0 & \sqrt{Z}_{\mathbf{R}b} \end{pmatrix}. \tag{2.114}$$

All terms in this expression depend only on the uncorrelated wave function, i.e. given a specific $W_{\mathbf{R}}$ and $|\Psi_0\rangle$ we can calculate $\sqrt{Z}_{\mathbf{R}}$ and with it the energy. This expression forms the basis of the later practical implementation.

2.5 Alternative methods

The derivation of the Gutzwiller approximation was somewhat involved; there are of course simpler methods to approximately take the hard-core interaction into account. At moderate to large J (where magnetic transitions appear), the density of bond fermions should be rather low, which can be exploited. We will describe two approximations, describing their original justifications and how they can be accommodated in our formalism: one is the approach of Jurecka and Brenig, and the other is to ignore the hard-core nature of the fermions as much as possible. Later on in Sec. 2.6, we will compare the results of the methods in the simplest possible calculation. However, first of all we need to discuss what we call *physicality conditions*, and what restrictions they place on approximations.

2.5.1 Physicality of expectation values

Let us try to evaluate how electrons are distributed over $\mathbf{k}$-modes. First we define the "Green functions"

$$G_{\sigma\sigma'}(\mathbf{R}, \mathbf{R}') = \langle c_{\mathbf{R}\sigma}^\dagger c_{\mathbf{R}'\sigma'} \rangle, \tag{2.115}$$

$$G(\mathbf{R}, \mathbf{R}') = G_{\uparrow\uparrow}(\mathbf{R}, \mathbf{R}') + G_{\downarrow\downarrow}(\mathbf{R}, \mathbf{R}'). \tag{2.116}$$

For $\mathbf{R} = \mathbf{R}'$, we can use $G_{\sigma\sigma'}$ to calculate electron and spin densities (G is the total electron density). To simplify the demonstration, we can here restrict ourselves to the paramagnetic and translation invariant case (i.e. $s_{\mathbf{R}} = 1$, $\mathbf{t}_{\mathbf{R}} = 0$), where we have

$$\langle c_{\mathbf{R}\uparrow}^\dagger c_{\mathbf{R}'\uparrow} \rangle = \langle c_{\mathbf{R}\downarrow}^\dagger c_{\mathbf{R}'\downarrow} \rangle, \tag{2.117}$$

$$G_{\sigma\sigma'}(\mathbf{R}, \mathbf{R}') = \frac{1}{2} G(\mathbf{R} - \mathbf{R}') \delta_{\sigma\sigma'}, \tag{2.118}$$

$$G(\mathbf{R} - \mathbf{R}') = 2\langle c_{\mathbf{R}\uparrow}^\dagger c_{\mathbf{R}'\uparrow} \rangle. \tag{2.119}$$

From Sec. 2.2, we find that G is given through two different expressions depending on $\mathbf{R}$ and $\mathbf{R}'$. For $\mathbf{R} \neq \mathbf{R}'$, (2.28) should be used. The result is

$$G(\mathbf{R}-\mathbf{R}') = 1 + \langle b^\dagger_{\mathbf{R}\uparrow} b_{\mathbf{R}'\uparrow}\rangle - \langle a^\dagger_{\mathbf{R}'\downarrow} a_{\mathbf{R}\downarrow}\rangle - \langle b^\dagger_{\mathbf{R}\uparrow} a^\dagger_{\mathbf{R}'\downarrow}\rangle - \langle a_{\mathbf{R}\downarrow} b_{\mathbf{R}'\uparrow}\rangle \tag{2.120}$$

$$= G'(\mathbf{R}-\mathbf{R}'). \tag{2.121}$$

We introduced the "nonlocal Green function" G' in the second line, which we understand to be defined through the same expression even for $\mathbf{R} = \mathbf{R}'$. It will give the $\mathbf{k}$-dependence of the electron occupation numbers. Meanwhile, for the "true" Green function we have (using (2.24))

$$G(\mathbf{R}-\mathbf{R}') = \begin{cases} G'(\mathbf{R}-\mathbf{R}') & \mathbf{R} \neq \mathbf{R}' \\ 1 - \langle a^\dagger_{\mathbf{R}} a_{\mathbf{R}}\rangle + \langle b^\dagger_{\mathbf{R}} b_{\mathbf{R}}\rangle & \mathbf{R} = \mathbf{R}' \end{cases}. \tag{2.122}$$

One can see that in general, $G \neq G'$ for $\mathbf{R} = \mathbf{R}'$ (note that (2.122) has implicit spin sums in the expectation values). Due to the hard-core fermion interaction, expectation values of pairing terms like $\langle b^\dagger_{\mathbf{R}\uparrow} a^\dagger_{\mathbf{R}\downarrow}\rangle$ must vanish, with which (2.120) gives

$$G(\mathbf{0}) = G'(\mathbf{0}) - \langle a^\dagger_{\mathbf{R}\uparrow} a_{\mathbf{R}\uparrow}\rangle + \langle b^\dagger_{\mathbf{R}\uparrow} b_{\mathbf{R}\uparrow}\rangle \tag{2.123}$$

We get the $\mathbf{k}$-space occupation numbers by Fourier transforming G:

$$\langle c^\dagger_{\mathbf{k}} c_{\mathbf{k}}\rangle = G(\mathbf{k}) \tag{2.124}$$

$$= \sum_{\mathbf{R}} e^{i\mathbf{k}\mathbf{R}} G(\mathbf{R}). \tag{2.125}$$

This sum can be split into a local and a nonlocal part, resulting in

$$G(\mathbf{k}) = \sum_{\mathbf{R}\neq\mathbf{0}} e^{i\mathbf{k}\mathbf{R}} G'(\mathbf{R}) + G(\mathbf{R}=\mathbf{0}) \tag{2.126}$$

$$= G'(\mathbf{k}) - G'(\mathbf{R}=\mathbf{0}) + G(\mathbf{R}=\mathbf{0}). \tag{2.127}$$

The number of electrons in the $\mathbf{k}$-mode is thus given by $G'(\mathbf{k})$, with the second and third term giving a constant offset.

A subtle but important consequence of (2.127) is that we need to be careful about how to enforce the hard-core condition on the bond fermions. $G(\mathbf{k})$ gives the total number of electrons in a momentum state $\mathbf{k}$, so clearly

$$0 \leq G(\mathbf{k}) \leq 2. \tag{2.128}$$

This physicality condition is automatically enforced as long as all bond fermion expectation values are evaluated on an *admissible* state, meaning one that does not include any double occupancies. For a generic state however, or when approximations are made, (2.127) can lead to violations of (2.128) and result in negative or too-large occupation numbers. This is clearly undesirable and should be kept in mind when solving the system approximately. One can also derive similar physicality conditions for the spin densities

(they should be bounded by $\pm 1/2$), which come into play once magnetic order is added to the system.

While we have been unable to prove that the Gutzwiller approximation of Sec. 2.3 generally fulfills the physicality condition, from the limit of infinite dimensions we consider this to be sensible. Since the Gutzwiller approximation is exact in infinite dimensions, it is sure to produce a state fulfilling (2.128). As the dimensionality enters the approximation only indirectly through the density of states, we expect the physicality rule to hold also in finite dimensions. Furthermore, we have not found any violations of physicality in our numerical investigations.

2.5.2 The method of Jurecka and Brenig

A different bond fermion method was introduced by Jurecka and Brenig [53]. Here, the translation between electrons and bond particles happens entirely on the operator level. Instead of choosing a particular ground state $|\Omega\rangle_{\mathbf{R}}$, the bond particle operators act on a vacuum state that does not correspond to any state in the original Hilbert space. All local states of the Kondo lattice are treated on a similar footing by introducing bond bosons $\tilde{s}_{\mathbf{R}}^{\dagger}$ and $\tilde{\mathbf{t}}_{\mathbf{R}}^{\dagger}$ to generate the singlet $|S\rangle_{\mathbf{R}}$ and the triplet $|\mathbf{T}\rangle_{\mathbf{R}}$ (we use the tildes to differentiate these operators from the ones in our own derivation). The result of the procedure is an exact (but interacting) mapping of the Kondo lattice model, provided the physicality condition

$$1 = \tilde{a}_{\mathbf{R}}^{\dagger}\tilde{a}_{\mathbf{R}} + \tilde{b}_{\mathbf{R}}^{\dagger}\tilde{b}_{\mathbf{R}} + \tilde{s}_{\mathbf{R}}^{\dagger}\tilde{s}_{\mathbf{R}} + \tilde{\mathbf{t}}_{\mathbf{R}}^{\dagger}\tilde{\mathbf{t}}_{\mathbf{R}} \tag{2.129}$$

is enforced (each site must be in exactly one physical state).

For actual calculations, the bosons were considered to be condensed, with (2.129) fulfilled on average. The condensation amplitudes $\langle\tilde{s}_{\mathbf{R}}\rangle$ and $\langle\tilde{\mathbf{t}}_{\mathbf{R}}\rangle$ correspond to our parameters $s_{\mathbf{R}}$ and $\mathbf{t}_{\mathbf{R}}$ from Sec. 2.2. However, unlike our description, these amplitudes are not normalized to unity. Instead of (2.10), the condition (2.129) results in

$$\left|\langle\tilde{s}_{\mathbf{R}}\rangle\right|^2 + \left|\langle\tilde{\mathbf{t}}_{\mathbf{R}}\rangle\right|^2 = 1 - \langle\tilde{a}_{\mathbf{R}}^{\dagger}\tilde{a}_{\mathbf{R}}\rangle + \langle\tilde{b}_{\mathbf{R}}^{\dagger}\tilde{b}_{\mathbf{R}}\rangle. \tag{2.130}$$

The kinetic energy contribution is quadratic in $\langle\tilde{s}_{\mathbf{R}}\rangle$ and $\langle\tilde{\mathbf{t}}_{\mathbf{R}}\rangle$, compare (2.30). The smaller values of these amplitudes thus result in an automatic renormalization of the band structure.

For an equivalent calculation in the language of the present paper, we normalize the parameters to unity as in the main text, but use the much simpler definition

$$\sqrt{Z}_{\mathbf{R}} = \sqrt{1 - \langle a_{\mathbf{R}}^{\dagger}a_{\mathbf{R}}\rangle_0 + \langle b_{\mathbf{R}}^{\dagger}b_{\mathbf{R}}\rangle_0}, \tag{2.131}$$

with no matrix structure in spin or bond fermion space. This result can alternatively be derived from our own formulation by treating the hard-core constraint using Barnes' slave boson mean-field theory [12, 13] instead of the Gutzwiller approximation.

(2.131) effectively corresponds to neglecting the denominator in (2.108). One can see that the Jurecka-Brenig approximation leads to a stronger renormalization of the hopping matrix elements than the Gutzwiller approximation, as the role of the denominator is to

"divide out" the self-interaction of equal-state fermions. As this correction is not present in the Jurecka-Brenig method, it will tend to distribute the bond fermions more evenly in spin space, i.e. paramagnetism is favored.

One should note that this derivation does not prescribe any specific technique on how to handle the "forbidden" expectation values describing local pair creation. They were implicitly accepted by Jurecka and Brenig, although one could equally well introduce the conditions (2.88) here as well. Later on we will implement both methods and compare their results to that of the Gutzwiller approximation.

2.5.3 "Ad-hoc" neglecting the hard-core interaction

The first approximation proposed [35] is even simpler, and consists of simply replacing the hard-core fermions with normal fermions. The variational energy is then minimized by an ordinary Slater determinant wave function. Such an approximation seems reasonable as long as the bond fermion density ρ_{BF} is not too large: the probability of bond fermions meeting is approximately ρ_{BF}^2.

However, it was soon recognized that some modifications were required to recover the expected band structure for general electron densities n_c [34]. In our language, the modifications can be interpreted as a consequence of the physicality condition in Sec. 2.5.1: numerically, one finds that (2.128) is not fulfilled otherwise, which precludes reasonable physical interpretation.

The method that was used to remedy this is in some sense the most straightforward. Namely, one can check from (2.121) that the physicality rule holds for G' by itself even on inadmissible states, meaning that

$$0 \leq G'(\mathbf{k}) \leq 2 \tag{2.132}$$

no matter whether the hard-core condition is enforced. This means that we can fulfill the physicality condition by requiring

$$G(\mathbf{k}) = G'(\mathbf{k}) \Leftrightarrow G(\mathbf{R}=\mathbf{0}) = G'(\mathbf{R}=\mathbf{0}), \tag{2.133}$$

which can be enforced through a Lagrange multiplier [35]. This choice is purely for convenience: there is no reason (2.133) should hold (and it does not hold in e.g. the Gutzwiller approach), but requiring it does fix the more pressing problem of unphysical expectation values. For this reason, we find "ad-hoc" to be an appropriate description of the method.

(2.133) can be phrased somewhat differently: in the references, the condition was instead interpreted as enforcing consistency between "two ways of counting the electrons". Specifically, we have

$$N_e = N\,G(\mathbf{R}=\mathbf{0}) = \sum_{\mathbf{R}} \left[1 - \langle a_{\mathbf{R}}^\dagger a_{\mathbf{R}}\rangle + \langle b_{\mathbf{R}}^\dagger b_{\mathbf{R}}\rangle\right], \tag{2.134}$$

$$N_e' = N\,G'(\mathbf{R}=\mathbf{0}) = \sum_{\mathbf{R}} \langle v_{\mathbf{R}}^\dagger W_{\mathbf{R}}^\dagger W_{\mathbf{R}} v_{\mathbf{R}}\rangle, \tag{2.135}$$

$$\Rightarrow N_e = N_e'. \tag{2.136}$$

N_e is the "correct" electron number, and N_e' the "incorrect" one (i.e., calculated as if (2.28) held also for local expectation values). However, in our calculation N_e' is more or less meaningless (it has no real physical interpretation), so we find this line of reasoning to be somewhat dangerous as well.

In the presence of magnetic order, we should in principle introduce separate physicality rules and Lagrange multipliers for each inequivalent site and spin direction; (2.136) is only an "averaged" form of the constraints. However, for reasonable results this averaged form seems to be enough. This was the approach in Ref. [33], and will also be used in Chapter 5. Finally, it should also be noted that the "ad-hoc" method explicitly *requires* the local pairing terms to be nonzero: (2.136) cannot be fulfilled otherwise, as can be shown by comparing (2.121) and (2.122). For example, for (2.123) it was assumed that pairing terms vanish, which results in an explicit contradiction with (2.133).

2.6 Preliminary analytic calculation

Generally speaking, bond fermion calculations require performing momentum integrals and solving for the variational parameters, which is not possible analytically. An exception to this is the simplest possible case with no magnetic polarization ($\mathbf{t}_\mathbf{R} = 0$), a half-filled conduction band ($n_c = 1$), and a flat density of states (with half-bandwidth D). In this case, only a single (transcendental) function needs to be inverted at the end of the calculation. As this calculation also helps to build some intuition for the results of the bond fermion method in more general cases, we will present it here. Further, it already allows us to demonstrate some properties of each of the three methods presented before.

Let us first use the Gutzwiller approximation. Assuming that $|\Psi_0\rangle$ has the above symmetries, one can easily convince oneself that the density matrix $\rho_\mathbf{R}$ is proportional to the unit matrix,

$$\langle a^\dagger_{\mathbf{R}\sigma} a_{\mathbf{R}\sigma}\rangle_0 = \langle b^\dagger_{\mathbf{R}\sigma} b_{\mathbf{R}\sigma}\rangle_0 = \text{const.} = \frac{\rho_\mathrm{BF}}{4}, \tag{2.137}$$

$$\langle a^\dagger_{\mathbf{R}\sigma} a_{\mathbf{R}\bar{\sigma}}\rangle_0 = \langle b^\dagger_{\mathbf{R}\sigma} b_{\mathbf{R}\bar{\sigma}}\rangle_0 = 0, \tag{2.138}$$

and that condition (2.88) is automatically fulfilled[15]. $\rho_\mathrm{BF} < 1$ is the total bond fermion density. Following from this, $\sqrt{Z} = \sqrt{\zeta}$ is also proportional to the unit matrix, (2.108) giving

$$\sqrt{Z} = \sqrt{\frac{1-\rho_\mathrm{BF}}{1-\rho_\mathrm{BF}/4}}. \tag{2.139}$$

[15] In bond fermion language, particle-hole symmetry schematically corresponds to exchanging $a \leftrightarrow b$, so that $\langle ab\rangle = \langle ba\rangle = -\langle ab\rangle = 0$.

The Gutzwiller approximation thus gives a simple multiplicative renormalization of the kinetic energy, albeit of a different form from that of Jurecka and Brenig. After inserting $s_{\mathbf{R}} = 1$ into (2.30), the kinetic energy (2.113) can then be simplified to

$$\langle H_t \rangle = -\sum_{\mathbf{R}\mathbf{R}'\sigma} \frac{Z t_{\mathbf{R}\mathbf{R}'}}{2} \left\langle v^\dagger_{\mathbf{R}\sigma} (\tau_0 - \sigma\tau_x) v_{\mathbf{R}'\sigma} \right\rangle_0, \tag{2.140}$$

$$v_{\mathbf{R}\sigma} = \begin{pmatrix} a^\dagger_{\mathbf{R}\bar{\sigma}} & b_{\mathbf{R}\sigma} \end{pmatrix}, \tag{2.141}$$

The spin-directions are thus decoupled: in the absence of magnetism, the bond fermion spin is conserved in both hopping and pair production process. Adding the interaction energy and performing a Fourier transform, we find that the energy expectation value is

$$E(|\Psi_0\rangle) = \langle H \rangle = \sum_{\mathbf{k}\sigma} \left\langle v^\dagger_{\mathbf{k}\sigma} \left[-\frac{3}{4} J \tau_z + \frac{Z\epsilon_{\mathbf{k}}}{2} (\tau_0 - \sigma\tau_x) \right] v_{\mathbf{k}\sigma} \right\rangle_0 + \frac{3}{4} J. \tag{2.142}$$

The final constant term comes from inverting two sets of $a^\dagger_{\mathbf{R}\sigma}$ operators.

To minimize E over $|\Psi_0\rangle$, one must take into account that Z is itself a function of $|\Psi_0\rangle$ through ρ_{BF}. To solve this problem, one introduces an *effective Hamiltonian* [115]: E depends on $|\Psi_0\rangle$ through the expectation values of a set of operators $\{A_i\}$, with

$$\langle A_i \rangle_0 = \frac{\langle \Psi_0 | A_i | \Psi_0 \rangle}{\langle \Psi_0 | \Psi_0 \rangle}. \tag{2.143}$$

Differentiating E (with respect to $\langle \Psi_0 |$ for convenience) and setting the result to zero, we have

$$0 = \frac{\mathrm{d}E\left(\{\langle A_i \rangle_0\}\right)}{\mathrm{d}\langle \Psi_0 \,|} = \sum_i \frac{\partial E}{\partial \langle A_i \rangle_0} \frac{\mathrm{d}\langle A_i \rangle_0}{\mathrm{d}\langle \Psi_0 \,|} \tag{2.144}$$

$$= \frac{1}{\langle \Psi_0 | \Psi_0 \rangle} \sum_i \frac{\partial E}{\partial \langle A_i \rangle_0} \left[A_i \,|\Psi_0\rangle - \langle A_i \rangle_0 \,|\Psi_0\rangle \right]. \tag{2.145}$$

The right-hand side can be identified as an eigenvalue equation with an effective Hamiltonian H_{eff} and an effective energy E_{eff}:

$$0 = H_{\mathrm{eff}} \,|\Psi_0\rangle - E_{\mathrm{eff}} \,|\Psi_0\rangle, \tag{2.146}$$

$$H_{\mathrm{eff}} = \sum_i \frac{\partial E}{\partial \langle A_i \rangle_0} A_i, \tag{2.147}$$

$$E_{\mathrm{eff}} = \langle H_{\mathrm{eff}} \rangle_0 \tag{2.148}$$

$|\Psi_0\rangle$ is an eigenstate of H_{eff}. However, the eigenvalue equation is still nonlinear due to the partial derivative on the right-hand side, and must be solved self-consistently. Only when E is a linear function of the $\langle A_i \rangle_0$ (the usual case in quantum mechanics) is the eigenvalue equation also linear.

In our case, finding the effective Hamiltonian is easy. It mostly corresponds to the term in angle brackets on the right-hand side of (2.142), but with a correction to the local (momentum-independent) term. Using

$$\frac{\partial \rho_{\mathrm{BF}}}{\partial \langle b^\dagger_{\mathbf{k}\sigma} b_{\mathbf{k}\sigma}\rangle_0} = \frac{\partial \rho_{\mathrm{BF}}}{\partial \langle a^\dagger_{\mathbf{k}\sigma} a_{\mathbf{k}\sigma}\rangle_0} = 1, \tag{2.149}$$

the result is[16]

$$H_{\mathrm{eff}} = \sum_{\mathbf{k}\sigma} v^\dagger_{\mathbf{k}\sigma} \left[-\epsilon_{\mathrm{eff}} \tau_z + \frac{Z\epsilon_{\mathbf{k}}}{2} (\tau_0 - \sigma\tau_x) \right] v_{\mathbf{k}\sigma}, \tag{2.150}$$

$$\epsilon_{\mathrm{eff}} = \frac{3}{4} J + Z' D f, \tag{2.151}$$

$$Z' = \frac{\mathrm{d}Z}{\mathrm{d}\rho_{\mathrm{BF}}}, \tag{2.152}$$

$$f = \frac{\langle H_t \rangle}{NZD}. \tag{2.153}$$

$Z'Df$ (the normalization has been chosen to make f dimensionless) can be seen as a renormalization of the creation energy due to the blocking effect bond fermions have on each other. An occupied site can no longer participate in hopping or creation processes, so that an energy $\sim \langle H_t \rangle / N$ is lost. Alternatively, one can view this as an effective (positive) correction to J; however, the variational energy should still be calculated with (2.142) which does not contain $Z'Df$. Note that a blocking term also arises in the (perhaps more familiar) Gutzwiller calculation for the Hubbard model, where it is usually unimportant: because the electron number is conserved, the blocking only results in a renormalization of the Fermi energy. In our case, bond fermions are generated by spontaneous pair production, and the blocking term is physically important because it inhibits this production.

The 2×2 Hamiltonian matrices in (2.150) can be diagonalized and give an effective $\mathbf{k}$-dependent band structure with a positive-energy and a negative-energy band, see Fig. 2.7. The eigenvalues and eigenvectors are

$$E^\pm_{\mathbf{k}\sigma} = \frac{Z\epsilon_{\mathbf{k}}}{2} \pm \sqrt{e^2_{\mathrm{eff}} + \frac{Z^2 \epsilon^2_{\mathbf{k}}}{4}}, \tag{2.154}$$

$$\psi^\pm_{\mathbf{k}\sigma} = \begin{pmatrix} \mp\sigma \alpha^\mp_{\mathbf{k}} \\ \alpha^\pm_{\mathbf{k}} \end{pmatrix}, \tag{2.155}$$

$$\left[\alpha^\pm_{\mathbf{k}}\right]^2 = 1 \pm \frac{\epsilon_{\mathrm{eff}}}{\sqrt{4\epsilon_{\mathrm{eff}} + Z^2 \epsilon^2_{\mathbf{k}}}}. \tag{2.156}$$

The particles are Bogoliubov fermions formed as mixtures of a-holes and b-particles. It follows from (2.24) that the density of Bogoliubov particles corresponds to the total density of electrons $n_e = 1 + n_c$, so that for half-filling ($n_c = 1$) the negative-energy bands

[16] It should be appreciated that the simple form of (2.150) was derived *assuming* $|\Psi_0\rangle$ does not break any symmetries. For an unrestricted $|\Psi_0\rangle$, $\sqrt{Z}$ would be much more complicated and so would H_{eff}. The reasoning is self-consistent, in the sense that we assume $|\Psi_0\rangle$ to be symmetric, thus H_{eff} turns out to be symmetric, thus it has a symmetric $|\Psi_0\rangle$ as its ground state (which closes the circle).

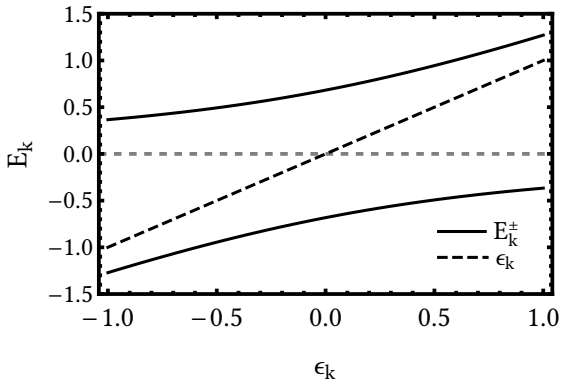

Figure 2.7: Quasiparticle bands $E^{\pm}_{\mathbf{k}\sigma}$ for $\epsilon_{\text{eff}} = 0.7D$ and $Z = 0.9$, with the free band energy $\epsilon_{\mathbf{k}}$ for comparison. Energies are given in units of D.

are occupied. The bond fermions form a condensate: for example, removing a negative-energy Bogoliubov particle with momentum $\mathbf{k}$ corresponds to removing $(\alpha^-_{\mathbf{k}})^2$ b-fermions from the condensate, and adding $(\alpha^+_{\mathbf{k}})^2$ a-fermions. Since $(\alpha^+_{\mathbf{k}})^2 \geq 1/2$, the lower band is "more a than b", which is why we refer to it as an *a-band* (and the upper band as a *b-band*).

The form of (2.154) shows the (possibly suprising) similarity of the strongly interacting Kondo lattice to the noninteracting periodic Anderson model (see Sec. 1.2.3), as the effective single-particle energies can be related by renormalizing the kinetic energy by Z and replacing the Anderson hybridization V with ϵ_{eff}.

The rest of the calculation can be simplified by introducing the dimensionless variable $r = \epsilon_{\text{eff}}/ZD$. It corresponds to the ratio between the energy needed to create a bond fermion, and the average hopping energy of each bond fermion. Intuitively, bond fermion production is strongly suppressed for $r \gg 1$. We can explicitly calculate

$$\rho_{\text{BF}}(r) = \frac{4}{N}\sum_{\mathbf{k}}\langle b^\dagger_{\mathbf{k}\sigma} b_{\mathbf{k}\sigma}\rangle_0 = \frac{4}{N}\sum_{\mathbf{k}}(\alpha^-_{\mathbf{k}})^2 = \frac{4}{N}\sum_{\mathbf{k}}\left[\frac{1}{2} - \frac{Dr}{4D^2r^2 + \epsilon^2_{\mathbf{k}}}\right] \tag{2.157}$$

$$= 2 - 2r\ln\left(\frac{1 + 2r^2 + \sqrt{1+4r^2}}{2r^2}\right), \tag{2.158}$$

$$f(r) = \frac{2}{ND}\sum_{\mathbf{k}}\frac{\epsilon_{\mathbf{k}}}{2}\left[\psi^-_{\mathbf{k}\uparrow}\right]^{\intercal}(\tau_0 - \sigma\tau_x)\psi^-_{\mathbf{k}\uparrow} = \frac{1}{ND}\sum_{\mathbf{k}}\epsilon_{\mathbf{k}}\left(1 - \frac{\epsilon_{\mathbf{k}}}{4D^2r^2 + \epsilon^2_{\mathbf{k}}}\right) \tag{2.159}$$

$$= -\frac{1}{2}\sqrt{1+4r^2} + 2r^2\,\text{arcoth}(\sqrt{1+4r^2}). \tag{2.160}$$

The flat density of states allows for an analytic evaluation of the momentum sums. From the definition of r and ϵ_{eff} we find the self-consistency equation

$$\frac{J}{D} = \frac{4}{3}\left(Zr - Z'f\right), \tag{2.161}$$

which can be solved for r (and thus all other parameters) using a numerical root-finding algorithm.

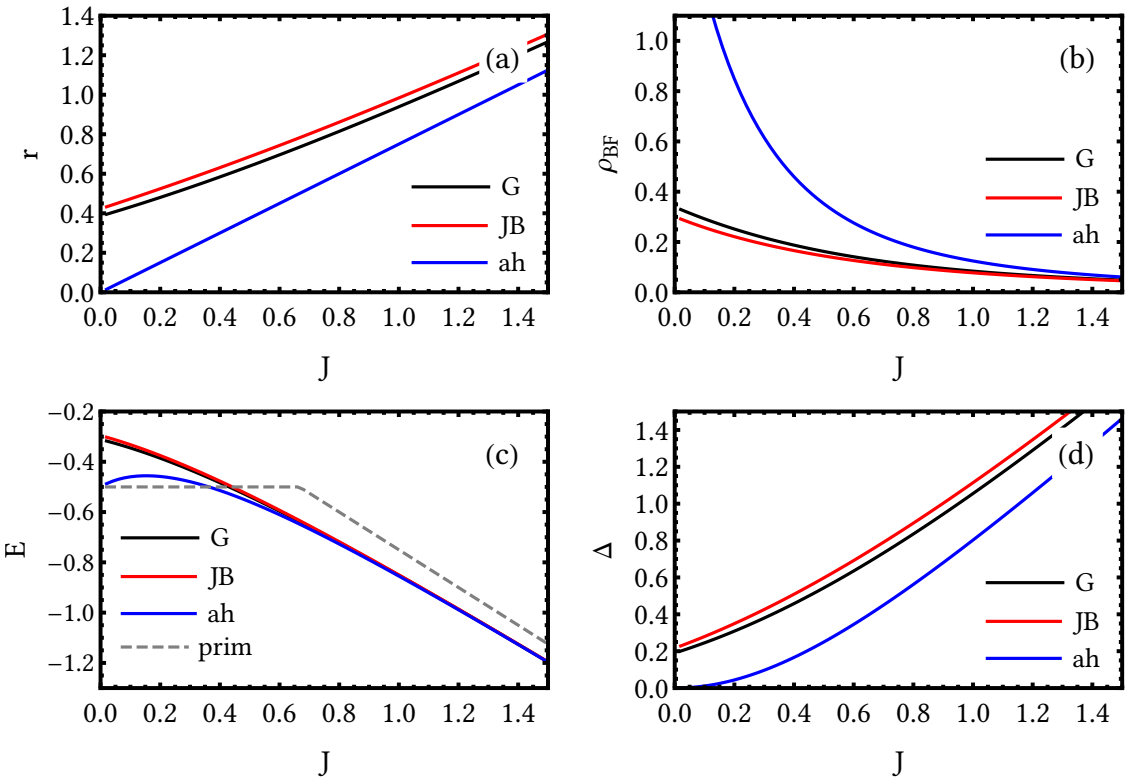

Figure 2.8: System parameters for the three different solution strategies. (a) dimensionless ratio r (b) bond fermion density ρ_{BF} (c) ground state energy density $E = \langle H \rangle / N$ (d) band gap Δ.

The above analysis can also be applied to the other two strategies of dealing with the hard-core constraint, which correspond to different choices of Z. We use subscripts G (Gutzwiller), JB (Jurecka-Brenig), and ah ("ad-hoc") to differentiate between different methods; the Gutzwiller Z^{G} is as before, while $Z^{\mathrm{JB}} = 1 - \rho_{\mathrm{BF}}$, and $Z^{\mathrm{ah}} = 1$.

The results for r are shown in Fig. 2.8 (a). The "ad-hoc" r^{ah} is directly proportional to J, as (2.161) reduces to $J/D = 3/4\, r^{\mathrm{ah}}$, whereas for the other two methods r never vanishes. The reason for this is that r characterizes the *total* creation energy of a bond fermion, which includes both the Kondo as well as the hard-core interaction energy; as the "ad-hoc" method ignores the hard-core interaction, the second term vanishes. The consequences of this can be seen in Fig. 2.8 (b). For small J, it is energetically favorable to generate a large number of bond fermions, since there is no term enforcing $\rho_{\mathrm{BF}}^{\mathrm{ah}} < 1$. The Gutzwiller and Jurecka-Brenig calculations are more correct, as the bond fermion density is limited to around 0.3 even for $J = 0$.

The ground-state energy density can be calculated as

$$\frac{\langle H \rangle}{N} = -\frac{3}{4} J (1 - \rho_{\mathrm{BF}}) + ZDf \tag{2.162}$$

and is shown in Fig. 2.8 (c). The light dashed line primitively estimates the ground-state energy as $E^{\mathrm{prim}} = \min(-D/2, -3/4J)$: $-D/2$ is the kinetic energy for uncorrelated elec-

trons ($J = 0$), and $-3/4J$ is the energy of the fully localized singlet state. The true ground-state energy will interpolate between these limits.

This plot demonstrates both strengths and weaknesses of the bond fermion method. For moderate-to-large J all three strategies give essentially the same result (and are significantly better than the primitive approximation), as this is the limit we have constructed the bond fermions from. Deficiencies appear at small J. At first glance, E^{ah} might be regarded as the most successful version, as it predicts the lowest energy and correctly reproduces the $J = 0$ limit (with $r^{\mathrm{ah}} = 0$ and $Z^{\mathrm{ah}} = 1$). However, this region is also where $\rho_{\mathrm{BF}}^{\mathrm{ah}}$ is unphysical, and the difference between E^{ah} and the less crude approximations quickly diminishes when increasing J. Furthermore, E^{ah} is nonmonotonic as the Kondo energy term in (2.162) is positive for $\rho_{\mathrm{BF}}^{\mathrm{ah}} > 1$, which is obviously also unphysical.

E^{G} and E^{JB} do not suffer from these specific problems, but they do not recover the correct ground state for $J = 0$ ($E^{\mathrm{G}} \approx E^{\mathrm{JB}} \approx -0.3D$). As we have mentioned before, in the actual free electron system all local states are equally likely, and not just the five states we have retained in the bond fermion calculation. Due to this restriction, the kinetic energy must then be (significantly) underestimated. Note however that we always have $E^{\mathrm{G}} < E^{\mathrm{JB}}$: as discussed, the Jurecka-Brenig method includes a self-interaction, so that it suffers even more badly than the Gutzwiller calculation in this limit.

Let us now take a closer look at the quasiparticle band structure of the system. We identify this with that of the effective Hamiltonian (Fig. 2.7). This is usual practice [115], but some care must be taken. The Gutzwiller bond fermion method is a ground-state theory and is in principle limited to static quantities. If we generate an additional a-b-pair for example, this influences the Gutzwiller parameters (reducing the kinetic energy) and causes all other quasiparticles to rearrange themselves. The band structure of the effective Hamiltonian includes the reduction in kinetic energy through the $Z'Df$-term, but not the rearrangement (the other quasiparticles are effectively assumed to be static). The identification is thus only approximate, but should be sufficiently accurate for most purposes. Note that the same caveat applies also to other theories that optimize a variational state using an effective Hamiltonian, such as mean-field theory [61].

As we mentioned, the band structure is formally the same as that of the periodic Anderson model with $U = 0$. Since the lower quasiparticle band is fully occupied, the bond fermion method leads us to conclude that the system is a *Kondo insulator*: this can be interpreted as an extreme version of the "large" Fermi surface, as we have $n_c = 1$ and thus $n_e = 2$ total electrons. The gap is indirect with the maximum of the lower band (minimum of the upper band) at $\epsilon_{\mathbf{k}} = +D$ ($\epsilon_{\mathbf{k}} = -D$). The size of the gap (Fig. 2.8 (d)) increases with J, as an increasing amount of energy is needed to generate bond fermions. For $J \gg D$ (not shown) we get $\Delta \longrightarrow 3/2J$ in all three cases, corresponding to the ground-state energy of two singlets. Again, only the "ad-hoc" method gives the correct limiting value at $J = 0$ (where the system should be conducting). In the other two cases we get a gap of around $\Delta \approx 0.2D$. This is of similar magnitude to the total energy per site $\langle H \rangle / N$ (which is just the kinetic energy for $J = 0$), which makes sense since this is approximately the energy lost when blocking a site with a bond fermion.

In summary, all three methods seem to give a satisfactory description of the Kondo lattice for $J > D$. The system is a Kondo insulator as expected, and the ground-state

energy clearly shows the trend towards localized singlets. For $J < D$, the "ad-hoc" method behaves quite differently from the others: It gives the correct noninteracting limit, but at the cost of several physically nonsensical predictions. Meanwhile, the more sophisticated methods underestimate the kinetic energy because of the hard-core interaction.

This however need not be too discouraging. Magnetic phase transitions are generally found at intermediate J (our calculations will support this), where the performance of the bond fermion methods appears acceptable. Furthermore, even in parameter regions where numerical accuracy may be lacking, results may still be qualitatively correct.

2.7 Gutzwiller approximation for general calculations and summary of expressions

To perform a bond fermion Gutzwiller calculation in more general settings (featuring magnetic order, for example), the procedure is somewhat more complicated. We will present a mostly straighforward approach here that does not directly rely on the symmetries (translation invariance, paramagnetism, particle-hole symmetry) used in the previous section; instead, possible symmetries can later be used to simplify the final expressions derived here. This method presented here is used in Chapters 3 and 4; Chapter 5 uses the "ad-hoc" method which is simpler to implement.

2.7.1 Equations

The general recipe is still the same as before: We write an effective Hamiltonian H_{eff} to optimize the wave function $|\Psi_0\rangle$, but terms have to be added to explicitly enforce the constraints that were before fulfilled automatically. First of all we have the Gutzwiller constraint (2.88), that is $0 = \langle a_{\mathbf{R}\sigma} b_{\mathbf{R}\tilde{\sigma}} \rangle_0$. This condition is taken care of by a set of Lagrange multipliers $\Lambda_{\mathbf{R}\sigma\tilde{\sigma}}$, which we add to H_{eff} as part of the operator H_Λ:

$$H_\Lambda = -\sum_{\mathbf{R}\sigma\tilde{\sigma}} \left[\Lambda_{\mathbf{R}\sigma\tilde{\sigma}} a_{\mathbf{R}\sigma} b_{\mathbf{R}\tilde{\sigma}} + \text{h.c.}\right] \tag{2.163}$$

$$= -\sum_{\mathbf{R}} v_{\mathbf{R}}^\dagger \Lambda_{\mathbf{R}} v_{\mathbf{R}}, \tag{2.164}$$

$$\Lambda_{\mathbf{R}} = \begin{pmatrix} 0 & 0 & \Lambda_{\mathbf{R}\uparrow\uparrow} & \Lambda_{\mathbf{R}\uparrow\downarrow} \\ 0 & 0 & \Lambda_{\mathbf{R}\downarrow\uparrow} & \Lambda_{\mathbf{R}\downarrow\downarrow} \\ \Lambda^*_{\mathbf{R}\uparrow\uparrow} & \Lambda^*_{\mathbf{R}\downarrow\uparrow} & 0 & 0 \\ \Lambda^*_{\mathbf{R}\uparrow\downarrow} & \Lambda^*_{\mathbf{R}\downarrow\downarrow} & 0 & 0 \end{pmatrix}. \tag{2.165}$$

The $\Lambda_{\mathbf{R}\sigma\tilde{\sigma}}$ are as yet undetermined, and will need to be solved for to enforce (2.88).

Next up is the conduction electron number, for which we introduce another Lagrange multiplier μ (the bond fermion chemical potential). The term added to the Hamiltonian is, taking the electron density from (2.24),

$$H_\mu = -\mu N_c = -\mu \sum_{\mathbf{R}} \left[1 - a_{\mathbf{R}}^\dagger a_{\mathbf{R}} + b_{\mathbf{R}}^\dagger b_{\mathbf{R}}\right] = -\mu \sum_{\mathbf{R}} v_{\mathbf{R}}^\dagger v_{\mathbf{R}} + \text{const.} \tag{2.166}$$

μ also needs to be solved for: For a given conduction electron density n_c, we want $Nn_c = \langle N_c \rangle_0$. The constant term (equal to μN) can be safely dropped from (2.166), as we do not care about the effective energy. The only utility of H_{eff} is that $|\Psi_0\rangle$ is its ground state, so a constant offset (even if it depends on the as yet undetermined parameter μ) is irrelevant.

Now that the constraints are taken care of, we again need to calculate derivatives of $\langle H \rangle$. This remains simple for the local energy terms H_J and $H_{\mathbf{B}}$, as these terms are linear in the bond fermion expectation values. For the kinetic energy H_t, we have to take into account the nontrivial matrix structure of $\sqrt{Z}_{\mathbf{R}}$. Specifically, the kinetic energy contribution to the effective Hamiltonian is

$$H_{\text{eff},t} = \sum_{\mathbf{R}\mathbf{R}'\alpha\alpha'} \frac{\partial \langle H_t \rangle}{\partial \langle v^\dagger_{\mathbf{R}\alpha} v_{\mathbf{R}'\alpha'} \rangle_0} v^\dagger_{\mathbf{R}\alpha} v_{\mathbf{R}'\alpha'} \tag{2.167}$$

$$= -\sum_{\mathbf{R}\mathbf{R}'} t_{\mathbf{R}\mathbf{R}'} v^\dagger_{\mathbf{R}} \overline{\sqrt{Z}}^\dagger_{\mathbf{R}} W^\dagger_{\mathbf{R}} W_{\mathbf{R}'} \overline{\sqrt{Z}}_{\mathbf{R}'} v_{\mathbf{R}'} - \sum_{\mathbf{R}} v^\dagger_{\mathbf{R}} m_{\mathbf{R}} v_{\mathbf{R}} + \text{irrelevant} \tag{2.168}$$

Here we inserted (2.113) for $\langle H_t \rangle$. The contribution (2.168) can again be separated into two terms, one of which is the kinetic energy itself, and the other the blocking effect (the "irrelevant" terms will be explained momentarily). The blocking term $m_{\mathbf{R}}$ has a nontrivial matrix structure, which reflects that the "blocking strength" can depend on both species (a or b) and the spin of a specific fermion. Specifically, $m_{\mathbf{R}}$ takes the form

$$m_{\mathbf{R}} = \begin{pmatrix} -m_{\mathbf{R}a} & 0 \\ 0 & m_{\mathbf{R}b} \end{pmatrix}, \tag{2.169}$$

$$[m_{\mathbf{R}a}]_{\sigma\tilde{\sigma}} = \sum_{\mathbf{R}'} \left\langle t_{\mathbf{R}\mathbf{R}'} v^\dagger_{\mathbf{R}} \frac{\partial \overline{\sqrt{Z}}^\dagger_{\mathbf{R}}}{\partial \langle a^\dagger_{\mathbf{R}\sigma} a_{\mathbf{R}\tilde{\sigma}} \rangle_0} W^\dagger_{\mathbf{R}} W_{\mathbf{R}'} \overline{\sqrt{Z}}_{\mathbf{R}'} v_{\mathbf{R}'} \right\rangle + \sum_{\mathbf{R}'} \left\langle t_{\mathbf{R}'\mathbf{R}} v^\dagger_{\mathbf{R}'} \overline{\sqrt{Z}}^\dagger_{\mathbf{R}'} W^\dagger_{\mathbf{R}'} W_{\mathbf{R}} \frac{\partial \overline{\sqrt{Z}}_{\mathbf{R}}}{\partial \langle a^\dagger_{\mathbf{R}\sigma} a_{\mathbf{R}\tilde{\sigma}} \rangle_0} v_{\mathbf{R}} \right\rangle, \tag{2.170}$$

and analogous for $m_{\mathbf{R}b}$. The easiest way to calculate the derivatives of $\overline{\sqrt{Z}}_{\mathbf{R}}$ is numerically: In Sec. 2.4, we introduced $\overline{\sqrt{Z}}_{\mathbf{R}}$ by first diagonalizing the density matrix $\rho_{\mathbf{R}}$ (whose entries are the $\langle a^\dagger_{\mathbf{R}\sigma} a_{\mathbf{R}\tilde{\sigma}} \rangle_0$ etc.). In the eigenbasis of $\rho_{\mathbf{R}}$, the calculation of the renormalization (the coefficients $\sqrt{\zeta}_{\mathbf{R}i}$) was straightforward, and $\sqrt{Z}_{\mathbf{R}}$ (and $\overline{\sqrt{Z}}_{\mathbf{R}}$) results after undoing the unitary transformation. For our implementation we simply perform these steps multiple times with slight offsets in the components of $\rho_{\mathbf{R}}$.[17]

In theory, one should also take into account anomalous contributions, i.e. nonzero entries in the off-diagonal blocks of $m_{\mathbf{R}}$, as (2.167) contains derivatives with respect to the "forbidden" terms $\langle a_{\mathbf{R}\sigma} b_{\mathbf{R}\tilde{\sigma}} \rangle_0$. These derivatives actually form the "irrelevant" terms: Their contribution to the effective Hamiltonian will be proportional to $a_{\mathbf{R}\sigma} b_{\mathbf{R}\tilde{\sigma}}$ (and its conjugate), which means that we can get rid of them by simply redefining our Lagrange multipliers $\Lambda_{\mathbf{R}\sigma\tilde{\sigma}}$.

[17] Due to the block structure of $\rho_{\mathbf{R}}$ an analytic calculation of the derivatives is possible, but the (complicated) result is not any more useful than a numerical derivative.

To get the final H_{eff}, we gather the constituent terms and add the local terms, which gives

$$H_{\text{eff}} = \sum_{\mathbf{R}} v_{\mathbf{R}}^\dagger h_{\mathbf{R}} v_{\mathbf{R}} + \sum_{\mathbf{R}\mathbf{R}'} v_{\mathbf{R}}^\dagger K_{\mathbf{R}\mathbf{R}'} v_{\mathbf{R}'}, \tag{2.171}$$

$$h_{\mathbf{R}} = h_{\mathbf{R}}^0 - m_{\mathbf{R}} - \Lambda_{\mathbf{R}} - \mu, \tag{2.172}$$

$$h_{\mathbf{R}}^0 = e_{\mathbf{R}} \mathrm{diag}(-1,-1,1,1) - \frac{\mathbf{B}}{2}\begin{pmatrix} -\boldsymbol{\tau} & 0 \\ 0 & \boldsymbol{\tau} \end{pmatrix}, \tag{2.173}$$

$$K_{\mathbf{R}\mathbf{R}'} = -t_{\mathbf{R}\mathbf{R}'} \sqrt{\overline{Z}}_{\mathbf{R}} W_{\mathbf{R}} W_{\mathbf{R}'} \sqrt{\overline{Z}}_{\mathbf{R}'}. \tag{2.174}$$

The ground state of H_{eff} is $|\Psi_0\rangle$. As a reminder, this is a *nonlinear* eigenvalue equation, as $\sqrt{\overline{Z}}_{\mathbf{R}}$ and $m_{\mathbf{R}}$ itself depend on $|\Psi_0\rangle$. Alternatively, we can see this as a *linear* eigenvalue equation, but augmented by a complicated set of equations for the parameters $\sqrt{\overline{Z}}_{\mathbf{R}}$ and $m_{\mathbf{R}}$ (this view is more useful for actual calculations).

The Lagrange multipliers $\Lambda_{\mathbf{R}\sigma\tilde{\sigma}}$ and μ need to be adjusted so that

$$0 = \langle a_{\mathbf{R}\sigma} b_{\mathbf{R}\tilde{\sigma}} \rangle_0 = \langle a_{\mathbf{R}\sigma}^\dagger b_{\mathbf{R}\tilde{\sigma}}^\dagger \rangle_0, \tag{2.175}$$

$$n_c N = \langle N_c \rangle_0, \tag{2.176}$$

which can also be seen as a nonlinear system of equations (note that the number of equations matches the number of unknowns). Using these definitions, the expectation value of the Gutzwiller energy is

$$\langle H \rangle = \sum_{\mathbf{R}} \langle v_{\mathbf{R}}^\dagger h_{\mathbf{R}}^0 v_{\mathbf{R}} \rangle_0 + \sum_{\mathbf{R}\mathbf{R}'} \langle v_{\mathbf{R}}^\dagger K_{\mathbf{R}\mathbf{R}'} v_{\mathbf{R}'} \rangle_0 + \sum_{\mathbf{R}} e_{\mathbf{R}}. \tag{2.177}$$

For future reference, we will also recapitulate the other definitions used here; if there is any confusion, the reader should reference the original sections:

$$v_{\mathbf{R}} = \begin{pmatrix} a_{\mathbf{R}\uparrow}^\dagger & a_{\mathbf{R}\downarrow}^\dagger & b_{\mathbf{R}\uparrow} & b_{\mathbf{R}\downarrow} \end{pmatrix}^{\mathsf{T}}, \tag{2.178}$$

$$W_{\mathbf{R}} = \frac{1}{\sqrt{2}} \begin{pmatrix} [s_{\mathbf{R}}^* + \mathbf{t}_{\mathbf{R}}^* \boldsymbol{\tau}]\, i\tau_y & [-s_{\mathbf{R}} + \mathbf{t}_{\mathbf{R}} \boldsymbol{\tau}] \end{pmatrix}, \tag{2.179}$$

$$e_{\mathbf{R}} = \frac{3J}{4} s_{\mathbf{R}}^2 - \frac{J}{4} \mathbf{t}_{\mathbf{R}}^2 - i\mathbf{B}(\mathbf{t}_{\mathbf{R}}^* \times \mathbf{t}_{\mathbf{R}}), \tag{2.180}$$

$$\rho_{\mathbf{R}} = \begin{pmatrix} \langle a_{\mathbf{R}\uparrow}^\dagger a_{\mathbf{R}\uparrow} \rangle_0 & \langle a_{\mathbf{R}\uparrow}^\dagger a_{\mathbf{R}\downarrow} \rangle_0 & & 0 \\ \langle a_{\mathbf{R}\downarrow}^\dagger a_{\mathbf{R}\uparrow} \rangle_0 & \langle a_{\mathbf{R}\downarrow}^\dagger a_{\mathbf{R}\downarrow} \rangle_0 & & \\ & 0 & & a \to b \end{pmatrix}, \tag{2.181}$$

$$\operatorname{diag}\{\langle N_{\mathbf{R}i}\rangle_0\} = U_{\mathbf{R}}^{\dagger}\rho_{\mathbf{R}}U_{\mathbf{R}}, \tag{2.182}$$

$$\sqrt{\zeta}_{\mathbf{R}i} = \sqrt{\frac{1-\sum_j\langle N_{\mathbf{R}j}\rangle_0}{1-\langle N_{\mathbf{R}i}\rangle_0}}, \tag{2.183}$$

$$\sqrt{Z}_{\mathbf{R}} = U_{\mathbf{R}}\sqrt{\zeta}_{\mathbf{R}}U_{\mathbf{R}}^{\dagger} = \begin{pmatrix}\sqrt{Z}_{\mathbf{R}a} & 0\\ 0 & \sqrt{Z}_{\mathbf{R}b}\end{pmatrix}, \tag{2.184}$$

$$\sqrt{\overline{Z}}_{\mathbf{R}} = \begin{pmatrix}\sqrt{Z}^{*}_{\mathbf{R}a} & 0\\ 0 & \sqrt{Z}_{\mathbf{R}b}\end{pmatrix}. \tag{2.185}$$

2.7.2 Optimization

We now describe how to actually use the above equations to optimize our variational state. First of all, one should choose a proper ansatz for the symmetry of the system. If one is interested in describing e.g. a translation invariant phase, the parameters in the equations will also be independent of $\mathbf{R}$. Thus, in the following, we take e.g. "s" to mean a suitable parametrization of $s_{\mathbf{R}}$, or "Λ" to mean a suitable parametrization of $\Lambda_{\mathbf{R}\sigma\tilde{\sigma}}$ (note that the parametrization should respect the self-adjointness and block structures of $\Lambda_{\mathbf{R}}$, $\sqrt{Z}_{\mathbf{R}}$, and $m_{\mathbf{R}}$).

To understand the numerical procedure, it helps to be somewhat explicit about which objects depend on which parameters. We take the effective Hamiltonian (2.171) to be a function of six types of parameters, $H_{\text{eff}}(s, \mathbf{t}, \sqrt{Z}, m, \Lambda, \mu)$, which is quadratic in fermion operators and can be diagonalized (e.g. in $\mathbf{k}$-space on a suitably fine grid, for translation invariant phases) to find the ground state $|\Psi_0\rangle\,(s, \mathbf{t}, \sqrt{Z}, m, \Lambda, \mu)$. All the parameters need to be solved for, which we will do "from inside to outside":

- If parameters s through m are fixed, we can solve for $\Lambda = \Lambda^*(s, \mathbf{t}, \sqrt{Z}, m)$ and $\mu = \mu^*(s, \mathbf{t}, \sqrt{Z}, m)$ by requiring (2.175–2.176) to hold for $|\Psi_0\rangle\,(s, \mathbf{t}, \sqrt{Z}, m, \Lambda^*, \mu^*)$. These conditions form a nonlinear system of equations, for which standard algorithms are available. Our implementation uses the freely available solver `MINPACK` [80] for the parameters in Λ (the single real parameter μ is determined by a one-dimensional solver at each `MINPACK` iteration).

- If parameters s and $\mathbf{t}$ are fixed, we solve for $\sqrt{Z} = \sqrt{Z}^*(s, \mathbf{t})$ and $m = m^*(s, \mathbf{t})$ through self-consistency iteration: We start with guesses for $\sqrt{Z}$ and m, and then calculate $|\Psi_0\rangle\,(s, \mathbf{t}, \sqrt{Z}, m, \Lambda^*, \mu^*)$, which gives us new guesses for $\sqrt{Z}$ and m through equations (2.169–2.170) and (2.181–2.184). If repeated, this procedure can sometimes by itself converge to a solution. Our implementation only performs a few steps of self-consistency iteration to get a rough starting guess, which is then refined by direct search with `MINPACK` solver.

- The above procedure gives $|\Psi_0\rangle\,(s, \mathbf{t}, \sqrt{Z}^*, m^*, \Lambda^*, \mu^*)$, from which we can calculate the Gutzwiller energy $\langle H\rangle(s, \mathbf{t})$ through equation (2.177). It remains to solve for s and $\mathbf{t}$ by minimizing $\langle H\rangle(s, \mathbf{t})$ through a (standard) optimization algorithm, our implementation uses `NLopt` [52, 97].

The solution thus proceeds in three nested loops. The main cost is that one has to repeatedly diagonalize H_{eff} in the innermost loop. All other operations consist of comparatively minor bookkeeping, as the number of free parameters to be solved for in each loop is typically small (< 20). Empirically, this solution method appears to work well with little oversight; for example, it is usually enough to take the simple $\Lambda_{\mathbf{R}\sigma\tilde{\sigma}'} = 0$ as a starting guess in the innermost loop, and still have the solver converge. The main danger is to miss some minima of $\langle H \rangle(s, \mathbf{t})$, which can be mitigated by either using a global optimization algorithm (over some physically reasonable range of parameters), or by repeated local optimizations from different starting points. To calculate momentum sums, we use a static grid and "smear out" the Fermi surface by using a small fictional temperature T (usually $T \sim 0.005t$ with t the nearest-neighbor hopping), which we found to be small enough for qualitative convergence), as this is the simplest way to avoid the numerical problems caused by the step discontinuity at the Fermi energy. We expect the numerical error introduced by this to be much smaller than the inherent inaccuracies in the bond fermion method.[18]

Of course, some variations on the above method are possible. For example, we chose $\sqrt{Z}_{\mathbf{R}}$ and $m_{\mathbf{R}}$ to solve the self-consistency equation, as was suggested by Yao et al. [115] in a similar calculation. Instead, one could try working with $\rho_{\mathbf{R}}$ directly; however, we found this to be much less numerically stable. Another variation is to exchange some operations in the innermost loops, like solving first for $\sqrt{Z}$ and m with fixed Λ. This also only slowed convergence. Loosely speaking, we think that future work would be better served by improving the method itself instead of its implementation.

[18] Note that the fictional temperature introduces a slight ambiguity: Should we now optimize the free energy $F = \langle H \rangle - TS$ instead of $\langle H \rangle$? While we have tried multiple methods and found no significant differences because of the smallness of T (indeed, if there *was* any difference the method could likely not be trusted), for peace of mind we have settled on $\langle H \rangle - TS/2$, which should lead to the best extrapolation of the energy to zero temperature [63].

3 Implementation for the square lattice

The square lattice is the "standard" setting to study the Kondo lattice model, as it is the simplest possible without the many peculiarities of one-dimensional systems; furthermore, many real materials have a strongly anisotropic layer structure, so that assuming a two-dimensional lattice is not entirely unrealistic (the experimental relevance of our results will be discussed later). This makes it a good test case for new techniques, since a number of more established methods have been applied to map out the phase diagram and band structure of the model. We will investigate these problems using the bond fermion method with the Gutzwiller approximation of Sec. 2.3. Our focus will be on magnetic transitions, which seem to occur in regions of moderate $J \sim t$, i.e. where the bond fermion method should be a good approximation. As the method is quite versatile (different types of magnetic order corresponding to different choices of $\mathbf{t}_\mathbf{R}$), we will go beyond usual Néel antiferromagnetism and also present results on incommensurate and ferromagnetic ordering. In the Néel case, we can compare the Gutzwiller approximation with the previous iterations of the bond fermion method.

Regarding previous work on this system, exact results are available in some special cases. At half-filling, the numerically exact quantum Monte Carlo results by Assaad [9] show that there is indeed a phase transition between a Néel antiferromagnetic phase at small interaction and a Kondo screened paramagnetic phase at large interaction. A variety of other numerical schemes that are less accurate but more generally applicable have been used. Most directly relevant for us are those investigating antiferromagnetic phase transitions, citing as examples the dynamical cluster approximation calculation by Martin and Assaad [76], the Gutzwiller approximation study by Lanatà et al. [68], and Watanabe and Ogata's variational Monte Carlo results [111]. Incommensurate phases were investigated through mean-field theory by Costa et al. [27] and Pankratova et al. [91]. Peters and Kawakami used dynamical mean-field theory to investigate both commensurate but nonstandard magnetic order [94] and more general spin- and charge-ordered phases [93].

3.1 Implementation

The geometry of the lattice enters into the Hamiltonian only through the hopping terms. Our focus is on the case of nearest-neighbor hopping (particle-hole symmetry), but we will also discuss the effects of a second-nearest-neighbor term. We thus set

$$H_t = -\sum_{\mathbf{R}\mathbf{R}'} t_{\mathbf{R}\mathbf{R}'} c^\dagger_{\mathbf{R}} c_{\mathbf{R}'}, \tag{3.1}$$

$$t_{\mathbf{R}\mathbf{R}'} = \begin{cases} t & \mathbf{R} \text{ and } \mathbf{R}' \text{ N. N.} \\ t' & \mathbf{R} \text{ and } \mathbf{R}' \text{ 2nd N.N.} \\ 0 & \text{else.} \end{cases} \tag{3.2}$$

t is used as the energy unit from here on. After a Fourier transform, the kinetic energy Hamiltonian yields the free band structure

$$H_t = \sum_{\mathbf{k}} c^\dagger_{\mathbf{k}} \epsilon_{\mathbf{k}} c_{\mathbf{k}}, \tag{3.3}$$

$$\epsilon_{\mathbf{k}} = -2t \left(\cos\left(k_x\right) + \cos\left(k_y\right)\right) - 4t' \cos\left(k_x\right) \cos\left(k_y\right). \tag{3.4}$$

In this chapter, we will set the magnetic field to zero ($\mathbf{B} = 0$). We take the bond fermion background $|\Omega\rangle$ to have an in-plane, spiral magnetic moment of the form

$$s_{\mathbf{R}} = s = \sqrt{1 - |\mathbf{t}|^2}, \tag{3.5}$$

$$\mathbf{t}_{\mathbf{R}} = |\mathbf{t}| \left(\cos(\mathbf{Q}\mathbf{R})\hat{e}_x + \sin(\mathbf{Q}\mathbf{R})\hat{e}_y\right). \tag{3.6}$$

$\mathbf{Q}$ is the magnetic wave vector. Néel antiferromagnetism has $\mathbf{Q} = (\pi, \pi)$, while pure ferromagnetic order has $\mathbf{Q} = (0, 0)$. s and $|\mathbf{t}|$ are constant, so that there is no modulation of the spin magnitude or of the charge density.

Our numerical implementation is as described in Sec. 2.7, and it is possible to insert this ansatz directly into the expressions therein. However, (3.6) is not translation invariant, which makes the implementation somewhat more tedious than it needs to be. This can be solved by taking advantage of a remaining symmetry: the system is unchanged when translating by $\mathbf{R}$ and simultaneously rotating all spins by $\varphi_{\mathbf{R}} = -\mathbf{Q}\mathbf{R}$ around the z-axis. Based on this, we can perform a canonical transformation of our electron operators that will result in a translation-invariant system. Effectively, we should perform a site-dependent rotation, so that in the rotated system the spins are all parallel (as opposed to the spiral form in (3.6). The most straightforward definition of the rotated operators c' and f' would be

$$c^\dagger_{\mathbf{R}\sigma} = e^{-i\varphi_{\mathbf{R}}\frac{\sigma}{2}} c'^\dagger_{\mathbf{R}\sigma} = e^{i\mathbf{Q}\mathbf{R}\frac{\sigma}{2}} c'^\dagger_{\mathbf{R}\sigma}, \tag{3.7}$$

and analogously for f. Actually, we will use an equivalent but slightly more convenient formulation: in addition to the spin rotation, we perform a further site-dependent gauge transformation, specifically

$$c^\dagger_{\mathbf{R}\uparrow} = c'^\dagger_{\mathbf{R}\uparrow}, \tag{3.8}$$
$$c^\dagger_{\mathbf{R}\downarrow} = e^{-i\mathbf{Q}\mathbf{R}} c'^\dagger_{\mathbf{R}\downarrow}, \tag{3.9}$$
$$f^\dagger_{\mathbf{R}\uparrow} = e^{i\mathbf{Q}\mathbf{R}} f'^\dagger_{\mathbf{R}\uparrow}, \tag{3.10}$$
$$f^\dagger_{\mathbf{R}\downarrow} = f'^\dagger_{\mathbf{R}\downarrow}. \tag{3.11}$$
$$\tag{3.12}$$

Note that for both c- and f-electrons, the relative phase between up and down is $\mathbf{QR}$, just like in (3.7). By replacing electron operators with these primed equivalents in (2.2–2.5) we get the new basis states

$$\left|S'\right\rangle_{\mathbf{R}} = \left|S\right\rangle_{\mathbf{R}}, \tag{3.13}$$
$$\left|T'_z\right\rangle_{\mathbf{R}} = \left|T_z\right\rangle_{\mathbf{R}}, \tag{3.14}$$
$$\left|T'_x\right\rangle_{\mathbf{R}} = \cos(\mathbf{QR}) \left|T_x\right\rangle_{\mathbf{R}} + \sin(\mathbf{QR}) \left|T_y\right\rangle_{\mathbf{R}}, \tag{3.15}$$
$$\left|T'_y\right\rangle_{\mathbf{R}} = \cos(\mathbf{QR}) \left|T_y\right\rangle_{\mathbf{R}} - \sin(\mathbf{QR}) \left|T_x\right\rangle_{\mathbf{R}}. \tag{3.16}$$

$\left|S\right\rangle_{\mathbf{R}}$ and $\left|T_z\right\rangle_{\mathbf{R}}$ are unchanged while $\left|T_x\right\rangle_{\mathbf{R}}$ and $\left|T_y\right\rangle_{\mathbf{R}}$ are rotated into each other, as to be expected from a spin-1 vector. $\left|A_\sigma\right\rangle_{\mathbf{R}}$ and $\left|B_\sigma\right\rangle_{\mathbf{R}}$ transform as spin-1/2 states (like $f^\dagger_{\mathbf{R}\sigma}$). Under this definition, (3.6) gives

$$\mathbf{t}_{\mathbf{R}} \left|\mathbf{T}\right\rangle_{\mathbf{R}} = \left|\mathbf{t}\right| \left|T'_x\right\rangle_{\mathbf{R}}. \tag{3.17}$$

We now set

$$s'_{\mathbf{R}} = s' = s, \tag{3.18}$$
$$\mathbf{t}'_{\mathbf{R}} = |\mathbf{t}|\hat{e}_x, \tag{3.19}$$

which lets us recover $\left|\Omega\right\rangle_{\mathbf{R}}$ as

$$\left|\Omega\right\rangle_{\mathbf{R}} = s'_{\mathbf{R}} \left|S'\right\rangle_{\mathbf{R}} + \mathbf{t}'_{\mathbf{R}} \left|\mathbf{T}'\right\rangle_{\mathbf{R}}. \tag{3.20}$$

This has the exact same form as (2.9). However, in the primed frame the magnetic moment is constant and parallel to $\hat{e}_x$.

We also have to express the kinetic terms and the interaction using the primed operators. The interaction H_J is isotropic, so its form is unchanged. Regarding the kinetic energy, we see from (3.8–3.9) that

$$c^\dagger_{\mathbf{k}\uparrow} = c'^\dagger_{\mathbf{k}\uparrow}, \tag{3.21}$$
$$c^\dagger_{\mathbf{k}\downarrow} = c'^\dagger_{\mathbf{k}-\mathbf{Q}\downarrow}, \tag{3.22}$$
$$H_t = \sum_{\mathbf{k}} c'^\dagger_{\mathbf{k}} \tilde{\epsilon}_{\mathbf{k}} c'_{\mathbf{k}}, \tag{3.23}$$
$$\tilde{\epsilon}_{\mathbf{k}} = \begin{pmatrix} \epsilon_{\mathbf{k}} & 0 \\ 0 & \epsilon_{\mathbf{k}+\mathbf{Q}} \end{pmatrix}. \tag{3.24}$$

$\tilde{\epsilon}_{\mathbf{k}}$ is the (spin-dependent) effective kinetic energy matrix, in which all dependence on $\mathbf{Q}$ is isolated. This is the main utility of the transformation, as the system is now effectively translation invariant again. This is in particular also true for $W_{\mathbf{R}}$ and $\sqrt{Z}_{\mathbf{R}}$, for example: otherwise, one would have to carry factors of $e^{i\mathbf{Q}\mathbf{R}}$ inside these matrices as well. The reason we chose the definition (3.8–3.11) over (3.7) is that this simplifies the kinetic energy; (3.7) would result in an annoying (and confusing) offset of $\mathbf{Q}/2$ in (3.24). It should be noted that the summation in (3.23) goes over the whole Brillouin zone: while for special values of $\mathbf{Q}$ (like $\mathbf{Q} = (\pi, \pi)$) one can introduce a smaller *magnetic Brillouin zone*, for general $\mathbf{Q}$ this is not possible.

From this point on, we will drop the primes. To solve the system, we have to insert our ansatz (3.19) and kinetic energy (3.24) into the expressions of section 2.7, and then simplify because of the symmetries present in our system. This leads to the effective Hamiltonian (after a Fourier transform) of

$$H_{\text{eff}} = \sum_{\mathbf{k}} v_{\mathbf{k}}^{\dagger} \left[h + K_{\mathbf{k}} \right] v_{\mathbf{k}}, \tag{3.25}$$

$$h = e \operatorname{diag}(-1, -1, 1, 1) - \Lambda - m - \mu, \tag{3.26}$$

$$e = \frac{3J}{4} s^2 - \frac{J}{4} |\mathbf{t}|^2, \tag{3.27}$$

$$K_{\mathbf{k}} = \sqrt{Z} W^{\intercal} \tilde{\epsilon}_{\mathbf{k}} W \sqrt{Z}. \tag{3.28}$$

Due to the effective translation invariance, we can drop the site index from e, W, Λ, and m. We also used that W is real (because $t_y = 0$), from which it is possible to derive that *all* quantities in the Hamiltonian are real. In particular, this means that W, $\sqrt{Z} = \sqrt{\overline{Z}}$, m, and Λ are all real (the block structure of these matrices is as in Sec. 2.7). The only complication encountered is that we earlier assumed the kinetic energy to be spin-independent, see (2.174). The expression (3.28) with $\tilde{\epsilon}_{\mathbf{k}}$ "sandwiched" can be derived from the (much earlier) bond fermion result (2.28), but is also quite intuitive: $\tilde{\epsilon}_{\mathbf{k}}$ is the kinetic energy for electrons, and the matrix W "translates" it into the bond fermion language (note the matching dimensions: $\tilde{\epsilon}_{\mathbf{k}}$ is 2×2 and W is 2×4).

While one could further reduce the number of independent parameters to be solved for by taking into account that the magnetization is entirely in-plane, we have not found this necessary since the method is computationally cheap enough anyway. By noting only that the matrices must be real and symmetric, we get that each of the 2×2 blocks in $\sqrt{Z}$ and m has three independent entries, and Λ has four.

Once a parametrization has been chosen, the numerical solution can proceed by the procedure specified in Sec. 2.7. The variational energy is minimized for fixed external parameters t', J, and n_c; the nested loops are

- Solve for Λ and μ, which fixes the electron number and the Gutzwiller constraint $\langle a_{\mathbf{R}\sigma} b_{\mathbf{R}\tilde{\sigma}} \rangle_0 = 0$.
- Solve for $\sqrt{Z}$ and m, the Gutzwiller renormalization parameters.
- Optimize $\langle H \rangle$ over $|\mathbf{t}|$ and $\mathbf{Q}$, which parametrize $s_{\mathbf{R}}$ and $\mathbf{t}_{\mathbf{R}}$. This determines the magnetic structure of the solution.

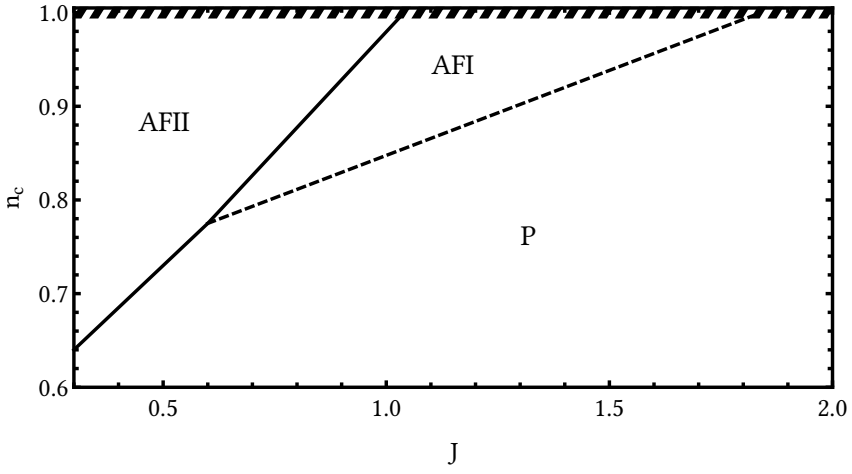

Figure 3.1: Phase diagram when taking only antiferromagnetism into account. The dashed line indicates that the AFI-P transition is continuous, while the full line implies that the AFII-P and AFII-AFI transitions are discontinuous. The size of the discontinuity decreases when approaching half-filling (more information the text). For $n_c = 1$ (stripes), the system is insulating and the AFII-AFI transition is also continuous.

Since there are competing phases in the model, we perform local optimizations with different starting values for $|\mathbf{t}|$ and $\mathbf{Q}$, corresponding to different magnetization strengths and ordering vectors.

3.2 Antiferromagnetic phase diagram

3.2.1 Phase diagram and band structure

We first focus on the case of pure antiferromagnetic ordering with only nearest-neighbor hopping, which corresponds to fixing $\mathbf{Q} = (\pi, \pi)$ and $t' = 0$. This is the most symmetric and most well-studied setting. While our method also allows us to perform calculations in the more general case, it is reassuring to first show that we can reproduce the main features of the model that have been established in previous investigations, with quantitative improvements over the previous bond fermion theory. Incommensurate and ferromagnetic ordering will be discussed in a later section.

When varying J and n_c, three different phases emerge (Fig. 3.1). At large J, formation of magnetic moments is suppressed by the interaction which favors singlets ($\mathbf{t} = 0$), giving the paramagnetic (P) phase. Two antiferromagnetic phases (we will refer to them as AFI and AFII) are found for moderate J: the symmetry of the magnetic ordering is the same in both cases, but away from half-filling ($n_c \neq 1$) there is a discontinuous drop in $|\mathbf{t}|$ across the transition from AFII to AFI (Fig. 3.2). The difference between the phases lies in their Fermi surfaces and band structures (Fig. 3.3); as in Sec. 2.6, we identify the

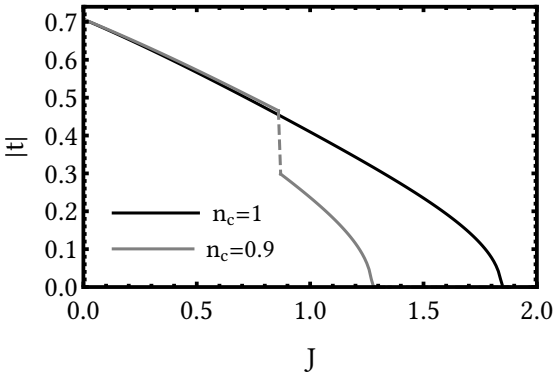

Figure 3.2: Magnetic parameter $|\mathbf{t}|$ across the AFII-AFI and AFI-P transitions. The transition to P (which has $|\mathbf{t}| = 0$) shows a square-root behavior. At half-filling, $|\mathbf{t}|$ is continuous (the critical point $J_{c,2} = 1.04t$ for the AFII-AFI transition is not distinct), while away from half-filling there is a jump in $|\mathbf{t}|$ (dashed).

band structure with the eigenvalues of the effective Hamiltonian[1]. Note that no error is committed when using this band structure to calculate the position of the Fermi surface. Unlike the excitation energies, the position of the Fermi surface *is* a ground state quantity, since it corresponds to points of discontinuity in $\langle c_{\mathbf{k}}^{\dagger} c_{\mathbf{k}} \rangle$.

The Bogoliubov nature of the quasiparticles should be kept in mind when interpreting the band structures. The negative-energy bands in Fig. 3.3 (b) are mostly of a-hole character, as the gap is quite large. Upon lowering n_c away from half-filling, the Fermi energy cuts into the a-hole band, which is equivalent to injecting a-particles. Thus, the Fermi surfaces in Fig. 3.3 (a) are formed by a-particles. Of course, physically all transport phenomena correspond to (renormalized) c-electron hopping.

A special feature of the Fermi surfaces is that they are "locked": $\mathbf{k}$ appears in the effective Hamiltonian solely through $\epsilon_{\mathbf{k}}$ and $\epsilon_{\mathbf{k}+\mathbf{Q}}$ in (3.23), which for $t' = 0$ satisfy $\epsilon_{\mathbf{k}+\mathbf{Q}} = -\epsilon_{\mathbf{k}}$, so there is only a single free parameter. The Fermi surfaces must thus be lines of constant $\epsilon_{\mathbf{k}}$. As the Fermi surfaces of a trivially solvable free-electron ($J = 0$) system follow these same lines (with $\epsilon_{\mathbf{k}} = E_{\text{Fermi}}$, the Fermi energy), the sheets of the interacting Fermi surface can be directly identified with those of a free-electron system. However, this associated non-interacting system does not necessarily need to have the same conduction electron density n_c as the interacting one; depending on this "effective" n_c, we can identify the Fermi surfaces as large or small (as in Sec. 1.2.3).

Specifically, the P and AFI phases have heavy hole pockets around (π, π) (and for AFI around the magnetically backfolded $(0, 0)$). These are large Fermi surfaces, as the Fermi surface is that of a noninteracting system filled with $n_c + 1$ itinerant electrons; it is as if the f-electrons (despite being localized) still contribute to the Fermi surface volume. Meanwhile, the AFII (small Fermi surface) phase has the same Fermi surface as a noninteracting system filled with n_c itinerant electrons, albeit with a larger band mass and and

[1] Our effective Hamiltonian actually gives the excitation spectrum in the rotated system. A c'-excitation with momentum $\mathbf{k}$ corresponds to a c-excitations with momenta $\mathbf{k}$ and $\mathbf{k} - \mathbf{Q}$. In plots with $|\mathbf{t}| = 0$ (for example, P in Fig. 3.3 (b)) we use the lab frame (i.e., $\mathbf{Q} = 0$) to avoid a redundant doubling of the bands.

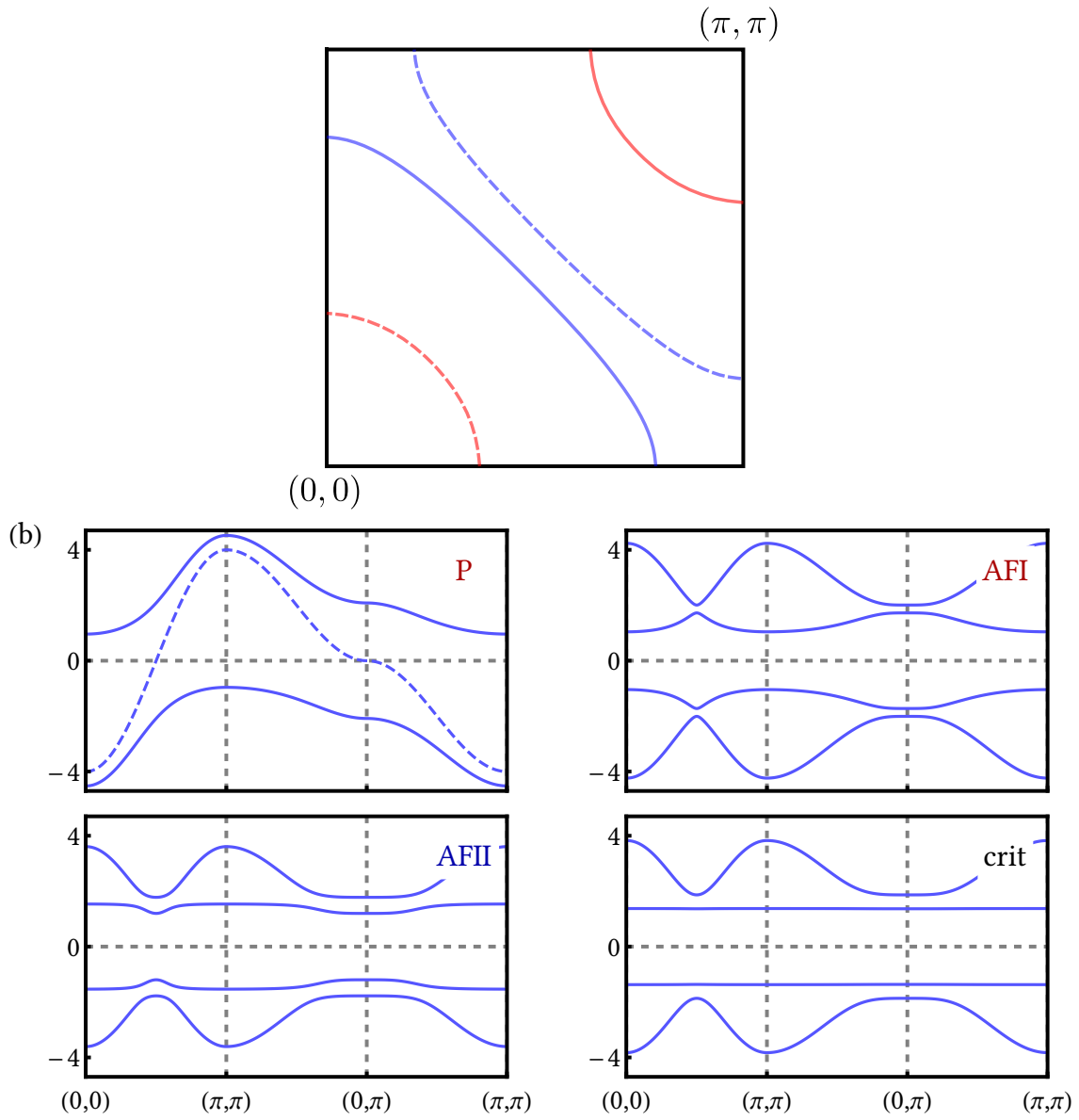

Figure 3.3: Evolution of the Fermi surfaces and band structures across the antiferromagnetic transition. Detailed interpretations and explanations are in the text.

(a) Possible Fermi surfaces for $n_c = 0.8$. Specifically, the Fermi surfaces for each phase are: P: red full line. AFI: both red lines. AFII: both blue lines. The full blue (full red) line is also the Fermi surface for a free electron system with $n_c = 0.8$ ($n_c = 1.8$) conduction electrons.

(b) Band structures for $n_c = 1$. From left to right and top to bottom, we have $J = 2t$ (P, the dashed line is the free band structure for comparison), $J = 1.6t$ (AFI), $J = 0.7t$ (AFII), and $J = 1.04t$ (critical point with a flat band, see the text).

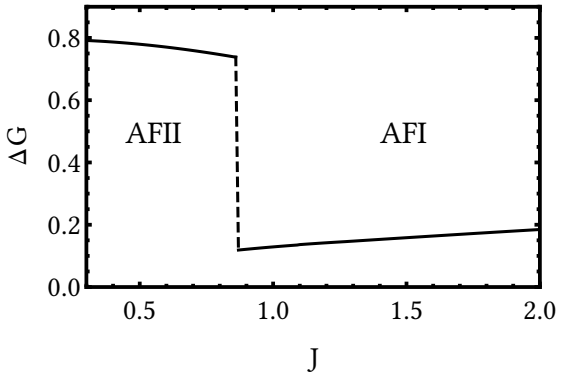

Figure 3.4: Quasiparticle residue ΔG across the AFII-AFI transition for $n_c = 0.9$, explanation in the text.

antiferromagnetically folded. This behavior of the bands is qualitatively very similar to the results of the dynamical cluster approximation [76]. While real-space DMFT predicts non-Néel ordered states, there is a very similar transition in Fermi surface topology there as well [93].

We must reiterate that this interpretation is superficial. While it is commonly suggested that the change in band structure is a consequence of the f-electrons "dropping out" or "localizing", this interpretation is not obvious in bond fermion theory, as we do not have a direct measure for the degree of "localization". However, there are other ways to judge the influence of correlations (and thus the f-electrons) on the quasiparticle properties. First is the larger band mass at the Fermi surface in the AFI phase, as this indicates an effective hybridization with the localized f-electrons. Further, the large Fermi surfaces phases also feature "heavy fermions" in the Fermi liquid sense. We can measure this by calculating the discontinuity in the conduction electron occupation $G(\mathbf{k})$ at the Fermi surface[2], which corresponds to the quasiparticle residue (usually called Z, but we will refer to it as ΔG to avoid confusion with the related Gutzwiller matrix) and is a measure for the mass enhancement due to correlations ($m^* \propto 1/\Delta G$). From Fig. 3.4, it is apparent that the AFII-AFI transition is accompanied by a stark change in the quasiparticle residue from almost free ($\Delta G \approx 0.8$) to strongly renormalized ($\Delta G \approx 0.1$). The large Fermi surface phases thus would be classified as much more correlated, indicating an increased influence of the f-electrons on the dynamics of the conduction electrons.

Approaching half-filling, all three phases develop band gaps (Fig. 3.5). As was discussed for pure paramagnetism in Sec. 2.6, a gap of order t remains even at $J = 0$. The addition of antiferromagnetism does not change this: on the contrary, the gap is larger than it would be for pure paramagnetism, since antiferromagnetism would lead to gap formation even by itself. Speaking more quantitatively, the exact ground state energy of the $J = 0$ system is $E_{\text{exact}} = -16/\pi^2 t = -1.62t$. Our result compares poorly with the variational energy

[2] $G(\mathbf{k})$ is defined as in Sec. 2.5.1, $G(\mathbf{k}) = \langle c_{\mathbf{k}}^\dagger c_{\mathbf{k}} \rangle$. For G', the $\mathbf{k}$-dependent part of G, we have $G'(\mathbf{k}) = \langle v_{\mathbf{k}}^\dagger \sqrt{Z} W^\intercal W v_{\mathbf{k}} \sqrt{Z} \rangle_0$ (compare this to the kinetic energy in (3.28)). ΔG, the size of the discontinuity at the Fermi surface, can be calculated with either $G(\mathbf{k})$ or $G'(\mathbf{k})$, as they only differ by a constant.

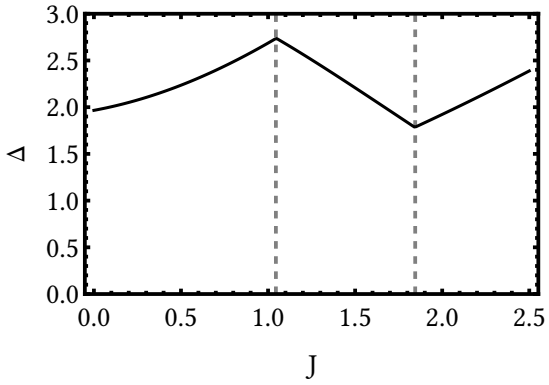

Figure 3.5: Band gap Δ at half-filling. The kinks correspond to the AFII-AFI and AFI-P phase transitions; for $J \gg t$ (not shown) we get $\Delta \to \frac{3}{2}J$.

$E_{\text{var}} = -1.08t$. Reiterating a previous point, predictions should be interpreted as having at best qualitative character in this parameter region.

Luckily, the region of antiferromagnetic phase transitions is found at moderate J, where our approximations are easier to justify. At half-filling, the critical value for the transition to magnetic order is $J_c = 1.85t$, which is a lot closer to the quantum Monte Carlo (QMC) value of $J_c = 1.45t \pm 0.05t$ [9] than the original bond fermion prediction (using the "ad-hoc" method for the constraint) of $J_c = 2.3t$ [33]. The QMC result is considered to be exact, in the sense that the bound $\pm 0.05t$ estimates all sources of error (for QMC, these are statistical fluctuations and the extrapolation to an infinite system). To compare, the variational Monte Carlo of Watanabe and Ogata gives a value of $J_c = 1.7t$ [111]. In our view, this value represents something of a "gold standard" for calculations that do not explicitly include long-range fluctuations (the wave function of Watanabe and Ogata consists of an uncorrelated state multiplied by a purely local projection operator). From this standpoint, the accuracy of the bond fermion prediction for J_c appears adequate. Dynamical mean-field theory gives $J_c = 2.2t$ [93], and the dynamical cluster approximation $J_c = 2.1t$ [77].

A mean-field description gives the critical value as $J_c = 0.4W = 3.2t$ ($W = 8t$ is the free bandwidth) [27]. The underlying reason for this significantly larger value is that the Kondo singlet is by nature correlated, i.e. it cannot be written as a Slater determinant. For example, for $J \gg t$, the correct expression for the energy per site is $-\frac{3}{4}J$, while the mean-field result is $-\frac{3}{8}J$. This means that mean-field theory is biased against Kondo screening (and in turn biased towards magnetic fluctuations). However, mean-field theory *does* reproduce the correct behavior for $J = 0$. It is thus accurate in the opposite limit as bond fermion theory, with a crossover in the ground state energy somewhere in between.

The bond fermion theory of Jurecka and Brenig [53] deserves special consideration, we will discuss it in Sec. 3.2.3; before this, we will discuss some interesting phenomena that appear for $n_c = 1$.

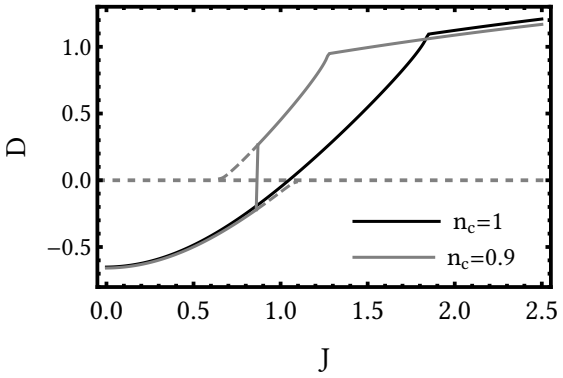

Figure 3.6: (Signed) width of the valence band $D = E_{\mathrm{v}}(0,0) - E_{\mathrm{v}}(\pi/2, \pi/2)$, where $E_{\mathrm{v}}(\mathbf{k})$ is the band energy of the second-lowest (valence) band. $|D|$ is the width of the band, and the sign determines the phase ($D > 0$ is AFI and $D < 0$ AFII). Note that $D = 0$ at the transition for $n_c = 1$; the density of states $\rho \sim 1/D$ thus diverges. For $n_c = 0.9$ the density of states does not diverge, but there are metastable states with very small $|D|$ (dashed). The kinks in the graphs at larger J correspond to the AFI-P transition.

3.2.2 Special features at half-filling

An interesting property of the phase diagram is that the AFII-AFI transition in a sense exists even at half-filling. There are no Fermi surfaces due to the gap, but the change in the band structure can still be detected. A "peak" in the valence band at the $\epsilon_{\mathbf{k}} = 0$ line (which contains $(\pi/2, \pi/2)$ for example) flips and turns into a "trough". Away from half-filling, this is accompanied by the aforementioned discontinuous change in Fermi surface (Lifshitz transition). While there is no Lifshitz transition at half-filling, the change in band structure still occurs. In this sense, half-filling is "smoothly connected" to the doped case, as on each side of the AFII-AFII transition the chemical potential simply wanders into the gap when approaching half-filling.

A further consequence of the gap is that the AFII-AFI transition itself is also smooth at half-filling: In the doped regime, there is a jump in $|\mathbf{t}|$ because of the Lifshitz transition. With a gap, the flipping of the band structure can happen continuously, without a jump in $|\mathbf{t}|$. Even more dramatically, at the critical point $J_{c,2} = 1.04t$ (when the maximum turns into a minimum), the whole band is perfectly flat (bottom right in Fig. 3.3 (b)). Intuitively, we can imagine moving an infinitesimal distance away from half-filling. On either side of the transition the Fermi surface is locked to either the red or the blue lines in Fig. 3.3 (a), so for a continuous phase transition the surface must be ill-defined at $J_{c,2}$. Exactly this happens for the flat band. A rigorous mathematical treatment is found below in Sec. 3.2.2.1.

This should not be confused with a complete decoupling of the c- and f-electrons (as appears for example in mean-field calculations at small J [27]). In our ansatz, localized and delocalized electrons have some degree of coupling no matter the phase, and the flat band arises at the critical point between two such phases.

It is to be emphasized that this leads to a divergent density of states and band mass at the transition point (note that ΔG remains finite and nonzero). While the square lattice is pathological in the sense that even in the free system the density of states diverges at zero energy, this is "only" logarithmic (a consequence of the saddle point of $\epsilon_{\mathbf{k}}$ for $\mathbf{k} = (0, \pi)$ and similar points), while in our case the two bands around the gap are each compressed into zero-width slivers. In fact, the symmetries that lead to the flat band (most significantly that $\epsilon_{\mathbf{k}} = -\epsilon_{\mathbf{k}+\mathbf{Q}}$) are also present in the nonpathological three-dimensional cubic lattice, so we expect a similar situation to occur there also.

At finite doping the band becomes narrower close to the transition, but a perfectly flat band is not realized. Instead, the density of states increases when approaching the transition from either side, but does not diverge (Fig. 3.6). Around the critical point there is a coexistence region with two separate local minima in the energy, corresponding to each of the antiferromagnetic phases. One of these minima is only metastable, and the transition is the point where their energies cross. As shown in the figure, the valence band becomes very narrow in both the metastable regions, but the transition occurs before a flat band is realized. We speculate that even at finite doping, inclusion of long-range fluctuations may move the phase transition closer towards these regions, as a large density would enhance them. As discussed in Sec. 3.4, some heavy fermion magnetic transitions show a significant (possibly divergent) mass enhancement near the phase transition; the "band flattening" mechanism we find may be a candidate to explain this phenomenon.

3.2.2.1 Mathematical details of the flat band

As mentioned before, we have $\epsilon_{\mathbf{k}+\mathbf{Q}} = -\epsilon_{\mathbf{k}}$ in (3.23). From (3.25) one gets the effective 4×4 band structure Hamiltonian

$$H_{\mathbf{k}} = h + \epsilon_{\mathbf{k}}\, \kappa, \tag{3.29}$$

$$\kappa = \sqrt{Z} W^{\mathsf{T}} \begin{pmatrix} 1 & 0 \\ 0 & -1 \end{pmatrix} W \sqrt{Z}. \tag{3.30}$$

The matrices h and κ are functions of the Gutzwiller parameters $\sqrt{Z}$ and m obtained from solving the self-consistency equations, and the value of $|\mathbf{t}|$ from the minimization. As such, they are implicitly functions of J. Note that they do not depend on $\mathbf{k}$, and the only momentum dependence is in $\epsilon_{\mathbf{k}}$.

The band energies are the eigenvalues of $H_{\mathbf{k}}$. At $J_{c,2} = 1.04t$, one finds that one pair of eigenvalues is constant, meaning independent of $\epsilon_{\mathbf{k}}$. However, an explicit numerical calculation shows that h and κ neither commute nor anticommute (in fact, $h\kappa \pm \kappa h$ both have full rank). From this one can infer that there is no $\mathbf{k}$-independent transformation to block-diagonalize $H_{\mathbf{k}}$. This illustrates why the flat band does not correspond to a physical symmetry: the symmetry operation involves both a translation in $\mathbf{k}$-space as well as a rotation in the abstract bond fermion space.

To give some mathematical insight into the circumstances required for the flat band, we calculate the eigenvalues E^* as the roots of the characteristic polynomial $p(E)$. We can infer the form (abbreviating $\epsilon_{\mathbf{k}}$ as ϵ)

$$p(E) = \det(E - H_{\mathbf{k}}) \tag{3.31}$$
$$= \det(E - h - \epsilon\kappa) \tag{3.32}$$
$$= \sum_{0 \le i+j \le 4} c_{ij}(h, \kappa) E^i \epsilon^j. \tag{3.33}$$

Since the characteristic polynomial of a $N \times N$ matrix is a polynomial in its entries (of total degree N), we can write $p(E)$ as a degree four polynomial in E and ϵ. For a flat band, this polynomial should have a root (as a function of E) whose value is independent of ϵ. It is clear that this can only be true for a quite special class of polynomials, and our task is to show that the symmetries of the system appropriately constrain the parameters c_{ij}. Specifically, we will demonstrate that the band flattening can be achieved by tuning our final free parameter J.

The particle-hole symmetry implies that the roots E^* of $p(E)$ are symmetric about zero, which implies that only terms even in E appear. Further, from the derivation in Sec. 3.1 one can see that flipping the sign of ϵ (or rather exchanging $\mathbf{k} \leftrightarrow \mathbf{k} + \mathbf{Q}$) is the same as flipping spin-up and spin-down, which should not have any effect as the magnetic moments are located in the x-y-plane. As a result, $p(E)$ must also be even in ϵ. Thus $c_{ij} \neq 0$ only if i and j are both even.

To proceed further, we consider the limits $\epsilon = 0$ and $\epsilon \to \infty$. They respectively yield

$$\sum_{0 \le i \le 4} c_{i0}(h, \kappa) E^i = \det(E - h), \tag{3.34}$$
$$c_{04}(h, \kappa) = \det(\kappa) = 0. \tag{3.35}$$

The second equality in (3.35) follows from (3.30): κ is a 4×4 matrix, but its definition also includes the 2×4 matrix W. If we take a (four dimensional) vector v so that $\sqrt{Z}v$ is orthogonal to both vectors corresponding to the two rows of W, we have $\kappa v = 0$. Thus, κ must be singular.

Putting these things together we get

$$p(E) = \det(E - h) + c_{02}\epsilon^2 + c_{22}E^2\epsilon^2. \tag{3.36}$$

We now set E to one of the eigenvalues of h, $E^*(h)$. This results in

$$p(E^*(h)) = \epsilon^2 \left(c_{02} + c_{22} E^*(h)^2 \right) \tag{3.37}$$
$$= \epsilon^2 f(J). \tag{3.38}$$

If we can tune J so that $f(J)$ vanishes, the right side will be identically zero. Thus, $E^*(h)$ is a root of the characteristic polynomial independent of ϵ and forms a flat band. Of course, if and where such roots occur depends on c_{02} and c_{22}, which are complicated functions of J. In our calculation we have one root at $J = 1.04t$, the transition point from AFII to AFI.

Summarizing, the following conditions facilitate the existence of the flat band:

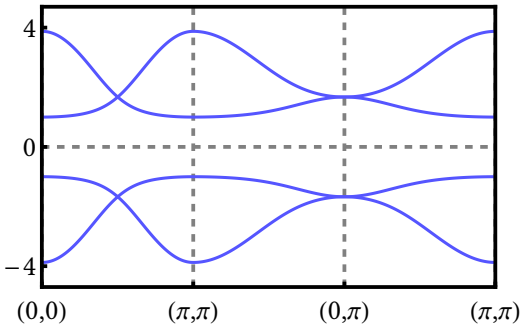

Figure 3.7: Band structure calculated using the method of Jurecka and Brenig, $J = 1.1t$ (the antiferromagnetic phase). Note that the band crossing at $(\pi/2, \pi/2)$.

- The effective Hamiltonian is only four-dimensional.
- Particle-hole symmetry reduces the number of independent eigenvalues.
- The kinetic energy matrix κ has a zero mode.

3.2.3 Antiferromagnetism in the Jurecka-Brenig theory

Jurecka and Brenig applied their technique (described in Sec. 2.5.2) to the square lattice at half-filling, yielding a critical interaction strength $J_c = 1.5t$ (very close to the QMC result) [53]. We have repeated their calculation and extended it to the doped case: as described in Sec. 2.5.2, this corresponds to modifying the definition of $\sqrt{Z}$. Further, we also mentioned that they ignored local pairing terms $\langle a_{\mathbf{R}\sigma} b_{\mathbf{R}\tilde{\sigma}} \rangle_0$, etc., whereas in the Gutzwiller approximation they are explicitly set to zero using the Lagrange multiplier matrix Λ (which needs to be solved for). We can simulate their calculation by, instead of solving for Λ as for the Gutzwiller approximation, simply dropping Λ altogether (or equivalently, fixing $\Lambda = 0$). This corresponds to minimizing the variational energy without any restrictions on $\langle a_{\mathbf{R}\sigma} b_{\mathbf{R}\tilde{\sigma}} \rangle_0$, etc. For completeness, we have also tried the "hybrid" approach of using $\sqrt{Z}$ as in the Jurecka-Brenig calculation, but Λ as in the Gutzwiller approximation.

The most striking difference to the Gutzwiller approximation is that there is no indication of the small Fermi surface (AFII) phase, as a large Fermi surface state is found for any interaction strength. Let us first discuss the calculation with $\Lambda = 0$.

The underlying reason for the lack of a phase transition was, in fact, already mentioned by Jurecka and Brenig themselves. Looking at the band structure in the antiferromagnetic phase (Fig. 3.7), one notices that the lower (upper) bands touch each other at $(\pi/2, \pi/2)$. This should be compared with Fig. 3.3 (b), where the AFI phase shows a clear gap between the bands. The discrepancy exists because in the Jurecka-Brenig method the antiferromagnetic scattering in the effective Hamiltonian is also proportional to $\epsilon_{\mathbf{k}}$. For $(\pi/2, \pi/2)$, we have $\epsilon_{\mathbf{k}} = 0$, so the bands do not repel. Accordingly, the mechanism of the band minimum at $(\pi/2, \pi/2)$ turning into a maximum is also impossible, and the AFII phase cannot be obtained.

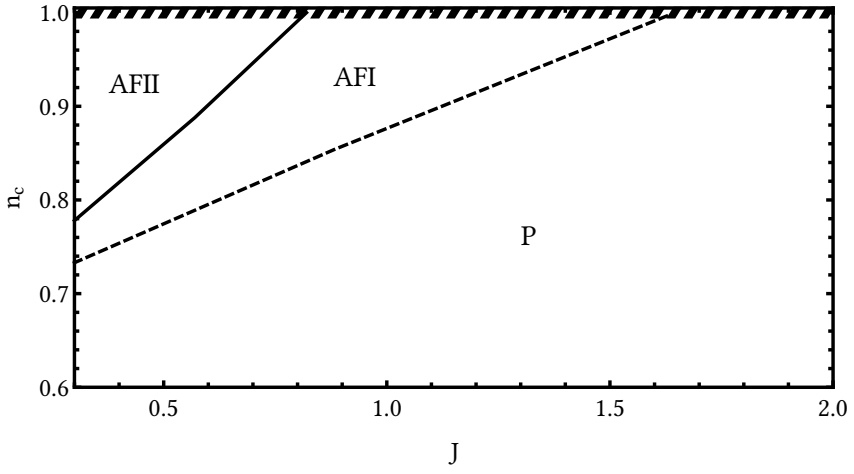

Figure 3.8: Same as Fig. 3.1, but for $t' = -0.4t$.

Since the magnetic vector points in the x-direction, antiferromagnetic scattering terms are precisely the spin-flip terms in the effective Hamiltonian. In (3.25), such terms appear as the off-diagonal terms of m and in Λ, which result in a band coupling (and thus repulsion) independent of $\mathbf{k}$. Of these, m is numerically much more important, as it corresponds to scattering that conserves the bond fermion number, while Λ corresponds to creation or annihilation of bond fermions (which is suppressed by the excitation gap). The Jurecka-Brenig theory in contrast has a diagonal m, as $\sqrt{Z}$ is proportional to the identity matrix.

Choosing the "hybrid" option (meaning, adding Λ) results only in a very small correction to the band structure. This is too little to induce the Lifshitz transition. It also changes the position of the critical point to $J_c = 1.3t$, less accurate the previous result. The Gutzwiller approximation thus seems more in line with other numerical calculations (which also found a Lifshitz transition in the antiferromagnetic phase).

3.2.4 Next-nearest neighbor hopping

We will now also briefly discuss the $t' \neq 0$ case. The phase diagram is qualitatively similar, although the antiferromagnetic regions become smaller (Fig. 3.8). Especially the size of the AFII phase is reduced, which can be interpreted as a consequence of the decreased nesting in the free band structure. The two magnetic phases can again be recognized by their qualitatively differing Fermi surfaces (Fig. 3.9). However, since the lattice is no longer bipartite and particle-hole symmetry is broken, one can no longer directly identify the Fermi surfaces with those of a free system. $\epsilon_{\mathbf{k}}$ and $\epsilon_{\mathbf{k}+\mathbf{Q}}$ are essentially independent quantities and act as two different $\mathbf{k}$-dependent parameters in the effective Hamiltonian, so the hole pockets do not have to follow lines of constant $\epsilon_{\mathbf{k}}$. The AFII Fermi surface is no longer ring-like surrounding the center of the Brillouin zone, but instead consists of disconnected hole pockets at $(\pi/2, \pi/2)$ and symmetrically equivalent positions. Still, the AFI-AFII transition is similar to before, as the maximum near $(\pi/2, \pi/2)$ flips around at the transition. One must note that due to the reduced symmetry, the conduction band

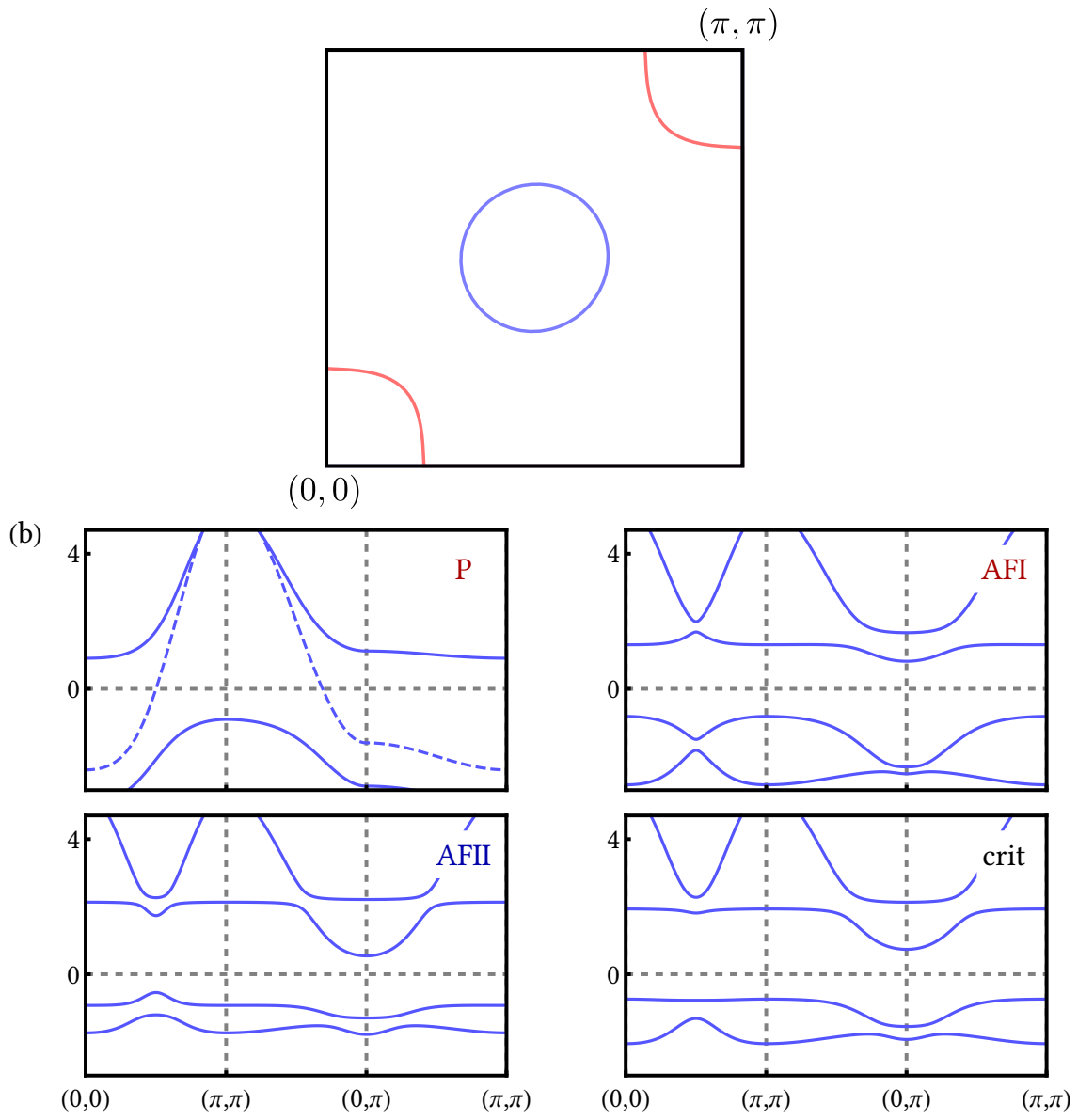

Figure 3.9: Fermi surface and band structures for $t' = -0.4$.

(a) Fermi surfaces for AFI ($J = 0.5t$, red) and AFII ($J = 0.62t$, blue), with $n_c = 0.9$. Unlike for $t' = 0$, the Fermi surfaces cannot be identified with those of a free system.

(b) Band structures for $n_c = 1$. From left to right and top to bottom, we have $J = 1.62t$ (P, the dashed line is the free band structure for comparison), $J = 1.3t$ (AFI), $J = 0.5t$ (AFII), and $J = 0.82t$ (critical point).

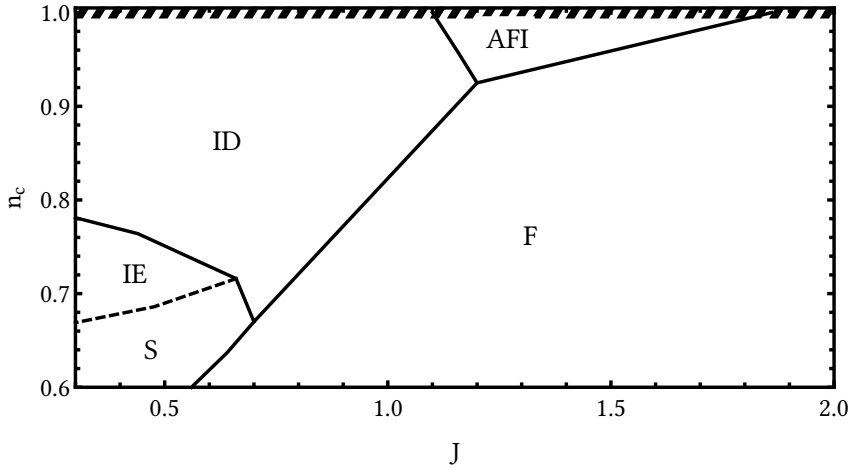

Figure 3.10: Phase diagram with incommensurate and ferromagnetic phases. The dashed line indicates a second-order transition, all other transitions are discontinuous. Explanations of each phase can be found in the main text.

no longer becomes globally flat at the critical point, but there remains a line of almost dispersionless excitations along the diagonal of the Brillouin zone (Fig. 3.9 (b)). The density of states will thus still drastically increase near the transition point.

3.3 Ferromagnetic and incommensurate phases

We now turn our attention to the more general case of arbitrary $\mathbf{Q}$. This includes the antiferromagnetic phases that were already discussed, but also ferromagnetism ($\mathbf{Q} = (0, 0)$) and more general spiral order. It turns out that all phases except AFI are unstable against such non-Néel ordering. The resulting phase diagram is pictured in Fig. 3.10. Notably, the paramagnetic phase is replaced by ferromagnetism (F). The other major change is in the area previously occupied by the small Fermi surface AFII phase, which is replaced by a sequence of phases with non-trivial $\mathbf{Q}$:

- ID: incommensurate phase with a wave vector lying along a *diagonal* of the Brillouin zone, $\mathbf{Q} = (q, q)$
- IE: incommensurate phase with a wave vector lying along an *edge* of the Brillouin zone, $\mathbf{Q} = (q, \pi)$
- S: commensurate phase with *stripe* magnetic order along a coordinate axis, $\mathbf{Q} = (0, \pi)$

Pure antiferromagnetism remains only at half-filling, and in the AFI phase. More generally, the situation at half-filling is completely unchanged, and the two critical interaction values have the same values as before.

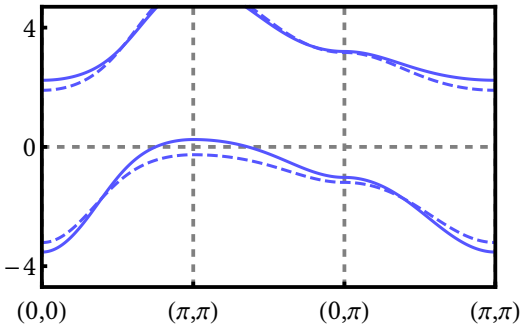

Figure 3.11: Band structure in the ferromagnetic (F) phase with $n_c = 0.9$ and $J = 2.02t$. Dashing indicates the quasiparticle spin of each band.

We will now discuss possible explanations for the appearance of each of these phases, beginning with the F phase. Close to half-filling, the band structure is qualitatively identical to the paramagnetic phase, except for a splitting of the bands (Fig. 3.11). In fact, the splitting is always strong enough to completely polarize the Fermi surface, resulting in one conducting and one insulating band. This type of "spin-selective" Kondo insulator has previously been proposed by Peters et al. in both infinite dimensions [95] and in one dimension [92] (in this case, perturbatory expansion in t/J leads to a rigorous proof of ferromagnetism in the $J \to \infty$ limit [103]). The same phase was also found in two dimensions [27, 94]. Further details of this ferromagnetic phase will be discussed in Chapter 4.

The results of these studies differ from ours in that ferromagnetism is only present at low conduction electron concentration $n_c \lesssim 0.5$, whereas in our calculation polarization is present at arbitrarily small doping. From a purely mathematical standpoint, it seems that the F phase is caused by a Stoner-like mechanism aided by the large density of states of the very heavy conduction band. A small ferromagnetic admixture to the triplet background is only weakly punished by the Kondo interaction, but increases hopping processes for the polarized bond fermions. Furthermore, the number of hard-core collisions is reduced by a polarization of the conduction bands. Only at quite large $J \sim 8t$ does the Kondo interaction win out and the system becomes paramagnetic.

While this ferromagnetic phase at small doping seems unphysical to us, we can very roughly judge how "far off" we are from the more likely paramagnetic solution. For this we turn to previous dynamical cluster approximation (DCA) [15] and Gutzwiller approximation [68] studies, where the model was investigated with an applied magnetic field. In both cases, the calculated magnetization profile was qualitatively similar (Fig. 3.12): with increasing B-field the magnetization quickly saturates (we call this field B_s), with a *metamagnetic* transition at larger field strength. The ferromagnetic phase we have found corresponds to the saturated region. While quantitative comparisons are difficult, the figures in the references indicate that the magnetic field needed for saturation is quite small: In the DCA calculation, which has $n_c = 0.9$, $J = 1.3t$, and a ratio of Landé factors $g_f/g_c = 4$, the magnetization saturates at $B_s \approx 0.002t$. In the Gutzwiller calculation,

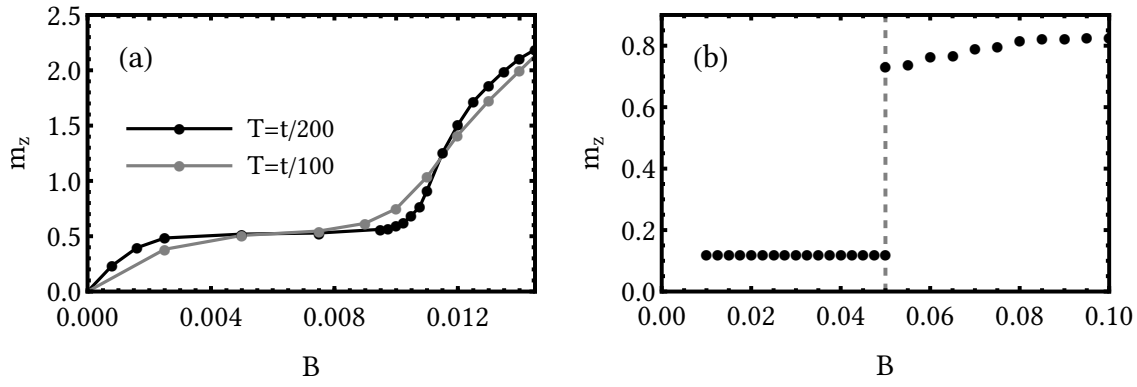

Figure 3.12: Magnetization as a function of an external magnetic field found by (a) Bercx et al. using DCA for two different temperatures [15], and (b) Lanatà et al. using Gutzwiller approximation [68]. The results are not directly comparable (see the text for more information), but a "saturated" plateau is visible in both graphs.

which has $n_c = 0.88$, $J = 0.45D$ (where D is the half-bandwidth, in our case $4t$), and equal Landé factors $g_f = g_c$, $B = 0.01D$ is already in the saturated region. We take these small values of the magnetic field needed for full polarization as a sign that even at low doping the Kondo lattice is energetically quite close to the fully polarized ferromagnetic state; however, triplet fluctuations (which we do not take into account) should destroy ferromagnetism near half-filling. A closer discussion of the effect an external field has on the system (and of the metamagnetic transition) is found in Chapter 4.

We now turn to the incommensurate phases. Doping away from half-filling with $J < J_{c,2}$, $\mathbf{Q}$ smoothly moves away from the Néel vector (π, π), towards the origin along the diagonal of the Brillouin zone (Fig. 3.13). This forms the ID phase. For $J \gtrsim 0.6t$, further doping leads directly to a phase transition to F. In the case of small J, one instead first finds another incommensurate phase of different symmetry, where $\mathbf{Q}$ jumps towards the edge of the Brillouin zone (IE). From there, the system transitions smoothly to a commensurate phase of the form $\mathbf{Q} = (0, \pi)$: the magnetic moments are laid out in alternating stripes with inequivalent x- and y-axes (S).
We can compare these results to the mean-field calculations of Costa et al. [27] and Pankratova et al. [91], which should be reasonably accurate for small J. While Costa et al. allow for c-f hybridization, this is only relevant in phases featuring Kondo screening. In our region of interest, their calculation is equivalent to that of Pankratova et al., except that the latter allow for phase separation. As we have not investigated phase separation ourselves, we will focus on the results of Costa et al.

The bond fermion and mean-field phase diagrams are similar to a point, as the mean-field theory also predicts two different kinds of antiferromagnetism and stripe magnetism. However, there are significant quantitative differences. For example, as Fig. 3.13 shows, when fixing $J = 0.5t$ the crossover between the ID and IE phases occurs near $n_c = 0.76$ in our calculation. For Costa et al., the transition always occurs for $n_c > 0.9$ even at larger $J = 2.4t$.

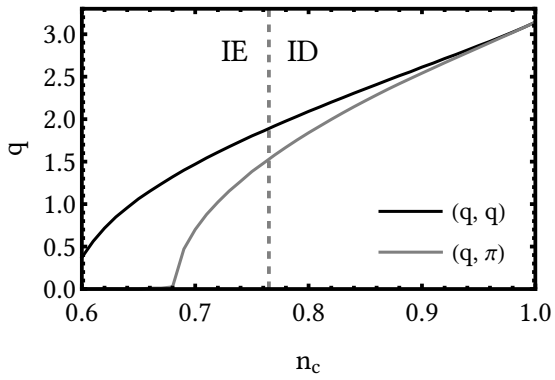

Figure 3.13: Evolution of the optimal $\mathbf{Q}$ for fixed $J = 0.5t$ at varying doping. $\mathbf{Q}$ is restricted either to the diagonal (ID, $\mathbf{Q} = (q, q)$) or the edge (IE, $\mathbf{Q} = (q, \pi)$) of the Brillouin zone. The vertical line signifies the phase transition between ID and IE: on the right side, (q, q) has lower energy, to the left it is (q, π). For $q = 0$ or $q = \pi$, we have commensurate magnetic order.

Similar to how the diagonal parts of the Gutzwiller matrix m cause a gap to remain even for $J = 0$, they here also "amplify" J (compare ϵ_{eff} in Sec. 2.6). Thus, the choice of $\mathbf{Q}$ still influences the strength of the hopping (and the variational energy) even for a very small or vanishing J, which is unphysical. From this standpoint it may actually be a positive surprise that, even in the region where the bond fermion wave function is not an appropriate ansatz, our phase diagram is still comparable to the mean-field result. However, we must assume that the ID phase is in truth confined to a much smaller region that in our phase diagram, the IE phase growing larger in turn. For another opinion, one can consult the DMFT results of Peters and Kawakami [94]. While they did not investigate incommensurate order, they also support the existence of a striped magnetic phase near $n_c = 0.5$.

3.4 Discussion and comparison to experiments

In summary, the bond fermion theory generally performed according to expectations. Restricted to antiferromagnetism, we find both a magnetic transition and a transition between small and large Fermi surface phases. The Gutzwiller approximation improved results compared to the previous bond fermion calculations, and leads to the novel prediction of a divergent band mass at the critical point $J_{c,2}$ and half-filling. Other features like the quasiparticle pole can also be calculated and show expected behavior.

For general ordering vectors, some problems appear. While quantitative inaccuracies at small interaction may be excused by the strong-coupling nature of the ansatz, we also find a likely unphysical ferromagnetic region at larger J. We will discuss ferromagnetic polarization more in depth in the next chapter. Before this, however, we will give a small overview over possible connections to experimental results for heavy fermion systems. While the Kondo lattice model is generally seen as providing a good description of basic heavy fermion physics, it is clear that such simple and abstract model will not adequately

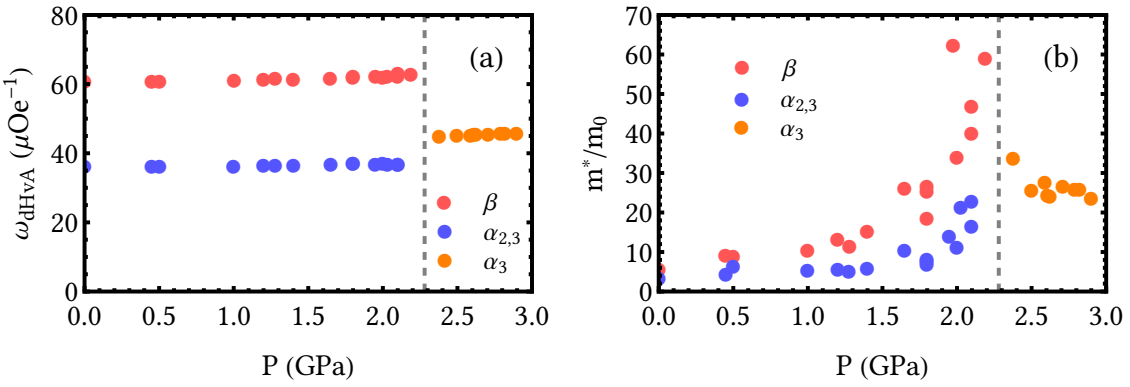

Figure 3.14: Measurements for $CeRhIn_5$ under pressure by Shishido et al. [102]. Shown are (a) de Haas-van Alphen frequencies and (b) mass enhancement based on the cyclotron resonance, for selected Fermi surfaces (β and $\alpha_{2,3}$ to the left of the transition and α_2 to the right).

describe a real material. Nevertheless, there are some compounds that seem to relate quite directly to model calculations like ours, which we will summarize here.

A chief example is $CeRh_{1-x}Co_xIn_5$, which shows some striking similarities to the Kondo lattice model phase diagram obtained above [39]. Ignoring its superconducting phase, the compound is incommensurately ordered at $x = 0$. Doping first leads to a transition to a commensurate antiferromagnetic phase with a reconstructed Fermi surface, and then to a paramagnetic phase. Fermi surface imaging suggests that the incommensurate phase has a small Fermi surface, while the commensurate phase has a large one. reconstruction they should be included in the Fermi surface volume. Superficially, this mirrors multiple aspects of our phase diagram, as we can find analogues of these phases in our calculations. The incommensurate phase would correspond to either IE or ID (which both have a small Fermi surface) and the commensurate one to the AFI phase (large Fermi surface). If we start out in IE/ID and assume Co-doping to be equivalent to increasing J/t, we have a similar sequence of phase transitions to the experiment. At the first transition the Fermi surface is reconstructed to include the f-electrons, and the ordering vector becomes commensurate. Magnetic order as a whole vanishes later, at a second transition.

Of course, the analogy is imperfect. The real material is three-dimensional and strongly anisotropic, with a quasi-layered $HoCoGa_5$ structure [46]: instead of in-plane spiral order as in our two-dimensional description, the incommensurability is in the out-of-plane direction with a wave vector $\mathbf{Q} = (\pi/a, \pi/a, q/c)$. Further, unlike our calculation, no sign of a significant narrowing of the bands was found near the transition.

If one instead takes pure $CeRhIn_5$ and applies pressure, one gets a direct transition from incommensurate antiferromagnetism to paramagnetism [102], with no intermediate commensurate state. According to our calculation this is also possible in the Kondo lattice, albeit only at lower electron densities. Results from de Haas-van Alphen and cyclotron resonance measurements are shown in Fig. 3.14. What is particularly interesting here is that while the de Haas-van Alphen frequencies (Fig. 3.14 (a)) of each band seem to be almost constant on each side of the transition (indicating that the Fermi surface does

not change much), some of the effective masses seem to diverge (Fig. 3.14 (b)). This is unlike the doping-induced transition, and fits with our observation that the Fermi surface reconstruction is associated with a significant flattening of the valence band near the transition. A similar pressure-induced transition was observed in $CeRh_2Si_2$ as well [8], also featuring the mass enhancement.

A different, much-studied example for incommensurate magnetic order is given by the system $CeCu_2(Si_{1-x}Ge_x)_2$ [58, 59, 87, 105]. This compound has the layered $ThCr_2Si_2$ structure and the Fermi surface takes the form of warped cylinders [105] so that a description by a planar model may be reasonable. This system shows incommensurate magnetic order with an ordering vector close to $\mathbf{Q} = (\pi/2a, \pi/2a, \pi/c)$, whereby the ordered moment forms a spiral in the plane perpendicular to $\mathbf{Q}$ [59]. It has to be noted, however, that in $CeCu_2Si_2$ the ordering vector has been shown [105] to correspond to a nesting vector of the heavy quasiparticle Fermi surface obtained for the paramagnetic phase by the renormalized band structure method. In this picture the antiferromagnetic phase would correspond to a spin-density-like instability of the large Fermi surface, that is the AFI phase in the present theory. This interpretation would therefore not be consistent with the present theory, where the incommensurate phase replaces the AFII phase.

4 Effect of a magnetic field

Inspired by the results of the previous chapter, we will try to understand the effect of an externally applied magnetic field **B** on the phase diagram of the system. As the bond fermion method predicts a saturated ferromagnetic state even without a magnetic field, some limitations exist. For example, we cannot describe the transition to the saturated region, or give an estimate of the magnetic field B_s required to reach it (in this sense we have $B_s = 0$, while the references have $B_s > 0$). However, this does not a priori imply that we cannot describe the saturated region itself or the behavior of the system at much larger field strengths. In this parameter region we can also investigate the interplay of antiferromagnetism and ferromagnetic polarization.

4.1 Calculation

To stay within the mathematical description of the investigation so far, we apply the magnetic field out-of-plane in the z-direction. This implies that we should allow a (spatially constant) triplet component t_z in our ansatz for the wave function, in addition to the in-plane antiferromagnetism of the previous sections. As a vector in the z-direction is unaffected by the transformation in Sec. 3.1, the ansatz reads

$$\mathbf{B} = B\hat{e}_z, \tag{4.1}$$

$$\mathbf{t} = t_x\hat{e}_x + t_z\hat{e}_z, \tag{4.2}$$

$$s = \sqrt{1 - t_x^2 - t_z^2}. \tag{4.3}$$

In the original (laboratory) system, this corresponds to a *canted* ordering vector that is constant out-of-plane and rotating in-plane. For simplicity, we restrict ourselves to in-plane Néel order ($\mathbf{Q} = (\pi, \pi)$). A purely ferromagnetic phase in this formulation corresponds to $t_x = 0$ (unlike the previous section, the ferromagnetic polarization is out-of-plane and parallel to the magnetic field).

Other choices for the ordering vector are possible. For example, one might include an oscillating component in the z-direction (possibly even setting $t_x = 0$, corresponding to *ferrimagnetic* ordering). This would however have the side effect of charge disproportionation, as different sites cannot be related through a symmetry transformation. Reflecting this, the canonical transformation to the primed system cannot remove a fluctuation in t_z, so the calculation would have to explicitly introduce multiple sublattices. As we are mostly interested in purely magnetic dynamics, we stick with (4.2).

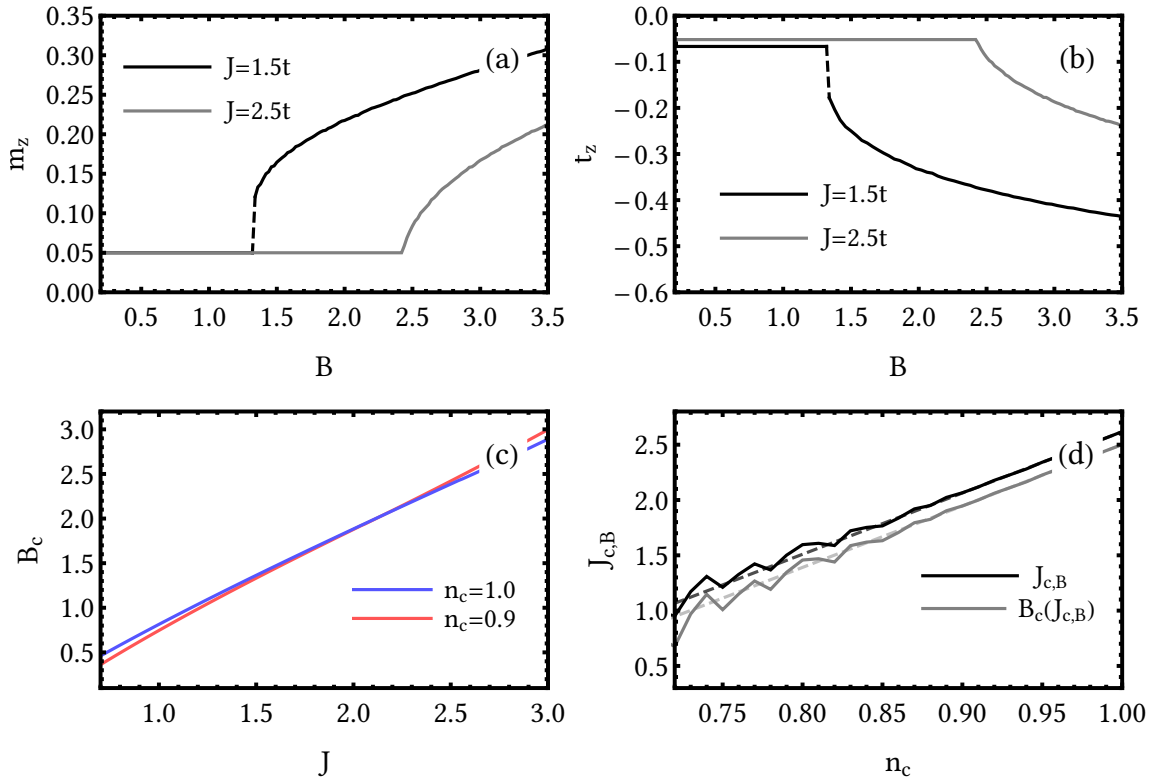

Figure 4.1:

(a–b) Net magnetization m_z and bond fermion parameter t_z across the metamagnetic transition, for $n_c = 0.9$.

(c) Critical field B_c.

(d) Critical interaction $J_{c,B}$ (and the critical field B_c at the critical interaction). For $J > J_{c,B}$, the metamagnetic transition is continuous. The dashed lines are linear fits, $J_{c,B}/t \approx 2.62 - 5.54\delta$ and $B_c(J_{c,B})/t \approx 2.50 - 5.50\delta$ with $\delta = 1 - n_c$.

To implement the calculation, only a few expressions of (3.25–3.28) have to be modified. Of course, t_z has to be included in W, see (2.179). The magnetic field $\mathbf{B}$ must be added to the local part of the effective Hamiltonian, which now reads

$$h = e\,\mathrm{diag}(-1,-1,1,1) - \frac{B}{2}\,\mathrm{diag}(-1,1,1,-1) - \Lambda - m - \mu. \tag{4.4}$$

We used $B \geq 0.2t$ for our calculation. In the regions of J and n_c we are interested in, this should easily be strong enough for a completely polarized conduction band (no matter whether the solution method is bond fermion theory, dynamical cluster approximation, or anything else). Since we have fixed $\mathbf{Q}$, the optimization parameters determining the energy are now t_x and t_z, which are handled analogously to the previous chapter.

4.2 Metamagnetism

Let us first fix $t_x = 0$ (corresponding to a purely ferromagnetic phase) and apply an increasing B, since this is the most commonly studied case in the literature. As mentioned in the previous chapter (and demonstrated in Fig. 3.12), the usual result is that of a metamagnetic transition: At first, the magnetization remains constant (saturated) at small fields. We call this phase FI, and it is equivalent to F in the previous section. Then, at a critical value B_c, there is a transition to a qualitatively different phase, which we refer to as FII. However, the details of this transition in the Kondo lattice are not entirely clear: for example, Bercx and Assaad (Fig. 3.12 (a)) find that the magnetization is continuous across the transition, whereas Lanatà et al. (Fig. 3.12 (b)) show a curve with a clear jump.

We also reproduce the transition, but with a twist. Typical curves for the magnetization m_z and the bond fermion parameter t_z are show in Fig. 4.1 (a–b) (the negative sign of t_z will be discussed later), and indeed the magnetization is constant in the FI phase with $m_z = (1-n_c)/2$ corresponding to the completely polarized band structure. The magnetization only starts rising in the FII phase, with a transition at the critical field B_c (shown in Fig. 4.1 (c)). As one can see, B_c increases with J, but is only weakly dependent on n_c. What is striking is that the metamagnetic transition in Fig. 4.1 (a–b) shows qualitatively different behavior depending on J: for smaller J, there is a clear jump in the magnetization, whereas for large J no discontinuity is visible. We call this behavior *selectively continuous*; the critical interaction strength below (above) which the transition is discontinous (continuous) is called $J_{c,B}$ and shown in Fig. 4.1 (d). The selectively continuous behavior suggests a simple resolution to the literature controversy: it is possible that each of the literature results gives a snapshot of the complete phase diagram, with Berckx and Assaad below $J_{c,B}$, and Lanatà et al. above $J_{c,B}$.

Before we proceed further however, we do have to make some remarks on the numerical procedure. Fig. 4.1 (d) shows some numerical noise, especially far away from half-filling. This is because the real value of $J_{c,B}$ is difficult to establish. The energy profile as a function of t_z is shown in Fig. 4.2 (a). (a1) shows that for $J < J_{c,B}$ we have a region in B where two local minima $t^*_{z,1}$ (blue) and $t^*_{z,2}$ (red) coexist, the minima respectively corresponding to FI and FII. The discontinuous transition takes place when the energies of the minima cross. (a2) has $J > J_{c,B}$ and no coexistence region is found; instead, $t^*_{z,1}$ smoothly morphs into $t^*_{z,2}$ and there is no discontinuity. The numerical problems arise because the minima in (a1) are both very shallow, and that $t^*_{z,2}$ (the minimum at large t_z) moves very quickly as a function of B (Fig. 4.1 (a–b) show square-root behavior above the transition, so that $\partial t^*_{z,2}/\partial B \to \infty$). For our calculation, we find $t^*_{z,1}$ by minimizing the energy for $B \ll B_c$ (note that $t^*_{z,1}$ is constant); $t^*_{z,2}$ is traced by starting at $B \gg B_c$ and then slowly lowering B, each time starting the optimization at the previous value of $t^*_{z,2}$. Due to the divergence of $\partial t^*_{z,2}/\partial B$, we continuously have to reduce the size of the steps in B; the procedure is continued until we can no longer find a separate minimum (that is, until the optimization returns $t^*_{z,2} = t^*_{z,1}$ within a small tolerance). Results are shown in Fig. 4.2 (b), where Δt_z is the distance between the minima at $B = B_c$. Several "steps" are visible, which are artifacts of the rather error-prone tracing procedure. We calculate $J_{c,B}$ by fitting a (quadratic) polynomial to Δt_z and extrapolating it to zero.

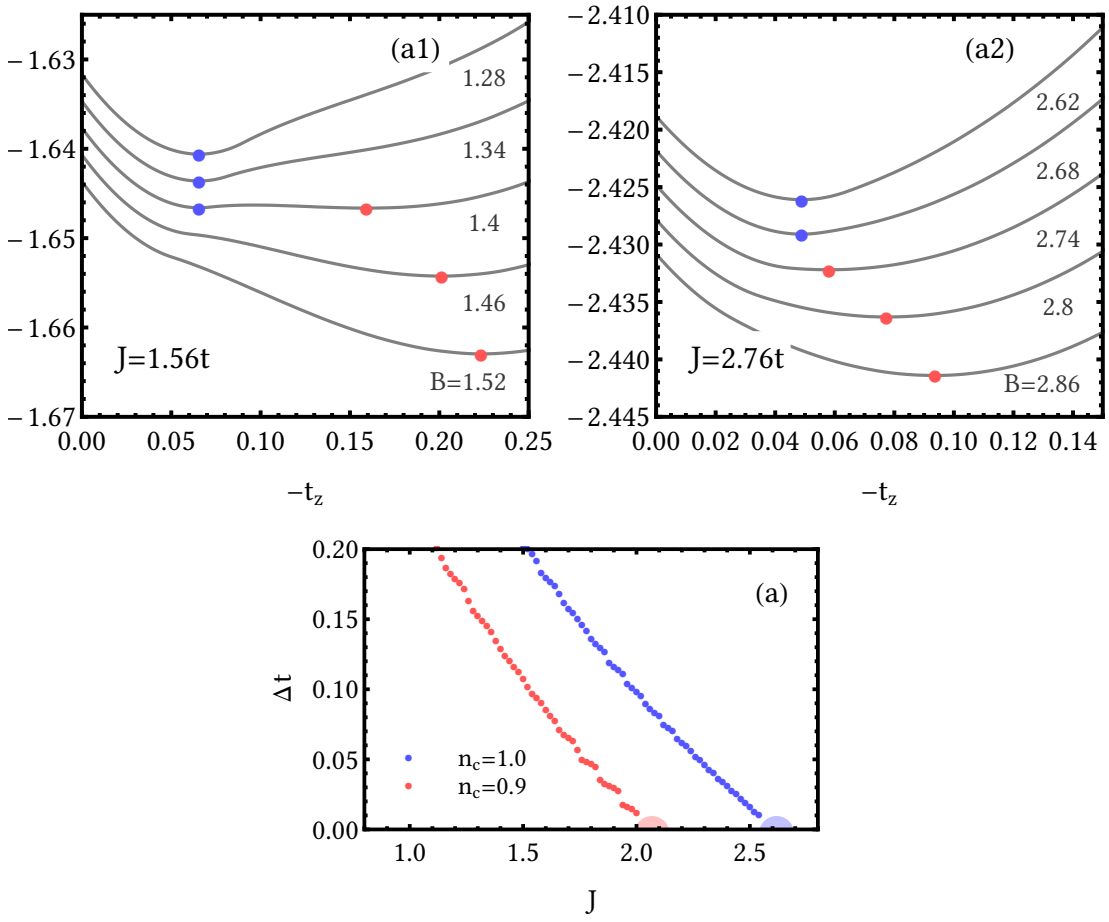

Figure 4.2:

(a) Variational energy $\langle H \rangle (t_z)$ for different magnetic fields. For low fields ($B < B_c$) the minimum's position is constant (red dots), but then starts to shift (blue dots). (a1) has $J < J_{c,B}$, and there is a small range where two minima coexist ($B = 1.4t$); the (discontinuous) metamagnetic transition corresponds to the energy crossover between the minima.
(a2) has $J > J_{c,B}$, where no coexistence region is detected; the minimum starts moving continuously at the transition.

(b) Discontinuity Δt_z at the transition. The shaded regions correspond to the position of the $J_{c,B}$ extrapolated from the (noisy) data.

While this method gives a smooth result at least for $n_c \gtrsim 0.85$ (see Fig. 4.1 (d)), there is certainly room for improvement. For example, by lowering the grid spacing and temperature for our numerical integration (here $\pi/50$ and $0.005t$, respectively) one may be able to smooth out the curves in Fig. 4.2 (b) somewhat further, at the cost of significantly increased processor time. However, we do not regard this as too critical and have relegated it to future work: in the pathological region, the accuracy of the bond fermion calcula-

tion will be inherently limited due to the neglect of fluctuations, no matter how well the numerical procedure is carried out.

Let us now give a more thorough description of the metamagnetic transition from a band structure perspective, starting with the continuous region ($J > J_{c,B}$). The Fermi surfaces and band structures are shown in Fig. 4.3. At small B (FI phase, red line in Fig. 4.3 (a)), the Fermi surface resembles that of the paramagnetic, large Fermi surface from before (compare the Fig. 3.3 (a)), with a single hole pocket at (π, π). However, the diameter of the hole pocket has increased as compared to the paramagnetic phase, as it now only holds quasiparticles of one spin direction (spin-down, to be specific), the others having wandered below the Fermi energy due to the magnetic polarization (the top two graphs in Fig. 4.3 (b)). This behavior is the same as the F phase in Chapter 3. The magnetization is saturated and the Fermi surface locked to a specific line of constant $\epsilon_{\mathbf{k}}$. This continues until $B = B_c$, when the bottom of an electron band "breaks through the band gap" due to the strong magnetic field (bottom two graphs in Fig. 4.3 (b)), causing an electron pocket to form around $(0, 0)$. The metamagnetic transition is thus a Lifshitz transition. Increasing B further expands both the old hole pocket and the new electron pocket. In the bond fermion description, this corresponds to the generation of many spin-up a- and b-fermions, as for large enough magnetic field this becomes favorable energetically. Accordingly, the magnetization of the system also starts to rise again coincident with the Lifshitz transition, leading to the metamagnetic behavior we saw in Fig. 4.1 (a–b). It should be noted that, while both the Fermi surfaces still have to follow lines of constant $\epsilon_{\mathbf{k}}$ inside the FII phase, they are no longer "locked": as the pocket around $(0, 0)$ is an electron pocket, only the *difference* in the volumes of both pockets must be constant.

In other words, the transition occurs when the magnetic field is large enough to overcome the lowest excitation energy above the gap. Calling the energy of this band $E_\Delta(\mathbf{k})$, the minimum is at $\mathbf{k} = (0, 0)$, so that we have $B_c = E_\Delta(0, 0)$[1]. This also explains why we seem to have $B_c \propto J$ in Fig. 4.1 (c), as $B_c \sim E_\Delta(0, 0) \sim \Delta \propto J$.

The relation $B_c = E_\Delta(0, 0)$ breaks down at $J_{c,B}$, as one can see in Fig. 4.4 (a). This corresponds to the discontinuous region: at smaller J, a significant deviation from a Kondo singlet (i.e. a large t_z) is not punished as strongly by the Kondo interaction. This means that the metamagnetic transition is energetically favorable even before $B = E_\Delta(0, 0)$; the rest of the "effective field" needed to overcome the gap is provided by a spontaneous polarization of the system itself. As for the evolution of the Fermi surface for $J < J_{c,B}$, it is effectively the same as for $J > J_{c,B}$, except that one jumps directly from the first to the last graph in Fig. 4.3 (b): before the band around $(0, 0)$ touches the Fermi surface, there is a discontinuous transition to a Fermi pocket with finite size.

[1] $E_\Delta(0, 0)$ should be computed for $B = 0$, but t_z at its saturated value. Note that for $n_c = 1$, we get $E_\Delta(0, 0) = \Delta$ because $t_z = 0$.

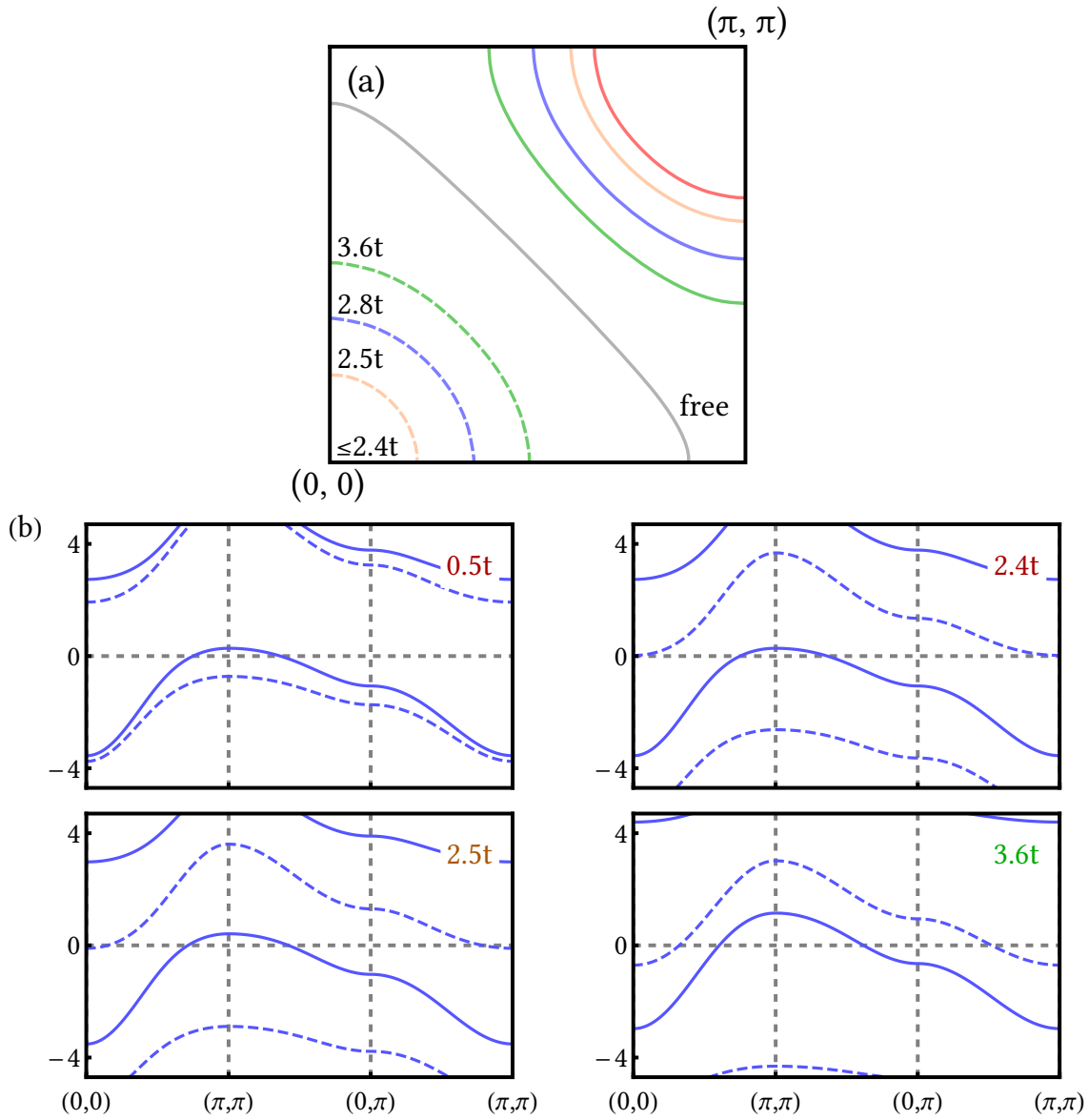

Figure 4.3: Evolution of the Fermi surface across the metamagnetic transition, with $n_c = 0.9$ and $J = 2.5t$ fixed and varying $0.5t \leq B \leq 3.6t$. See Fig. 4.1 (a) for the corresponding magnetization $m_z(B)$.

(a) The Fermi surfaces for varying B. Solid (dashed) lines correspond to spin-down hole (spin-up particle) surfaces. For $B \leq 2.4t$ the system is in the FI phase with only a hole pocket (red), above the critical value $B_c = 2.45t$ ($B = 2.5t, 2.6t, 3.5t$) a particle pocket gradually emerges around $(0, 0)$. A free electron band structure is shown in grey for comparison.

(b) The corresponding evolution of the band structures. The dashing again corresponds to the quasiparticle spin. For $B = 0.5t$ the bands above and below the gap are still well-separated, for $B = 2.4t$ they have almost touched (but the Fermi surface has not actually changed yet, so the system is still FI). At $B = 2.5t$ a small pocket forms (the metamagnetic transition), which then gradually grows in size ($B = 3.6t$).

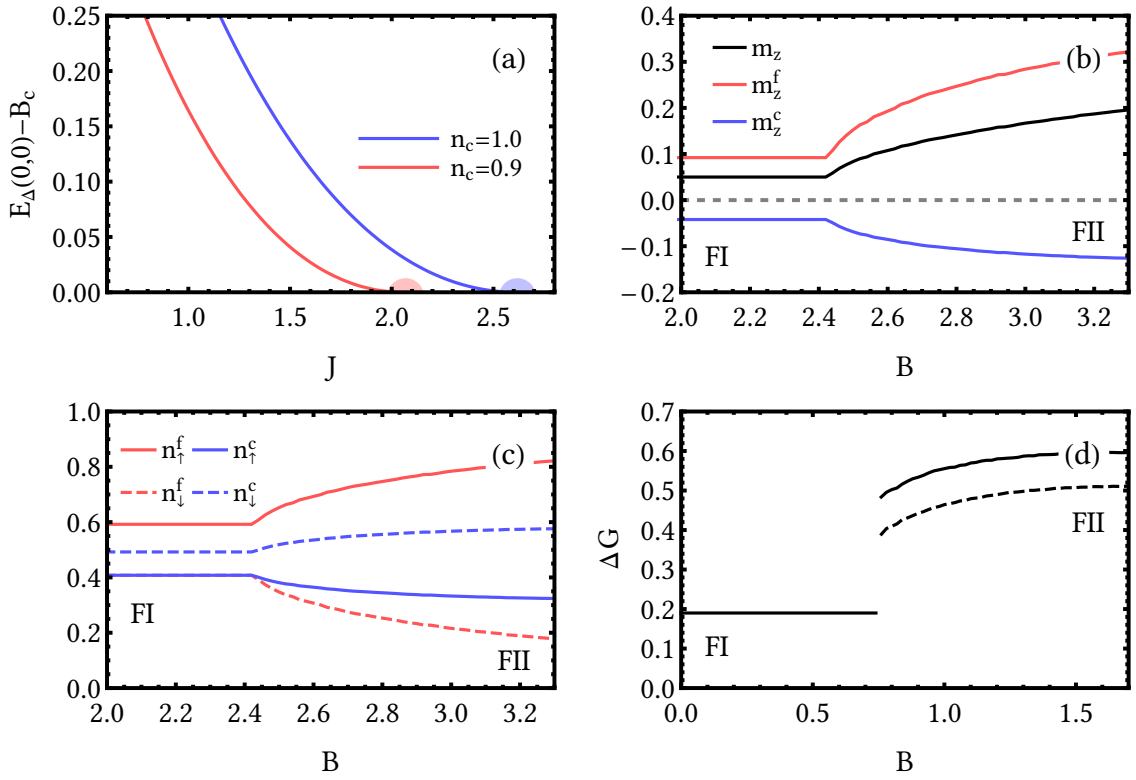

Figure 4.4:

(a) Difference between $E_\Delta(0,0)$, the lowest excitation above the gap, and B_c. The difference vanishes at $J_{c,B}$.

(b–c) Decomposition of the magnetization and electron density into individual contributions across the metamagnetic transition, for $n_c = 0.9$ and $J = 2.5t$.

(d) Quasiparticle residue for $n_c = 0.9$ and $J = t < J_{c,B}$. On the right side of the transition there are two inequivalent Fermi surfaces, the full (dashed) line corresponds to the a- (b-) like Fermi surface. The b-like surface vanishes at $J_{c,B}$.

Let us now take a closer look at how the magnetic polarization actually arises in the bond fermion wave function. First, let us explain the sign of t_z For this, one should look back all the way to Sec. 2.2. As was noted there, for real $\mathbf{t}_\mathbf{R}$, the background polarization is exactly opposite for c- and f-electrons and thus *does not* carry any net spin, no matter the value of t_z. Writing (2.2–2.5) out explicitly we have

$$|\Omega\rangle_\mathbf{R} = \frac{(s+t_z)c^\dagger_{\mathbf{R}\uparrow}f^\dagger_{\mathbf{R}\downarrow} + (s-t_z)c^\dagger_{\mathbf{R}\downarrow}f^\dagger_{\mathbf{R}\uparrow}}{\sqrt{2}}\,|0\rangle_\mathbf{R}\,. \tag{4.5}$$

The effect of t_z is only that it becomes easier or harder to generate bond fermions with a given spin direction, which *does* result in a net spin. As the spin of a bond fermion is physically carried by f-electrons, we should choose t_z in a way that the weight of

background f-electrons with spin-up is increased; from (4.5) we then get $t_z < 0$. In general, the magnetization of the system is roughly opposite to $\mathbf{t}_\mathbf{R}$.

We can decompose the magnetization into its c- and f-parts, see Fig. 4.4 (b)[2]. Thus, as one can guess from (4.5), the spins of conduction and localized electrons point in opposite directions because of J. However, the conduction spin is reduced from its background value by charge fluctuations, so a net magnetization remains. This effect is even stronger in the FII phase, where conduction, spin, and net magnetization are significantly larger.

For a physical interpretation of the FII phase, it is helpful to decompose the spin even further into the spin-dependent electron densities (Fig. 4.4 (c)). We see that inside the FI phase, we have $n^f_\downarrow = n^c_\uparrow$, a tell-tale sign of the spin-selective Kondo insulator of Peters et al. [95]. This identity can be interpreted as a spin-dependent Kondo screening, as each spin-down f-electron is paired with a screening spin-up electron, while some spin-up f-electrons remain unscreened. Earlier, we have associated such a screening breakdown with two other features: A Fermi surface transition (from large to small) and an increase in the quasiparticle residue ΔG. Both of these phenomena are also present here:

The large-small transition is not as clear-cut as before, but a connection to a free electron system can still be made. FI is easily interpreted as a large Fermi surface phase (the free system having n_c+1 electrons with completely polarized charge carriers, a *half-metal*). For FII, one should think about what happens to a free system with n_c electrons (gray line in Fig. 4.3 (a)) if we add a magnetic field: the gray line will Zeeman-split in two and come to resemble that of the FII Fermi surfaces. Curiously, the behavior with increasing B is *opposite* to that of the Kondo lattice, as the distance between the spin-split Fermi surfaces *increases* with B. In the Kondo lattice the distance *decreases*, as the breakdown of screening causes the Fermi surface to resemble that of the free system more and more.

Finally, we do in fact find the expected transition in ΔG, see Fig. 4.4 (d): the FI phase is more strongly correlated (has a smaller ΔG) than the FII phase.

4.2.1 An alternative ansatz

We will end this section with a small digression. So far, we have tacitly accepted that the c- and f-spins should be opposed to each other because of the Kondo interaction. However, in a magnetic field a parallel orientation of spins is quite natural. Should we then not also allow admixture of such a state to the background? This was indeed the approach in Ref. [110], where the background state was chosen as (in our notation, with $\mathbf{Q} = 0$)

$$|\Omega\rangle_\mathbf{R} = s\,|S\rangle_\mathbf{R} + |\mathbf{t}|\,|\uparrow\uparrow\rangle_\mathbf{R}\,, \tag{4.6}$$

$$|\uparrow\uparrow\rangle_\mathbf{R} = c^\dagger_{\mathbf{R}\uparrow} f^\dagger_{\mathbf{R}\uparrow}\,|0\rangle_\mathbf{R}\,. \tag{4.7}$$

[2] Here we have $J > J_{c,B}$; $J < J_{c,B}$ is qualitatively the same, but with a jump instead of a continuous rise.

While this is an obvious choice ($|\uparrow\uparrow\rangle_{\mathbf{R}}$ is the ground state for $B \to \infty$), in practice some problems arise. Namely, $|S\rangle_{\mathbf{R}}$ and $|\uparrow\uparrow\rangle_{\mathbf{R}}$ have different spin, so that the resulting state does not conserve the z-spin. Indeed, comparing with (2.3), one finds that

$$|\uparrow\uparrow\rangle_{\mathbf{R}} = \frac{-|T_x\rangle_{\mathbf{R}} + i\left|T_y\right\rangle_{\mathbf{R}}}{\sqrt{2}}, \tag{4.8}$$

$$\Rightarrow \mathbf{t} = \frac{|\mathbf{t}|}{\sqrt{2}}(-\hat{e}_x + i\hat{e}_y). \tag{4.9}$$

(2.26–2.27) then give background expectation values of

$$\langle\Omega|\mathbf{S}^c_{\mathbf{R}}|\Omega\rangle_{\mathbf{R}} = -\frac{s|\mathbf{t}|}{\sqrt{2}}\hat{e}_x + \frac{|\mathbf{t}|^2}{2}\hat{e}_z, \tag{4.10}$$

$$\langle\Omega|\mathbf{S}^f_{\mathbf{R}}|\Omega\rangle_{\mathbf{R}} = +\frac{s|\mathbf{t}|}{\sqrt{2}}\hat{e}_x + \frac{|\mathbf{t}|^2}{2}\hat{e}_z. \tag{4.11}$$

While the total background spin is parallel to the z-axis, both c- and f-spin have significant in-plane components (typically larger than the z-components, since these are quadratic in $\mathbf{t}$). As the c-spin is reduced by charge fluctuations and can be mostly neglected, the final magnetization will point mostly along the x-axis. This also explains why Ref. [110] found a *decrease* in $|\mathbf{t}|$ when turning on a magnetic field in the z-direction.

As with most issues in bond fermion calculations, the problem with ansatz (4.9) lies in the neglect of fluctuations: in this case, the particular problem is *phase fluctuations*. (4.6) has specified a particular phase relationship between $|S\rangle_{\mathbf{R}}$ and $|\uparrow\uparrow\rangle_{\mathbf{R}}$ (specifically, that they have the same phase). Multiplying $|\uparrow\uparrow\rangle_{\mathbf{R}}$ with a complex phase corresponds simply to a z-rotation (for example, multiplying by i would result in polarization along the y-axis in (4.10–4.11)). By fixing the phase, one has thus introduced an artificial breaking of the *a priori* cylindrical symmetry of the problem.

The symmetric choice ($\mathbf{t} \propto \hat{e}_z$) we made in our own calculation does not suffer from these drawbacks. Furthermore, it also has the advantage that flipping $B \to -B$ simply results in $t_z \to -t_z$ (whereas in (4.6) one needs to replace $|\uparrow\uparrow\rangle_{\mathbf{R}}$ by $|\downarrow\downarrow\rangle_{\mathbf{R}}$), which is likely to be advantageous for small-to-moderate values of B. Our choice of real t_z does not break any further symmetry, as from (2.27) it is apparent that choosing a different phase influences $\langle S^f_z\rangle$ (with real t_z giving the largest possible background value).

However, simply neglecting $|\uparrow\uparrow\rangle_{\mathbf{R}}$ is quite unsatisfactory, which again calls for further research into a proper treatment of triplet fluctuations. If all phase fluctuations are treated on even footing, the effect of fluctuations into $|\uparrow\uparrow\rangle_{\mathbf{R}}$ could be included while correctly preserving the cylindrical symmetry.

4.3 Canted phase diagram

We now allow for both $t_x \neq 0$ and $t_z \neq 0$. We emphasize that we still have $\mathbf{B} \propto \hat{e}_z$, so that a finite t_x (which corresponds to an in-plane antiferromagnetic polarization) is entirely spontaneous. The resulting phase diagram for $B = 0.2t$ is shown in Fig. 4.5.

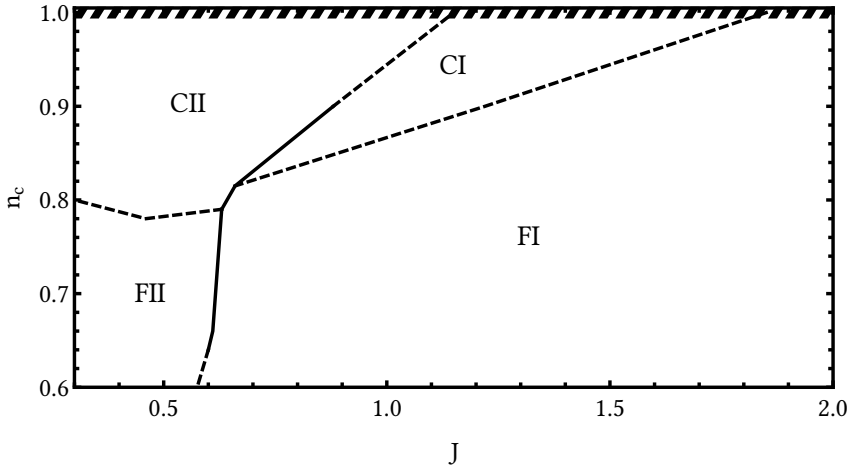

Figure 4.5: The phase diagram for $B = 0.2t$, taking into account canted and ferromagnetic phases.

Due to the magnetic field, we find that t_z is always nonzero. There are two types of phases, depending on whether t_x is zero or finite: The ferromagnetic phases (FI and FII) have $t_x = 0$ and have been discussed in the previous section; the *canted* phases (CI and CII) have $t_x \neq 0$. The canted phases respectively are the analogues of the AFI and AFII phases. The magnetic phase diagram is superficially similar to the nonmagnetic phase diagram Fig. 3.1: roughly speaking, the paramagnetic region is replaced by FI and FII, and the antiferromagnetic phases AFI and AFII are replaced by their canted equivalents. However, this neglects some striking differences that have appeared due to the magnetic field, which we will discuss now.

4.3.1 Softening of the heavy fermion transition

We start with the most significant difference. In Fig. 3.1, the phase transition between AFI and AFII was discontinuous except at exactly half-filling. Meanwhile, in Fig. 4.5, the dashed phase border implies that the CI-CII transition is continuous in a finite region around half-filling. Only for $n_c \lesssim 0.9$ do we find a discontinuity across the transition, see for example **t** in Fig. 4.6 (a). The size of the jump is shown in Fig. 4.6 (b): in the region where the jump is zero, the transition corresponds *only* to a Lifshitz transition, with no discontinuity in any other system parameters. We thus have again have a selectively continuous transition, but this time between canted phases.

This behavior is quite unexpected: recall that for each of the AFI and AFII phases, the Fermi surfaces were locked, so that a continuous transition could only happen at half-filling (where there are no Fermi surfaces at all because of the gap). It turns out that this argument *does not* apply to the canted phases CI and CII, as one can see from the Fermi surfaces and band structures in Fig. 4.7: the Fermi surface is *not* locked throughout the CII phase. Instead, for small J it starts out near the original AFII Fermi surface, i.e. near $(\pi/2, \pi/2)$, and then (for increasing J) "wanders" towards $(0, 0)$. The transition to CI then corresponds to the vanishing of one of the Fermi surfaces as the "ring" closes

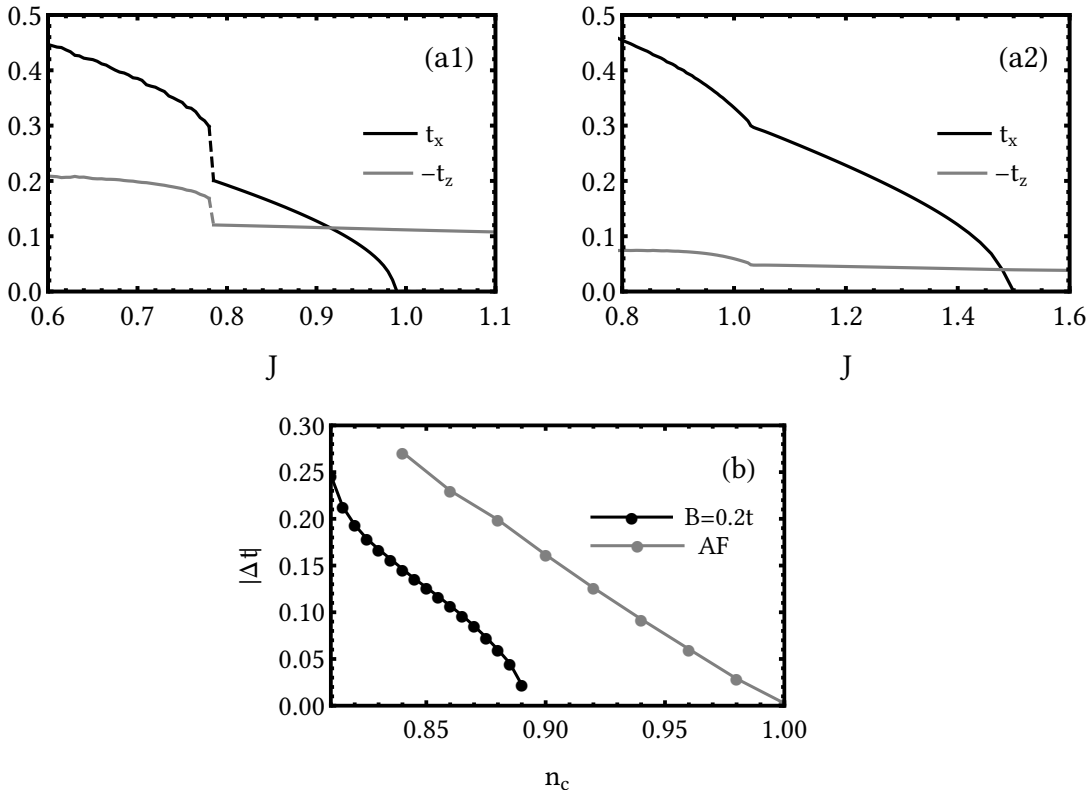

Figure 4.6:

(a) t_x and t_z for $n_c = 0.86$ / $n_c = 0.97$ and $B = 0.2t$. (a1) shows two phase transitions: A clear jump (dashed lines) between CII and CI, and then a continuous vanishing of t_x at larger J (FI phase). In (a2), the transition between CII and CI only results in a kink in the curves, without a discontinuity. Note that $t_z < 0$ as before, whereas the sign of t_x is arbitrary.

(b) Size of the discontinuity $|\Delta \mathbf{t}|$ at the CI-CI transition. No discontinuity is detected $n_c \geq 0.9$. The AFI-AFII transition is shown for comparison; there, $|\Delta \mathbf{t}|$ only vanishes for $n_c = 1$.

around $(0, 0)$ (inside the CI phase the Fermi surface is indeed locked). For $n_c > 0.9$, the wandering is continuous all the way through (the Fermi surface smoothly deforms with J); for $n_c < 0.9$ the wandering is cut short (the Fermi surface smoothly deforms part of the way towards $(0, 0)$, but then suddenly jumps the rest of the way), which is associated with the discontinuity in $\mathbf{t}$. One should note that this is very similar in essence to the selectively continuous metamagnetic transition of the previous section, but described in reverse (for the metamagnetic transition, the "natural starting point" is the low-B FI phase, whereas for the canted transition it is the low-J AFII phase).

The form and evolution of the Fermi surfaces requires some further explanation. First of all, one notices that the canted Fermi surfaces are not symmetric when mirroring around

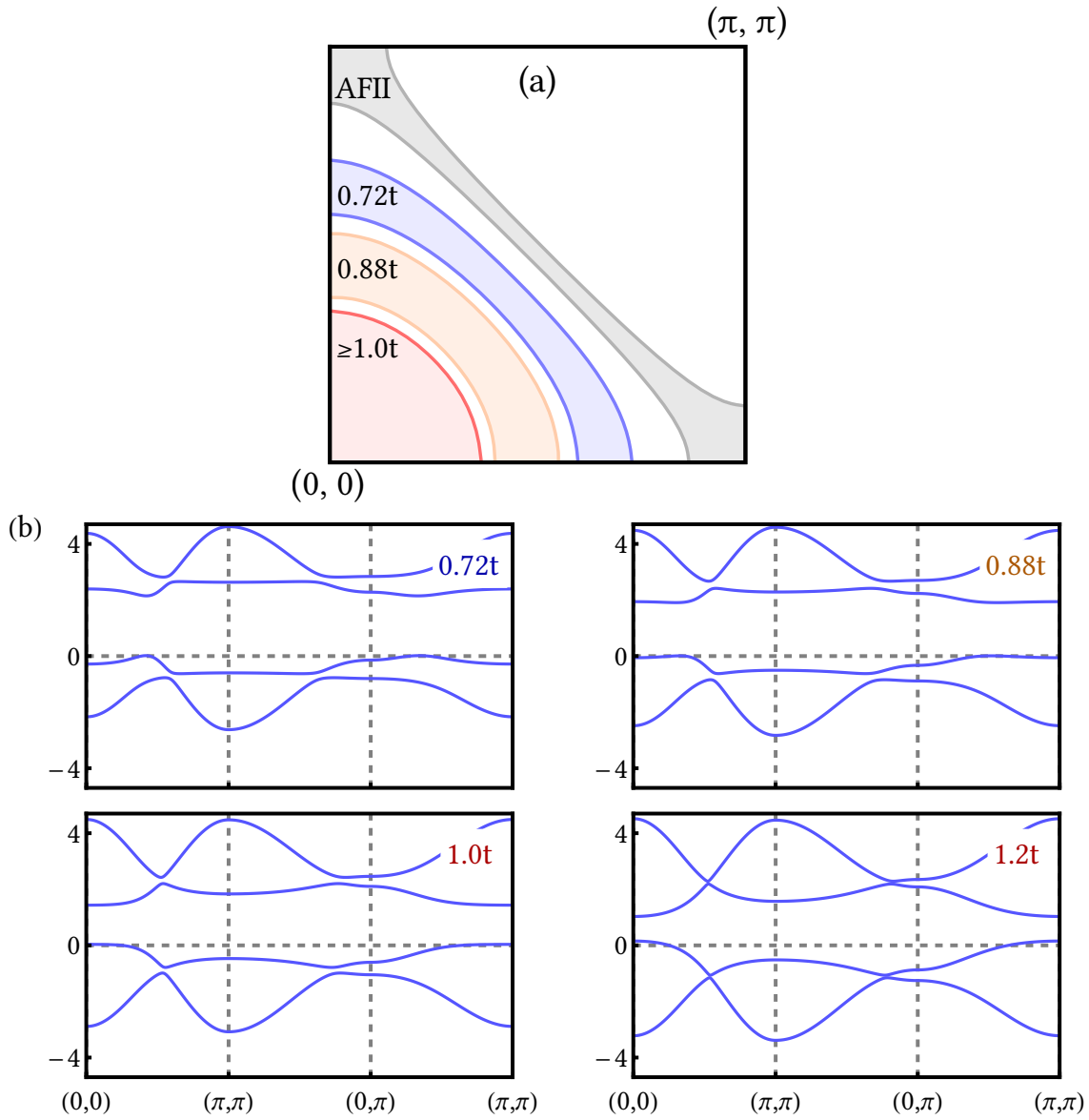

Figure 4.7: Evolution of the Fermi surface across the CI-CII transition, with $n_c = 0.9$ and $B = 0.2t$ fixed and varying $0.72t \leq J \leq 1.2t$ (note that in Fig. 4.3 it was instead B that was varying). The z-spin is not conserved, so we cannot unambiguously identify bands as spin-up or spin-down.

(a) Fermi surfaces for varying J. The system gradually evolves from a ring-like structure in the CII phase ($J = 0.72t, 0.88t$, blue and orange) to a single Fermi pocket in the CI phase ($J \geq 1.0t$). The AFII band structure is shown in grey for comparison. Note that only AFII is symmetric about the diagonal.

(b) Corresponding evolution of the band structures. The maximum of the valence band, and thus the Fermi surface, gradually moves towards $(0, 0)$ ($J = 0.72t, 0.88t$). After the transition to the CI phase ($J = 1.0t$), the band structure keeps changing but the position of the Fermi surface is constant ($J = 1.2t$).

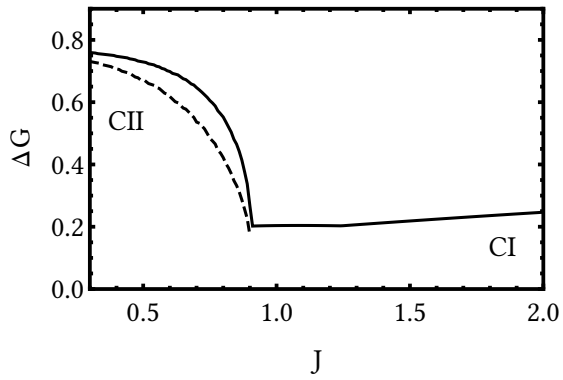

Figure 4.8: Quasiparticle residues for the canted phases across the CII-CI transition, $n_c = 0.9$ and $B = 0.2t$. There are two inequivalent Fermi surfaces: The full (dashed) line corresponds to the Fermi surface further from (closer to) $(0, 0)$. The Fermi surface closer to $(0, 0)$ vanishes when the "ring" closes around $(0, 0)$, see Fig. 4.7 (a).

the diagonal $(\pi, 0)$–$(0, \pi)$. This may seem impossible since, after all, we still have Néel-like two-sublattice order, which usually implies exactly such a symmetry: actually, in a description with two explicit sublattices, $\mathbf{k}$ and $\mathbf{k}+\mathbf{Q}$ are *the same point*. However, we are not using such a two-sublattice description, but instead use a canonically rotated system with only one sublattice. Here, as we remarked in Sec. 3.2.2.1, the mirror symmetry instead corresponds to a spin-flip symmetry: $\mathbf{k}$ and $\mathbf{k}+\mathbf{Q}$ are *different points*, but they can be related by flipping the z-spin. In a two-sublattice description, the momentum $\mathbf{k}$ would include all the degrees of freedom which are in our description split over $\mathbf{k}$ and $\mathbf{k}+\mathbf{Q}$. This is closer to the physical reality, but does not reflect the mathematical symmetries of the system as well[3].

The reason the AFI and AFII Fermi surfaces (Fig. 3.3 (a)) are still mirror-symmetric in the canonically rotated system is that they are unaffected by a z-flip (the magnetization was purely in-plane). We cannot transform AFI and AFII into each other without introducing another intermediate phase with different Fermi surface topology. However, with the magnetic field, the z-flip symmetry (and with it mirror symmetry) is broken. This has two direct consequences. First, the AFII Fermi surface, which was locked to the diagonal as it had to obey the mirror symmetry, is now the CII Fermi surface, which is "mobile". Second, one of the AFI pockets is pushed below the Fermi energy (giving the CII Fermi surface), as there is now a Zeeman-like energy difference between the bands at $(0, 0)$ and (π, π). These two effects combined allow for a continuous transformation between CI and CII.

This "softened" transition between CI and CII further demonstrates that, once a magnetic field is added, the distinction between large and small Fermi surface is looser than before. Instead, the CII phase can smoothly go from large (with the Fermi surface near $(\pi/2, \pi/2)$ to small (near $(0, 0)$). Equivalently, in the common parlance, the f-electrons

[3] In simpler words, to get to the physical Fermi surfaces (the ones that would be found by e.g. ARPES), an antiferromagnetic partner should be added to each Fermi surface in Fig. 4.7 (a).

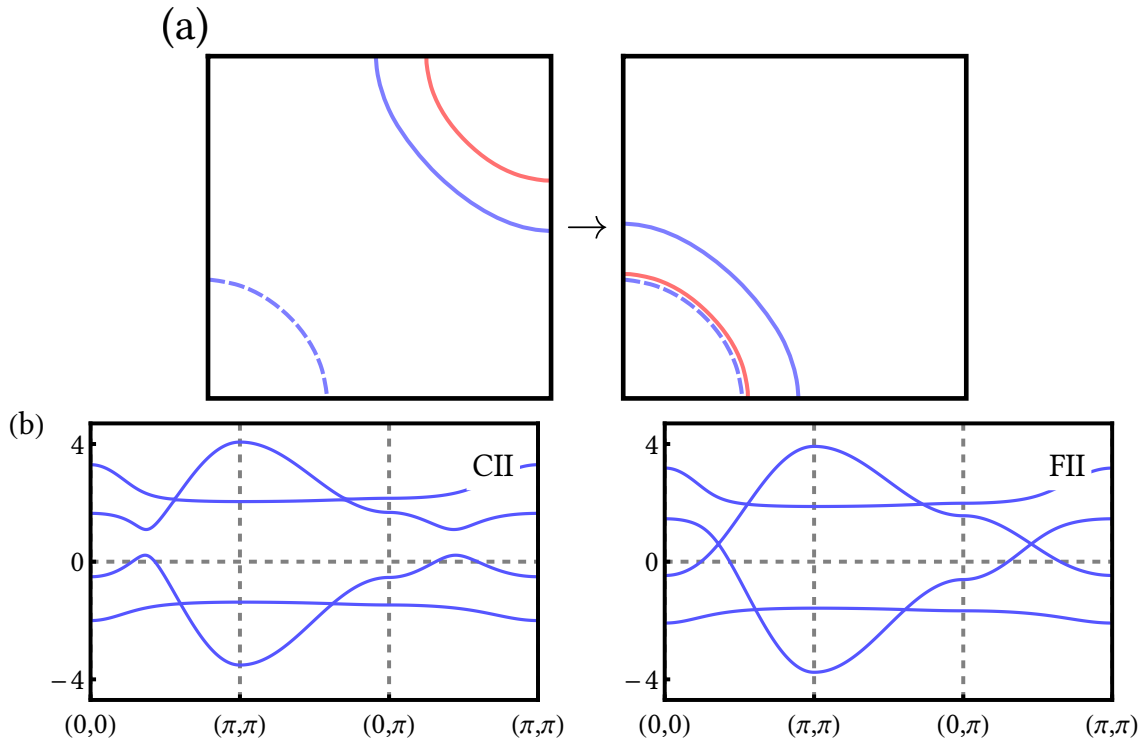

Figure 4.9:

(a) The effect of the canonical rotation on the ferromagnetic Fermi surfaces (FII in blue and FI in red), compare Fig. 4.3 (a): the spin-down Fermi surfaces (full lines) are translated by $\mathbf{Q}$ by the transformation.

(b) The CII-FII transition ($B = 0.2t$, $J = 0.5t$, $n_c = 0.8, 0.76$ respectively) with the FII band structure drawn in the rotated frame, compare to FII in Fig. 4.3 (b). The transition causes an antiferromagnetic gap to close, but no Lifshitz transition occurs. The CI-FI transition is analogous.

"drop out" gradually, instead of abruptly, as is the common situation. For further evidence of this, we can again estimate the importance of correlations using the quasiparticle residue ΔG, see Fig. 4.8. ΔG drops sharply but continuously, at least for the Fermi surface that is retained across the Lifshitz transition. If and how this new mechanism could be measured experimentally is discussed in Sec. 4.4.

As a final note, the continuity of the transition even for $n_c < 1$ also means that half-filling is no longer "special", except that the system becomes insulating. For example, the flat band at the AFI-AFII transition (section 3.2.2) is no longer present. Mathematically, this results from the inequivalence of $\mathbf{k}$ and $\mathbf{k} + \mathbf{Q}$ (see for example the band structures in Fig. 4.7 (b)).

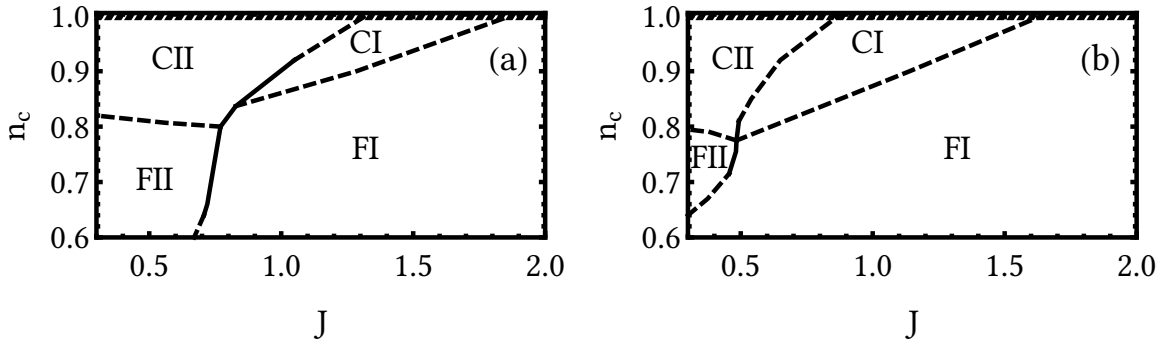

Figure 4.10: Phase diagrams for (a) $B = 0.4t$ and $t' = 0$ and (b) $B = 0.2t$ and $t' = -0.4t$.

4.3.2 Canted-ferromagnetic transitions

The smaller novelty in the phase diagram Fig. 4.5 is that the transition from CII to FII is now also continuous. Earlier, only the AFI-P transition was continuous, whereas AFII-P was always associated with a finite jump in $\mathbf{t}$. To explain why this is possible, we again have to "match up" the Fermi surfaces. At first glance, they do not seem to fit each other: Comparing the FII Fermi surface (e.g. orange lines in Fig. 4.3 (a)) to the CII Fermi surface (e.g. orange lines in Fig. 4.7 (a)), their topologies are superficially different; FII has pockets around $(0, 0)$ and (π, π), whereas CII has both pockets around $(0, 0)$. To resolve this, we must again take into account the canonical rotation, as Fig. 4.3 (a) is drawn in the unrotated ($\mathbf{Q} = 0$) system. The transformation is shown in Fig. 4.9 (a): effectively, the solid lines (which are Fermi surfaces made out of spin-down quasiparticles) are translated by $\mathbf{Q}$ (equivalently, flipped along the diagonal), which results in the same "ring" structure we have in the CII phase. An analogous reasoning applies to the FI and CI phases. Note that this means that the canted-ferromagnetic transitions are not accompanied by Lifshitz transitions. Indeed, Fig. 4.9 (b) shows that the effect of $t_z \to 0$ is a closing of an antiferromagnetic gap significantly above the Fermi energy.

The last transition to discuss is the FI-FII border in Fig. 4.5. This is simply the metamagnetic transition, but at constant B and with varying J (as opposed to the earlier case of constant J and varying B).

4.3.3 Stronger magnetic field and $t' \neq 0$

Finally, we want to quickly check how robust the previous results are against a modification in some of the system parameters. First, we choose a somewhat higher magnetic field, $B = 0.4t$. The resulting phase diagram (Fig. 4.10 (a)) is almost identical to the previous one. The main effect of the magnetic field (i.e., a strong polarization of the system) was already achieved by the lower field, so it makes sense that a further increase would not greatly alter our findings. Qualitatively, the relative sizes of the CII and FII regions have increased, as these are the unscreened (or rather, lightly screened) phases, which are favored by a magnetic field. Of course, as we mentioned at the start, the more interesting case of $B \to 0$ is sadly unavailable to us.

The other modification is to include a second-nearest neighbor hopping term $t' = -0.4t$ (with $B = 0.2t$). Our previous arguments regarding the (dis-) continuities relied on the specific forms of the Fermi surfaces, so it is not clear whether they will survive the complication of having $\epsilon_{\mathbf{k}+\mathbf{Q}} \neq -\epsilon_{\mathbf{k}}$. The phase diagram (Fig. 4.10 (b)) shows that they do, as we again find a very similar phase diagram, including the softening of the CI-CII transition. The evolution of the Fermi surfaces is analogous, see Fig. 4.11 (a), and we have a single Fermi pocket that wanders to the center of the Brillouin zone. The reasoning is the same as before: As the z-spin symmetry is broken, the Fermi surfaces do not need to be mirror symmetric in the canted phases, allowing for a continuous transition. The FI-FII transition (here driven by J) is also equivalent to before (i.e. a particle pocket around $(0, 0)$ appears in the FII phase).

We thus see that the softened CI-CII transition is not dependent on the particle-hole symmetry present at $t' = 0$, but rather more general. In fact, we expect the results for a three dimensions to be similar, as our arguments did not explicitly refer to the dimensionality of the system.

4.4 Summary and discussion

Summarizing, we have found that an out-of-plane magnetic field results in strong qualitative changes in the physics of the Kondo lattice, both in the presence and in the absence of in-plane antiferromagnetism. For strong magnetic fields or strong doping, Zeeman splitting overpowers the gap and Kondo screening breaks down. At smaller fields, the breaking of spin-flip symmetry softens the transition between small and large Fermi surface phases. In fact, even the concept of large and small Fermi surfaces must be approached with care, as the transition between them becomes continuous.

Regarding the details of the metamagnetic transition, we find it to be selectively continous, i.e. depending on J, it may or may not be associated with a discontinuity. A very similar observation was also made by Kubo [64] for the related periodic Anderson model.

A different controversy we have not yet discussed is about the true "nature" of the metamagnetic transition. The DCA band structures show that the Kondo gap does not close in the metamagnetic phase, but is merely moved away from the Fermi energy. The mean-field calculation of Kusminskiy et al. [109] instead predicts a complete localization of the f-electrons at the transition, so that the spectrum is gapless. Our results (which feature only "partial" f-localization) are naturally closer to that of DCA, as the bond fermion ansatz cannot describe a complete decoupling of localized and itinerant electrons. In contrast however, the bond fermion method predicts a $B_c \sim J$ (as $B_c \sim \Delta$), which is similar to mean-field theory. DCA instead gives a much smaller gap and critical field ($B_c \lesssim 0.1t$ for $J \approx t$). To add onto the confusion, quantum Monte Carlo [9] gives a gap of $\Delta \approx 0.6t$ in this range, which seems to imply that the true B_c is somewhere in between the DCA and bond fermion results.

Metamagnetic transitions (i.e. step-like anomalies in the magnetization at a finite magnetic field) are very common in real heavy fermion materials, although their origins are unclear. The most important question is whether the transition actually involves a heavy fermion transition (somewhat equivalently, a breakdown of screening), as predicted by the

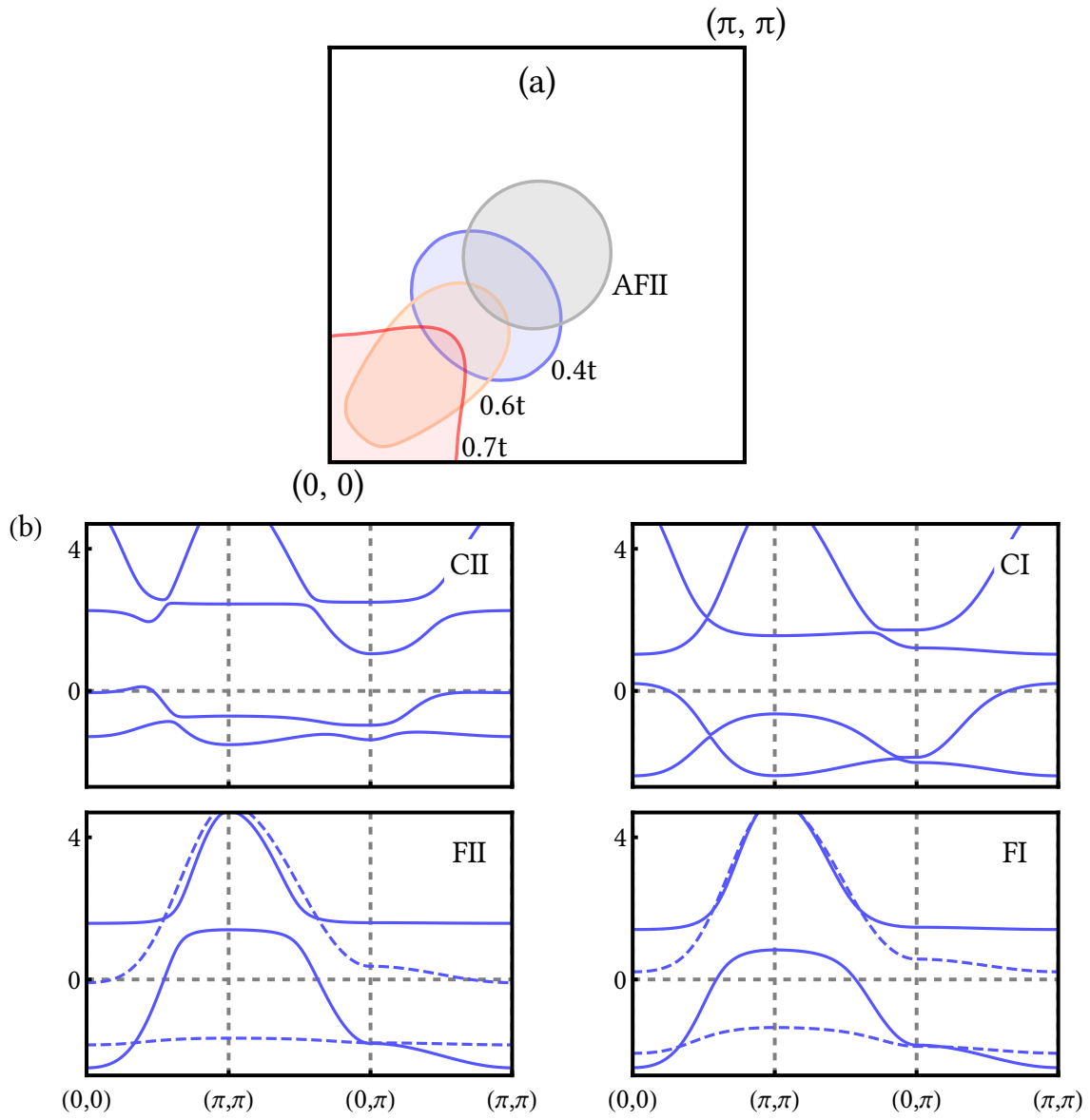

Figure 4.11: The different phases for $t' = -0.4t$ and $B = 0.2t$.

(a) The CII-CI transition, analogous to Fig. 4.7 (a), with $n_c = 0.9$ constant and varying J.

(b) Band structures for each of the possible phases. CII and CI have $n_c = 0.9$ and $J = 0.5t, 1.1t$ respectively. FII and FI have $n_c = 0.74$ and $J = 0.34t, 0.6t$ respectively.

Kondo lattice model, or is caused by some other effect. The case for the heavy fermion transition can be made by comparing the critical field to other quantities relevant for Kondo screening: for example, the critical field B_c seems to be proportional to $T_\chi^{\max}$, the temperature at which the zero-field susceptibility is maximal and which can be interpreted as the onset of heavy fermion behavior [6].

However, this is controversial even for $CeRu_2Si_2$, which has the most well-studied the most well-studied metamagnetic transition [41]. While de Haas-van Alphen experiments indicate a strong discontinuous change in the band structure [7] (implying a similar large-small Fermi surface transition as $CeRh_{1-x}Co_xIn_5$ discussed in chapter 3), some other features are missing that would be expected from f-electron localization. For example, magnetoresistance measurements by Daou et al. [28, 96] show no sign of a strong modification in either the longitudinal or the Hall resistance at the transition; a modification of the Hall resistance would be expected based on our calculation, as a large number of electron-like (negatively charged) charge carriers are introduced for $B > B_c$. The alternate mechanism put forth by Daou et al. is that the real metamagnetic transition corresponds not to the transition at B_c, but instead to the transition to the saturated band at B_s (which we are unable to resolve). However, it is not clear how this could explain the step in the magnetization. Since other heavy fermion compounds (such as CeTiGe [30]) have metamagnetic transitions that fit more closely with the screening breakdown scenario, it seems questionable whether there is a single underlying reason for heavy fermion metamagnetism, again illustrating the limited applicability of model calculations such as ours.

The softening of the antiferromagnetic transition by a magnetic field is an interesting possibility, but we expect that this would require significant effort to investigate experimentally. In the case of $CeRh_{1-x}Co_xIn_5$, the strongest candidate for a Fermi surface quantum phase transition, the response to high magnetic fields has only been investigated for the pure compounds (see Ref. [49] and the references therein). Establishing the effect of a magnetic field on the f-localization transition requires measurements at intermediate x. Further, it is unclear whether the mechanism behind the softening described here (a "wandering" of the Fermi surface due to the breaking of spin-flip symmetry) is possible in systems with more realistic band structures.

5 Implementation for the triangular lattice

In this chapter, we will study the Kondo lattice model on a triangular lattice. This brings with it the complication of *geometric frustration*, as the triangular lattice is not bipartite: while the Kondo lattice usually tends to order (close to) antiferromagnetically, a straightforward collinear ordering is unlikely in this case. The two most natural ways to resolve the frustration are pictured in Fig. 5.1 (a). The first is a three-sublattice antiferromagnetic order, where the magnetic moments form an angle of 120° with respect to each other. This type of ground state is realized in both classical and quantum Heisenberg antiferromagnets on triangular lattices [16, 17, 21].

A more interesting possibility, which is not available in a pure spin model, is that of *partial Kondo screening* [11, 66, 67, 86, 113]. Here, magnetic moments are formed only on a subset of sites, while the remaining ones are in singulet (screened) states. Specifically for the triangular lattice, if one third of the sites are non-magnetic, the other sites can form a honeycomb lattice which allows for standard two-sublattice Néel order.

Experimentally, there is some support for partial screening. For some geometrically frustrated heavy fermion compounds (such as UNi_4B [78, 82, 90], CePdAl [54, 71], or $Ce_5Ni_2Si_3$ [70]) experiments indicate that part of the Ce- or U-ions remain paramagnetic even in magnetically ordered phases, consistent with the notion of partial Kondo screening.

5.1 Implementation

We here implement the bond fermion method in the "ad-hoc" form that ignores the hard-core constraint (see Sec. 2.5.3). Three kinds of magnetic ordering are considered: the above-mentioned 120° antiferromagnetic (AF) and partially Kondo screened (PKS) phases, as well as ferromagnetic (F) order. The first two break the translational symmetry of the model; we will implement them using the three sublattices in Fig. 5.1 (a).

Using the basis vectors $\hat{e}_1 = (1, 0)$ and $\hat{e}_2 = (1, \sqrt{3})/2$ (the lattice spacing is set to unity), the nearest neighbors of a site $\mathbf{R}$ are given by $\mathbf{R} \pm \hat{e}_1$, $\mathbf{R} \pm \hat{e}_2$, and $\mathbf{R} \pm (\hat{e}_2 - \hat{e}_1)$. The hopping Hamiltonian is then

$$H_t = -t \sum_{\mathbf{R}} \left[c^\dagger_{\mathbf{R}} c_{\mathbf{R}+\hat{e}_1} + c^\dagger_{\mathbf{R}} c_{\mathbf{R}+\hat{e}_2} + c^\dagger_{\mathbf{R}} c_{\mathbf{R}+\hat{e}_2-\hat{e}_1} + \text{h.c.} \right]. \tag{5.1}$$

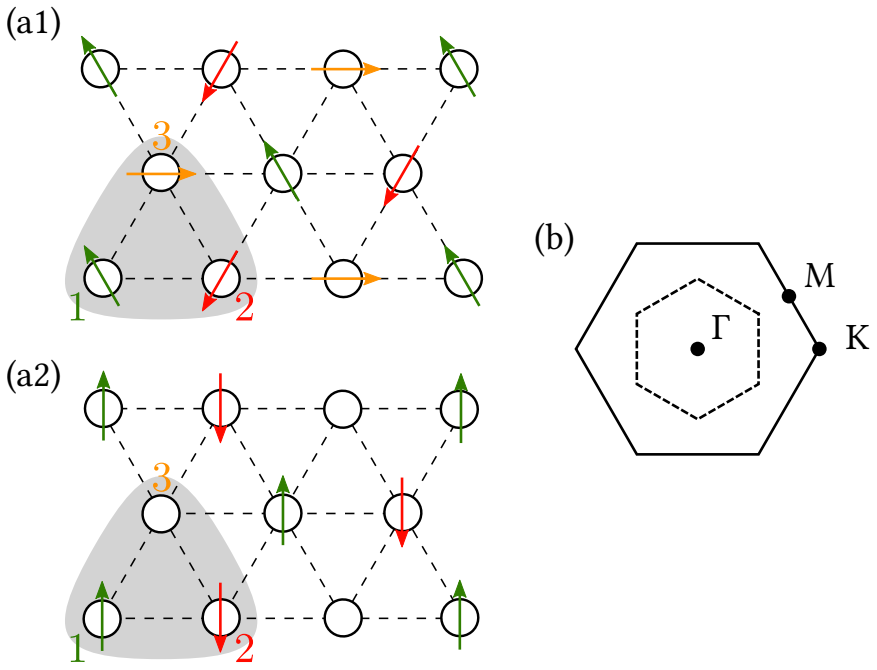

Figure 5.1:

(a) Schematic view of the net magnetic moments in the (a1) 120° Néel and (a2) partial Kondo screening phases. The colored numbers indicate the sublattice index, atoms with same-colored arrows belong to the same sublattice. The atoms underlaid in gray form a single unit cell of the ordered system. Note that sublattice 3 does not carry a net magnetic moment in the partial Kondo screening phase.

(b) The original (full line) and antiferromagnetic (dashed line) Brillouin zones of the triangular lattice. Γ, M, and K are symmetry points. $\mathbf{k}$-sums are constrained to the antiferromagnetic Brillouin zone.

We now split the lattice into the three sublattices, indexed by $\mathrm{I} \in \{1, 2, 3\}$, and Fourier transform each sublattice individually:

$$\mathfrak{c}^\dagger_{\mathbf{k}\mathrm{I}} = \sum_{\mathbf{R}\in S_\mathrm{I}} e^{i\mathbf{k}\mathbf{R}} c^\dagger_{\mathbf{R}}, \tag{5.2}$$

$$c^\dagger_{\mathbf{R}} = \sum_{\mathbf{k}} e^{-i\mathbf{k}\mathbf{R}} \mathfrak{c}^\dagger_{\mathbf{k}\mathrm{I}} \quad \text{if} \quad \mathbf{R} \in S_\mathrm{I}. \tag{5.3}$$

S_I is the set of sites included in sublattice I, and $\mathfrak{c}$ the "decomposed" electron operator. The momentum sum goes over a smaller Brillouin zone (Fig. 5.1 (b)).

Using this, (5.1) can be rewritten as (first split the sum using $\sum_{\mathbf{R}} = \sum_{\mathrm{I}\in\{1,2,3\}} \sum_{\mathbf{R}\in S_\mathrm{I}}$, then apply (5.3); note that if e.g. $\mathbf{R} \in S_1$, then $\mathbf{R} + \hat{e}_1 \in S_2$, etc.)

$$H_t = \sum_{\mathbf{k}} \mathfrak{c}_{\mathbf{k}}^\dagger \epsilon_{\mathbf{k}} \mathfrak{c}_{\mathbf{k}}, \tag{5.4}$$

$$\epsilon_{\mathbf{k}} = \begin{pmatrix} 0 & f_{\mathbf{k}} & f_{\mathbf{k}}^* \\ f_{\mathbf{k}}^* & 0 & f_{\mathbf{k}} \\ f_{\mathbf{k}} & f_{\mathbf{k}}^* & 0 \end{pmatrix}, \tag{5.5}$$

$$f_{\mathbf{k}} = -te^{ik_x} - 2te^{-ik_x/2} \cos\left(\frac{\sqrt{3}}{2} k_y\right). \tag{5.6}$$

$\mathfrak{c}_{\mathbf{k}}^\dagger$ contains the $\mathfrak{c}_{\mathbf{k}\mathrm{I}}^\dagger$ (since each $\mathfrak{c}_{\mathbf{k}\mathrm{I}}^\dagger$ also carries a spin index, $\mathfrak{c}_{\mathbf{k}}^\dagger$ has in total six components). $\epsilon_{\mathbf{k}}$ is the kinetic energy matrix. Note that $f_{\mathbf{k}} \to f_{\mathbf{k}}^*$ when $\mathbf{k}$ is rotated by $\frac{\pi}{3}$, reflecting the symmetry of the triangular lattice.

As explained in Sec. 2.5.3, we need to enforce some constraints on the local expectation values to avoid physically unreasonable occupation numbers. For simplicity, we use only the "averaged" constraint (2.134–2.136), from which we get

$$N_e = \sum_{\mathbf{R}} \left[1 - \langle a_{\mathbf{R}}^\dagger a_{\mathbf{R}} \rangle + \langle b_{\mathbf{R}}^\dagger b_{\mathbf{R}} \rangle \right] \tag{5.7}$$

$$= \sum_{\mathbf{R}} \left[\langle a_{\mathbf{R}} a_{\mathbf{R}}^\dagger \rangle + \langle b_{\mathbf{R}}^\dagger b_{\mathbf{R}} \rangle - 1 \right] \tag{5.8}$$

$$= \sum_{\mathbf{k}} \left[\langle \mathfrak{a}_{\mathbf{k}} \mathfrak{a}_{\mathbf{R}}^\dagger \rangle + \langle \mathfrak{b}_{\mathbf{k}}^\dagger \mathfrak{b}_{\mathbf{k}} \rangle - 3 \right]. \tag{5.9}$$

In (5.8) we used that $\langle a_{\mathbf{R}}^\dagger a_{\mathbf{R}} \rangle = 2 - \langle a_{\mathbf{R}} a_{\mathbf{R}}^\dagger \rangle$ (the 2 arises from the implicit spin sum). For (5.9) we introduced $\mathfrak{a}$ and $\mathfrak{b}$ which decompose a and b into sublattices analogously to $\mathfrak{c}$ did before (the 3 arises because the momentum sum is restricted to the magnetic Brillouin zone, i.e. $\sum_{\mathbf{k}} 1 = N/3$).

We can also calculate

$$N_e' = \sum_{\mathbf{R}} \langle v_{\mathbf{R}}^\dagger W_{\mathbf{R}}^\dagger W_{\mathbf{R}} v_{\mathbf{R}} \rangle. \tag{5.10}$$

$W_{\mathbf{R}}$ is constant on each sublattice, meaning $W_{\mathbf{R}} = \text{const.} = W_\mathrm{I}$ if $\mathbf{R} \in S_\mathrm{I}$, for W_I still defined according to (2.179). Introducing $\mathfrak{v}$ analogously to before, we then rewrite N_e' as

$$N_e' = \sum_{\mathbf{k}} \langle \mathfrak{v}_{\mathbf{k}}^\dagger W^\dagger W \mathfrak{v}_{\mathbf{k}} \rangle, \tag{5.11}$$

$$W = \begin{pmatrix} W_1 & 0 & 0 \\ 0 & W_2 & 0 \\ 0 & 0 & W_3 \end{pmatrix}, \tag{5.12}$$

where we also introduced the "combined" transformation matrix W. Since $\mathfrak{v}$ contains a set of four bond fermions for each sublattice, $\mathfrak{v}_{\mathbf{k}}$ has a total of twelve components. Similarly, W is a 6×12 matrix, as each W_I is 2×4. The physicality condition reads $N_e = N_e'$.

Putting these things together, the energy expectation value (2.32) is minimized by the ground state of the effective Hamiltonian

$$H_{\text{eff}} = \sum_{\mathbf{k}} \mathfrak{v}_{\mathbf{k}}^{\dagger} \left[h + W^{\dagger}(\epsilon_{\mathbf{k}} - \lambda) W \right] \mathfrak{v}_{\mathbf{k}}, \tag{5.13}$$

$$h = \begin{pmatrix} h_1 & 0 & 0 \\ 0 & h_2 & 0 \\ 0 & 0 & h_3 \end{pmatrix}, \tag{5.14}$$

$$h_{\text{I}} = e_{\text{I}} \operatorname{diag}(-1, -1, 1, 1) - \mu \operatorname{diag}(1, 1, 1, 1). \tag{5.15}$$

The chemical potential μ and the additional Lagrange multiplier λ respectively correspond to the "electron numbers" N_e and N_e', allowing us to tune N_e to its correct value and enforce $N_e = N_e'$.

The explicit forms of $s_{\mathbf{R}}$ and $\mathbf{t}_{\mathbf{R}}$ we use are

$$\text{AF} \qquad s_{\text{I}} = \cos(\Theta), \qquad \mathbf{t}_{\text{I}} = \sin(\Theta) \begin{pmatrix} \cos\left(\frac{2\pi}{3}\text{I}\right) \\ \sin\left(\frac{2\pi}{3}\text{I}\right) \\ 0 \end{pmatrix}, \tag{5.16}$$

$$\text{PKS} \qquad s_1 = s_2 = \cos(\Theta), \qquad \mathbf{t}_1 = -\mathbf{t}_2 = \sin(\Theta)\hat{e}_z,$$

$$s_3 = 1, \qquad \mathbf{t}_3 = 0, \tag{5.17}$$

$$\text{F} \qquad s_{\text{I}} = \cos(\Theta), \qquad \mathbf{t}_{\text{I}} = \sin(\Theta)\hat{e}_z. \tag{5.18}$$

In all three cases, the angle Θ controls the degree of triplet (magnetic) admixture in $|\Omega\rangle$ (with $|\mathbf{t}_{\mathbf{R}}| = \sin(\Theta)$ on magnetic sites). Paramagnetism corresponds to $\Theta = 0$. For magnetic sites the exchange energy is given by $e_{\text{I}} = J/4\,(1 + 2\cos(2\Theta))$.

The phase diagram is found by minimizing the energy over the range $0 \leq \Theta \leq \pi/3 = 1.05$ for each type of magnetic order. The reason for the specific upper bound is that the "ad-hoc" method of dealing with the hard-core constraint becomes inapplicable for $\pi/3 < \Theta$. In this region, the bond fermion energy of formation e_{I} is negative. Consequently, it is energetically favourable to create as many bond fermions as possible and due to the pair creation terms $\propto a^{\dagger}_{\mathbf{R}\sigma} b^{\dagger}_{\mathbf{R}'\sigma'}$, the system is filled with fermions (in a Gutzwiller calculation, this would be prevented by a large blocking term m). The "ground states" in the region $\Theta > \pi/3$ usually have bond fermion densities ρ_{BF} of 2 to 3 per site, which makes little sense in view of the hard core constraint. For a similar reason, we also restricted our calculation to $J > 1.3t$; as seen in the analytic calculation (Sec. 2.6), for very small J one would find unphysically large ρ_{BF} no matter $\mathbf{t}_{\mathbf{R}}$. This keeps the bond fermion density at an acceptable level ($\rho_{\text{BF}} \lesssim 0.8$, with the probability for a constraint violation always below 20%).

To implement the variational optimization, we use a similar structure of nested loops as in Sec. 3.1, although this is much simplified because of the "ad-hoc" approximation. One does not have to solve for the matrices $\sqrt{Z}$, m, or Λ: instead, one can use a simple one-dimensional root finding procedure to adjust λ so that $N_e = N_e'$. This is also a reason for why we have not used more of the symmetries of our different magnetic states: in the Gutzwiller approximation, we could reduce the number of independent parameters to solve for this way, but in the "ad-hoc" method this is not really worth the effort. The effective temperature was set to $T = 0.0025t$ in this calculation.

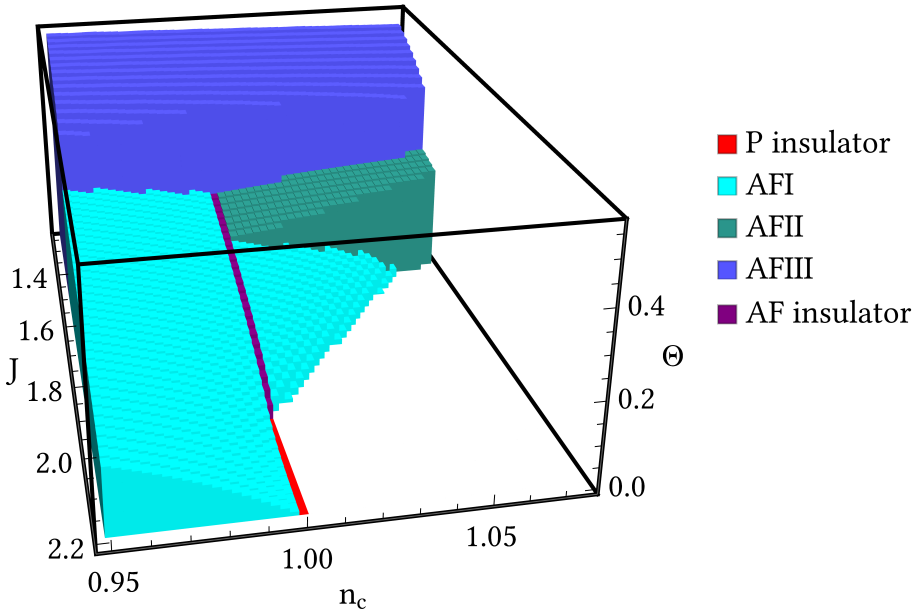

Figure 5.2: The phase diagram when considering only paramagnetic and antiferromagnetic phases. Colors denote different phases; the z-axis shows the optimal angle Θ.

5.2 120° antiferromagnetic phases

For the sake of clarity we first present the results with only AF order taken into account. We find four qualitatively different phases, depicted in Fig. 5.2. For example, if we were to start with a large J and then reduce it while holding $n_c > 1$ constant (note that since the triangular lattice is not bipartite, there is no particle-hole symmetry and the behavior for $n_c < 1$ is qualitatively different), we would first encounter a second-order transition from the paramagnetic phase to the ordered AFI phase (with finite Θ), followed by two successive first-order transitions to the AFII and AFIII phases, respectively. While the symmetry of all three ordered phases is the same, they are (as in the previous chapters) distinguished by their band structures and Fermi surfaces (Fig. 5.3).

AFI and AFII have $\Theta < 0.35$ and are analogous to the antiferromagnetic phases of the square lattice. The AFI Fermi surface is almost the same as what would be found by a paramagnetic calculation, consisting of a pocket at the Γ point (more precisely: two slightly acircular pockets rotated 60° relative to each other), and its antiferromagnetic copies around the Brillouin zone edges. The interpretation is analogous to the square lattice as well: the quasiparticles have a large (band) mass, so that the system is strongly correlated. Meanwhile, for the AFII phase, the Fermi surface is more similar to the free Fermi surface, so that the system is weakly correlated.

The quasiparticle band structures in both AFI and AFII are gapped. Approaching half-filling from above, the jump in Θ at the AFI-AFII transition vanishes continuously, and no transition between them occurs for $n_c \leq 1$. The reason is that the difference in behavior of AFI and AFII is caused by a slight shift of the minima of the lowest band above the gap (from Γ and K for AFI to M and halfway between Γ and K for AFII) whereas the topmost

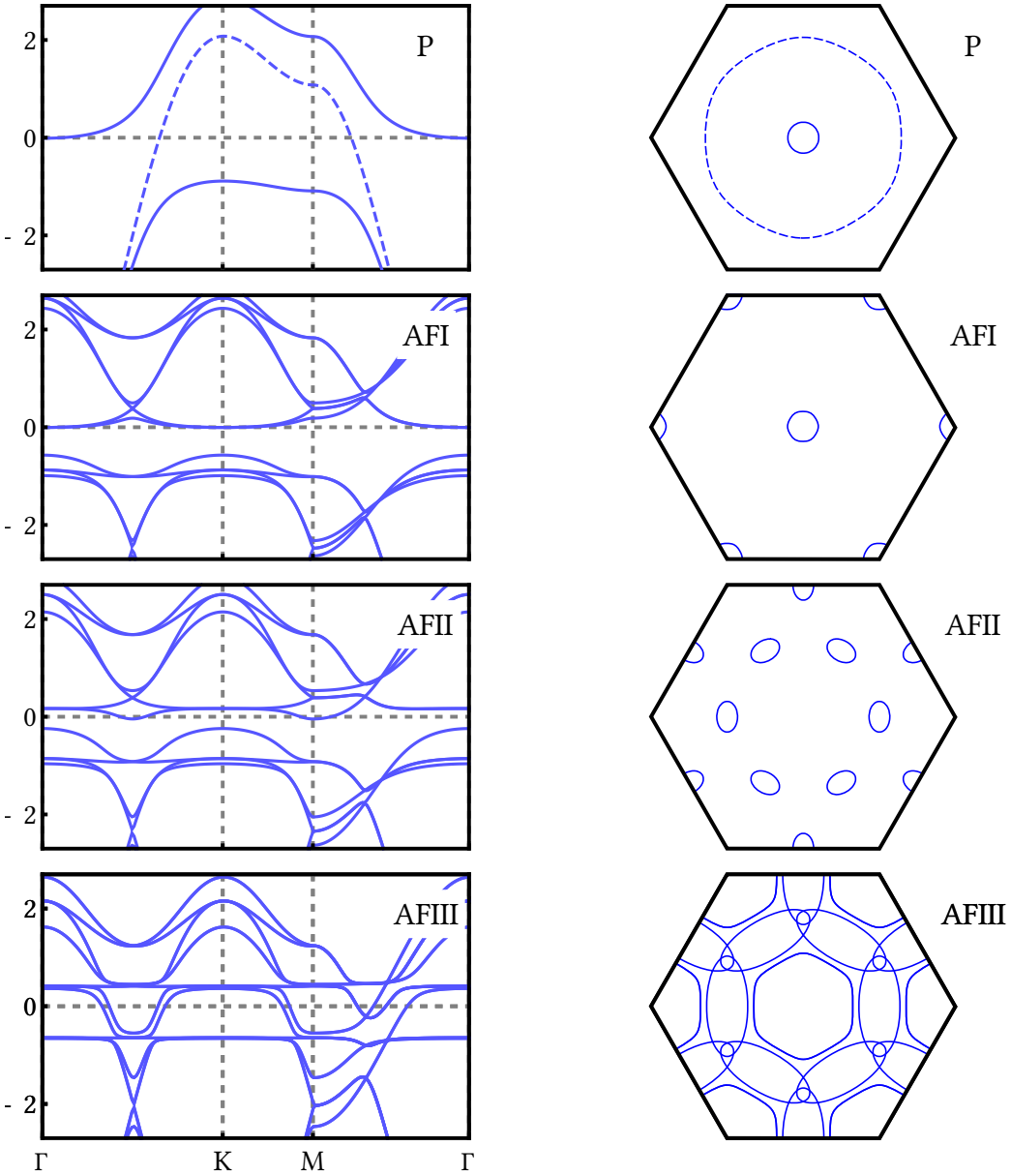

Figure 5.3: Band structures for the paramagnetic and antiferromagnetic phases on a path through the symmetry points of the large Brillouin zone, with the corresponding Fermi surfaces ($n_c = 1.025$). From top to bottom, we have $J = 1.83t$ (P, the dashed line is the free band structure), $J = 1.63t$ (AFI), $J = 1.51t$ (AFII), and $J = 1.25t$ (AFIII). Note the similarity between P and AFI Fermi surfaces, whereas AFII and AFIII are more similar to the free Fermi surface.

band below the gap has has the same appearance in both cases. This means that below half-filling, when the Fermi surface cuts into the band below the gap, the phases coalesce.

AFIII covers the region of $J \lesssim 1.45t$ and all electron densities considered. The optimal angle is large, $\Theta \sim 0.5$. As a consequence of this, the hybridization between localized and itinerant bands is rather weak: (2.179) shows that $W_{\mathbf{R}}$ is formed from two 2×2 matrices, which respectively have determinants $s_{\mathbf{R}}^2 - \mathbf{t}_{\mathbf{R}}^2$ and its complex conjugate. These matrices become singular for $\Theta = \pi/4 = 0.79$, at which point flat and itinerant bands decouple. One is left with two effectively independent systems: one set of bands that mimics the band structure of a mean-field calculation, where the interaction with the localized spins is replaced by a sublattice-dependent Zeeman term, and one set of perfectly flat bands above and below the Fermi energy. This is most easily shown in the simpler case of a system fixed ferromagnetic polarization. Specifically, if we were to set $s_{\mathbf{R}} = 1/\sqrt{2}$ and $\mathbf{t}_{\mathbf{R}} = \hat{e}_z/\sqrt{2}$, (2.28–2.30) would result in

$$W_{\mathbf{R}} = \begin{pmatrix} 0 & 1 & 0 & 0 \\ 0 & 0 & 0 & -1 \end{pmatrix}, \tag{5.19}$$

$$\langle c^\dagger_{\mathbf{R}\uparrow} c_{\mathbf{R}'\uparrow} \rangle = \langle a_{\mathbf{R}\downarrow} a^\dagger_{\mathbf{R}'\downarrow} \rangle, \tag{5.20}$$

$$\langle c^\dagger_{\mathbf{R}\downarrow} c_{\mathbf{R}'\downarrow} \rangle = \langle b^\dagger_{\mathbf{R}\downarrow} b_{\mathbf{R}'\downarrow} \rangle. \tag{5.21}$$

Thus, only spin-down bond fermions take part in hopping processes (forming the itinerant bands), while the others are completely localized (forming the flat bands).

The current situation is slightly more complicated as $\mathbf{t}_{\mathbf{R}}$ depends on the site, but is analogous[1]. The AFIII phase has a Θ close enough to $\pi/4$ that the residual hybridization can be ignored for a qualitative description of the dynamics near the Fermi energy (see again Fig. 5.3): the Fermi surface is the result of folding the non-interacting electron bands to the antiferromagnetic Brillouin zone (AFBZ) and hybridizing them. Accordingly, this phase remains conducting even at half-filling, in contrast to the other magnetic phases.

For $n_c = 1$, the Fermi energy is located inside the gap and the system becomes insulating. Our calculation predicts a critical value of $J = 1.96t$ for the formation of magnetic moments, and $J = 1.45t$ for the transition to the metallic AFIII phase. In the case of $n_c < 1$, Θ vanishes much more slowly and magnetic order survives to larger J: the "combined" AFI/AFII phase (which we refer to as AFI because its Fermi surface is the same as AFI phase at $n_c > 1$) extends up to $J \sim 4t$ (not pictured).

5.3 Partial Kondo screening

We now repeat the above calculation, but for PKS type order. Phases of this type may be favored over AF order in easy-axis anisotropic systems, where noncollinear order is suppressed. On the other hand, since the PKS phase's sublattices cannot all be related by symmetry transformations, they will have a charge disproportionation and a higher

[1] For the simplest demonstration, perform a site-dependent rotation so that $\mathbf{t} \propto \hat{e}_z$ everywhere. (5.19) then applies, implying that two bond fermion modes are decoupled (at the cost of introducing spin-dependent hopping amplitudes).

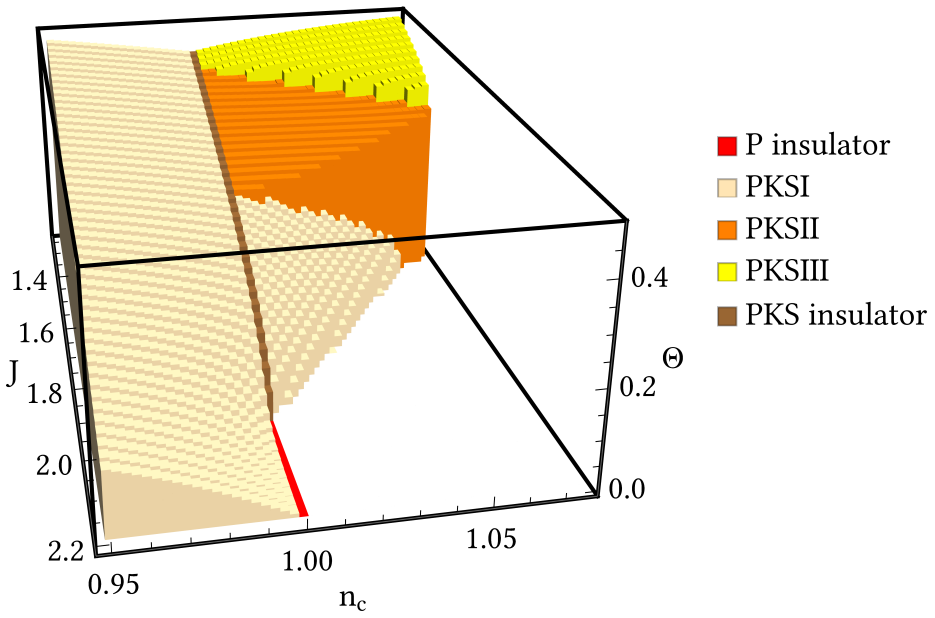

Figure 5.4: Same as Fig. 5.2, but for PKS order.

Coulomb energy that is unaccounted for in the Kondo lattice model. As was the case for the AF phase, we find three different ordered phases (Fig. 5.4), PKSI through PKSIII, which are reached for $n_c > 1$ by lowering J. Somewhat surprisingly, the critical value of the interaction at half-filling is unchanged at $J = 1.96t$.

The band structures of the PKS phases are shown in Fig. 5.5. A significant difference between these and the AF phases is the different band degeneracy, which is caused by a nonobvious symmetry. For the PKS phases, spatial parity inversion ($\mathcal{P}$) about a non-magnetic lattice site exchanges the two magnetic sublattices (compare Fig. 5.1 (a) bottom). The original state of the lattice can then be restored by flipping the magnetic moments through time reversal ($\mathcal{T}$), so that a $\mathcal{PT}$ operation is a remaining (antiunitary) symmetry of the ordered system. When acting with $\mathcal{PT}$ on a Bloch state $\propto e^{i\mathbf{kR}}$, each of $\mathcal{P}$ and $\mathcal{T}$ involve exchanging $\mathbf{k} \to -\mathbf{k}$, so that the crystal momentum remains unchanged. However, $\mathcal{T}$ does not commute with S_z, the bond fermion spin in z-direction, which is conserved as the system is spin rotation invariant about the z-axis. Accordingly, for every $\mathbf{k}$, we must have degenerate states that can be distinguished by their spin direction. In contrast, $\mathcal{P}$ is not a symmetry operation for the AF phases (compare Fig. 5.1) which explains why the bands in these phases are non-degenerate.

PKSI and PKSII are qualitatively very similar to AFI and AFII respectively. Fermi pockets are found in the same spots as before. Note the relative decrease in area of the Fermi pockets between AFII and PKSII, which is a consequence of the absence of spin degeneracy in the AF phases: since for PKSII each band in a pocket can accomodate two electrons instead of one, their sizes must be halved for the total fermion number to stay the same. This is not the case for AFI and PKSI because (as mentioned earlier) the pocket for AFI actually consists of two slightly different and rotated pockets.

PKSIII does not have an AF analogue. Unlike AFIII, the band structure is gapped and becomes insulating when approaching $n_c = 1$. In fact, it is most similar to AFII and PKSII:

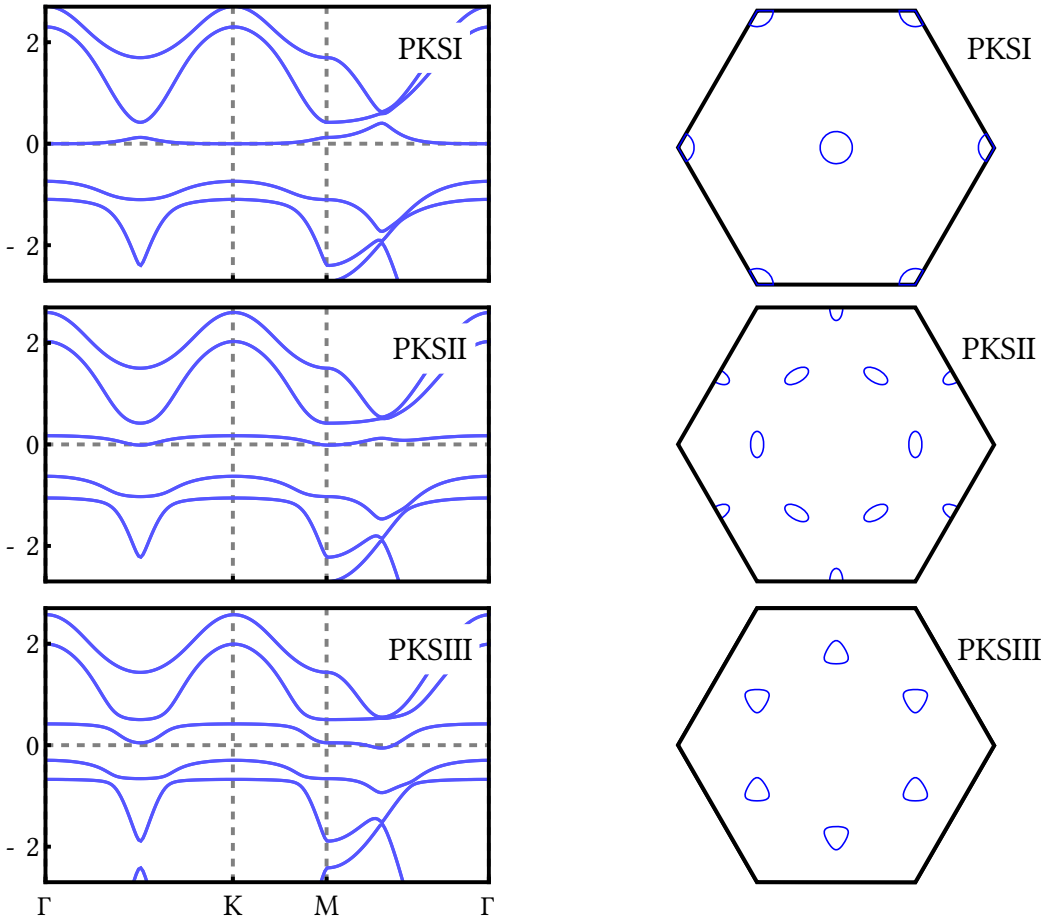

Figure 5.5: Same as Fig. 5.3, but for the PKS phases. Interactions are $J = 1.63t$ (PKSI), $J = 1.51t$ (PKSII), and $J = 1.25t$ (PKSIII).

while the Fermi surfaces of these phases consist of pockets along the *edges* of the small BZ, they are now placed at the *corners*. The bands below the gap are still unaffected, so that no transition between PKS phases is found at all for $n_c < 1$ and PKSI extends to lower J.

Fig. 5.6 summarizes some physical properties at half-filling, namely the angle Θ in (5.16), the charge disproportionation $n_3 - n_c$ between magnetic and nonmagnetic sites in the PKS phase, and the probabilities p_I for violation of the hard-core constraint on sublattice I. The critical values are $J = 1.96t$ for P to PKS and $J = 1.38t$ for PKS to AF (see section 5.4). Note that $\Theta = 0$ for the paramagnetic phase and $n_3 - n_c \neq 0$ only for the PKS phase, whereas $p_3 = p_{1,2}$ for the paramagnetic and AFIII phases. Θ shows square-root behavior directly below the PKS transition, while $n_3 - n_c$ is linear. In addition, $p_\mathrm{I} < 0.16$ in the whole range of the plot (somewhat justifying the applicability of the "ad-hoc" method). In the PKS phase there is a sizable charge disproportionation $n_3 - n_c$: n_3, the electron density on the third (nonmagnetic) sublattice is found to be significantly higher (in excess of 10% for some parameter regions) than on the other (magnetic) sublattices. On-site Coulomb repulsion will thus be a significant obstacle to PKS phases in more realistic systems.

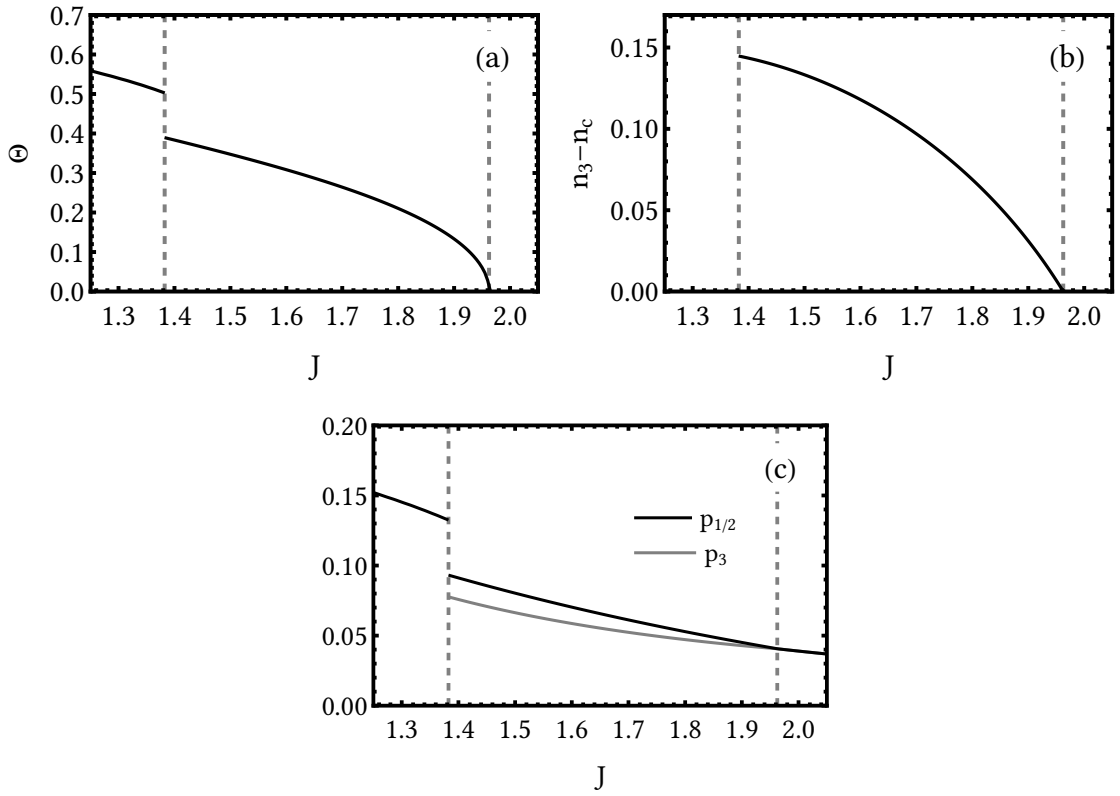

Figure 5.6: Details of the system at half-filling. The dashed lines indicate the position of the AFIII-PKS and the PKS-P transitions.

(a) Order parameter Θ.

(b) Charge disproportionation $n_3 - n_c$ (where n_3 is the conduction electron density on sublattice $I = 3$). $n_3 - n_c$ is only finite in the PKS phase.

(c) Probability of a constraint violation on the different sublattices. Outside the PKS phase, all sites are equivalent ($p_1 = p_2 = p_3$), whereas in the PKS phase the violation probability is higher on the magnetic sublattices ($p_{1/2} \neq p_3$).

5.4 Full phase diagram

We now consider all phases simultaneously, resulting in the combined phase diagram in Figures 5.7 and 5.8. A large part of the PKS region is replaced by AF phases: in particular, PKSIII is completely covered by AFIII. However, PKS is still found in a kite-shaped region around the (insulating) line of $n_c = 1$ and $1.37t < J < 1.96t$ and a disconnected region for $n_c < 1$ and $J \approx 3.2t$.

The P metal is replaced by a weakly ferromagnetic phase up to $J \sim 5t$. Its properties are quite similar to those of ferromagnetic phase on the square lattice. The magnetic moment is again comparatively small, with the angle $\Theta < 0.05$, and the the Fermi surface is completely polarized, see Fig. 5.9. Accordingly, the area of each Fermi pocket must be doubled

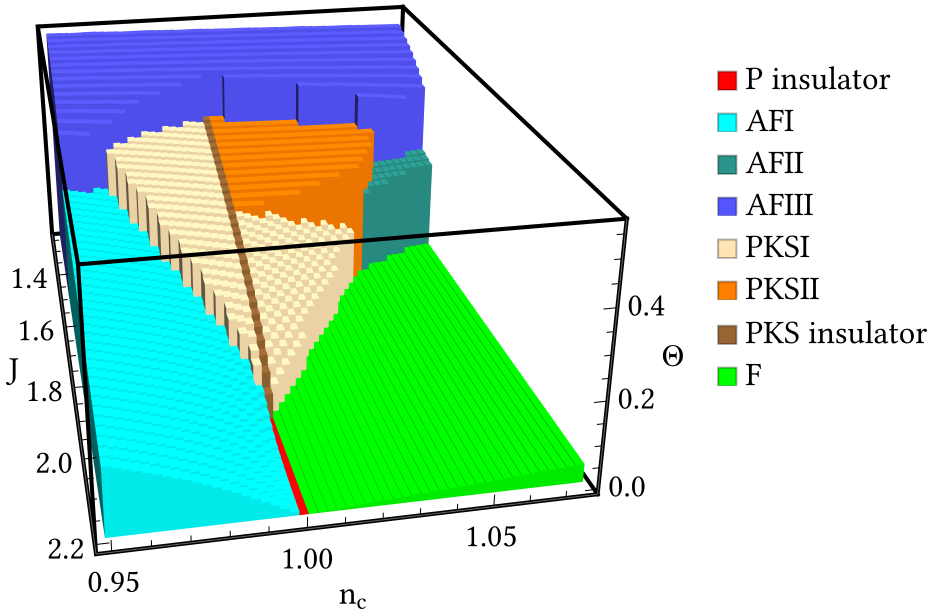

Figure 5.7: Same as Figs. 5.2 and 5.4, but with all kinds of magnetic order included.

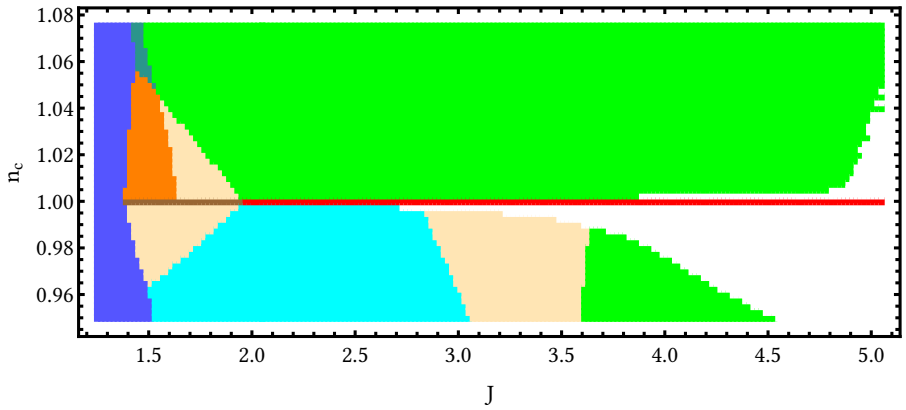

Figure 5.8: Extended vertical view of Fig. 5.7.

compared to the paramagnetic phase. The order parameter vanishes continuously when approaching half-filling, so that no insulating ferromagnetic phase is observed.

5.5 Summary and discussion

In summary we have studied the phase diagram of the Kondo lattice model on a two-dimensional triangular lattice with the "ad-hoc" method, which brings about the additional complication of geometrical frustration. We investigated two ways for the ordered moment to circumvent the frustration, three-sublattice Néel order which is realized in Heisenberg antiferromagnets, and partial Kondo screening where magnetic moments are formed only on a subset of sites which form a honeycomb lattice. Our calculations indicate that both types of magnetic order become stable for smaller J and that they are in

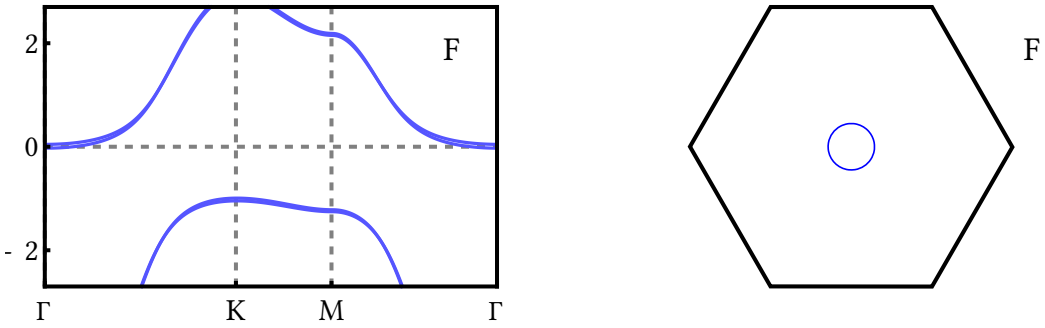

Figure 5.9: Same as Figures 5.3 and 5.5, but for the F phase ($J = 2.01t$). Note the slight band splitting, which results in an enlarged Fermi pocket when compared to the paramagnetic phase.

fact energetically very close to each other. For example, at half-filling the critical value of J_c where magnetic order sets in is practically the same for AF and PKS. As was the case for the two-dimensional square lattice, the antiferromagnetic phases themselves actually consist of several phases which differ in their Fermi surface topology. For larger $J < J_c$ and for both types of magnetic order the band structure and Fermi surface may be obtained by backfolding the paramagnetic band structure, so that one has Fermi pockets formed by the heavy part of the paramagnetic band. Accordingly, the phase transition from paramagnetic to antiferromagnetic is of second order. Upon further reducing J there is a first-order transition to a phase whose band structure and Fermi surface are consistent with that of the mere conduction band under the influence of decoupled magnetic moments.

We will now try to relate our results to previous works on PKS in the triangular lattice. While some studies have focused on chiral-type magnetic order and treated the localized moments classically [3, 4, 75], Motome et al. investigated PKS at half-filling using variational Monte Carlo (VMC) [81]. In contrast to our calculation, they do not find any indication that a PKS state exists for $n_c = 1$, unless it is stabilized by an Ising-like interaction between the localized moments. While VMC should in principle yield more accurate results than bond fermion theory, one has to keep in mind that the precision of VMC is limited by its restriction to considerably smaller finite systems. The energy differences we find between the different phases are typically very small (the bond fermion theory predicts a maximum relative difference of 2% across the whole parameter region under consideration), while Motome et al. estimate a relative accuracy of 3% for their calculation.

PKS has also been investigated in the context of the periodic Anderson model on a triangular lattice. In the mean-field approximation, Hayami et al. [43, 44] found a phase diagram qualitatively similar to ours for $U = 2t$ [44]. Keeping in mind that we restrict ourselves to homogeneous phases and are thus unable to reproduce the phase separated regions discussed by Hayami et al., both calculations predict the same phases at half-filling: paramagnetic Kondo insulator for large J, antiferromagnetic metal for small J, and PKS in an intermediate region. Additionally, their phase diagram shows a similar tendency towards AF (F) order below (above) half-filling. However, the numerical values

of J at the phase transitions seem to be considerably higher than in our calculation: if we estimate J as $8V^2/U$ (noting that this may be somewhat inaccurate in the present parameter region), phase transitions take place between around $3t$ and $6t$. At larger U, the PKS phase is replaced first by a collinear "up-up-down" (UUD) antiferromagnetic phase and then by an insulating 120° AF state [43]. While we did not investigate UUD order, an insulating AF phase at intermediate coupling qualitatively matches our results with PKS disregarded.

Aulbach et al. [10] considered the same problem using DMFT. These authors took into account UUD, PKS, and ferromagnetic phases whereas antiferromagnetic 120° order was disregarded. They found magnetic order at less than half-filling (corresponding to $n_c > 1$ as they chose the opposite sign for the kinetic energy). There, ordered phases are found in two disconnected parameter regions, one with PKS that gives way to UUD order upon lowering J, and, at even further reduced electron densities, one displaying ferromagnetism. In particular, no PKS insulator is found. We have so far been unable to explain this stark contrast to our results (where magnetically ordered phases are favored compared to paramagnetism in much larger regions of parameter space).

Additionally, there is theoretical evidence for PKS at other commensurate fillings [45, 85]. We cannot expect our approximations to give reliable results so far away from half-filling. For example, Noda et al. predict a PKS state and a metal-insulator transition for $n_c = 2/3$, which in our formulation of the bond fermion theory would consists of a state with 5 filled bands. However, the band degeneracy in the PKS makes such a transition impossible, as insulating phases can only exist for an even number of filled bands. To replicate the behavior found by Noda et al. would thus seem to require a significantly different (and more complicated) ansatz for a bond particle theory, perhaps one where entanglement between different sites in a unit cell is already included in the definition of $|\Omega\rangle$ and the bond fermions.

As demonstrated, there is considerable variance in literature results. From this aspect, it is thus quite difficult to evaluate the performance of the bond fermion calculation in general, and the "ad-hoc" method in particular. We expect that a Gutzwiller approximation as in the previous chapters would lead to broadly similar results, but with the antiferromagnetic transitions shifted to smaller J (analogous to the results for the square lattice). However, due to the aforementioned small energy differences, more substantial changes cannot be ruled out without a complete calculation (an avenue for future work). Especially the fate of the AFIII phase is unclear: it may be that the larger gap in a Gutzwiller approximation destroys (part of) this conducting phase.

Regarding the ferromagnetic phase near half-filling, we find its presence in the triangular lattice rather more justified than for the square lattice. Ferromagnetism is the simplest type of magnetic ordering that does not suffer from frustration, and the results of Hayami et al. are concurrent in this regard. Still, similar criticism as in the square lattice applies here as well.

6 Conclusion and outlook

In this thesis we have investigated the dynamics of the Kondo lattice model (KLM), a simple yet strongly correlated system that illustrates the interplay between heavy fermion physics and magnetic phenomena. To this end we employed the bond fermion method, wherein the system is described by the strong-coupling ground state "dressed" with effective fermions (which act as the excitations of the theory). A thorough description of both the philosophy and the mathematics of the theory are given in Chapter 2. Departing from the literature, the residual bond fermion interaction is treated more rigorously through the well-known Gutzwiller approximation. We were also able to explain and improve on some of the shortcomings in previous descriptions of the method (in particular regarding the "physicality" of expectation values).

This improved method was then applied to the standard KLM on the square lattice (Chapter 3), where we found both antiferromagnetism and a Lifshitz transition between phases with qualitatively different (either large or small) Fermi surfaces. In addition to general agreement with literature results (and, in some aspects, marked improvements compared to previous bond fermion studies), we also found a novel phenomenon: our calculation suggests a strong narrowing of the conduction band near the Lifshitz transition. The resulting increase in the band mass mirrors the behavior of some heavy fermion compounds, for example $CeRhIn_5$. Somewhat less successful was the inclusion of incommensurate and ferromagnetic order parameters. Incommensurate order was only found in the region of weak interaction, for which a strong-coupling theory like the bond fermion method is an inappropriate tool. However, the resulting phase diagram was still qualitatively reasonable, except for an extended and likely unphysical ferromagnetic phase.

This ferromagnetic phase and the phenomenon of metamagnetism (a phase transition at a large external field, which is ubiquitous in real materials) were investigated more closely in Chapter 4, where we added an out-of-plane magnetic field to the calculation. The nature of the metamagnetic transition was found to be different depending on the interaction strength: at large (small) interaction it is first- (second-) order. The antiferromagnetic phases and the Lifshitz transition between large and small Fermi surfaces are also strongly modified by the magnetic field: whereas before the Lifshitz transition was strongly discontinuous, it now proceeds continuously through intermediate stages whose Fermi surfaces do not fit neatly into the large-small dichotomy.

Finally, in Chapter 5 we calculated the phase diagram of the triangular KLM, which brings with it the complication of geometric frustration. For this we used a more basic form of the bond fermion method, where the bond fermion interaction is mostly disregarded. Special focus was on the phenomenon of partial Kondo screening: due to the frustration, it may be energetically favorable for only a subset of all lattice sites to participate in magnetic ordering. Our calculation predicts that this is indeed the case in a significant region of the phase diagram.

In conclusion, the bond fermion method is a valuable tool to investigate heavy fermion physics in regions where many other approaches struggle (for example mean-field theory, which is suited for weakly interacting systems), and not too difficult to implement. Indeed, the "ad-hoc" version of the method is only slightly more complicated than mean-field theory. It is also easy to adapt to other geometries, or add couplings to external fields (like the magnetic field in this thesis) or degrees of freedom.

However, we can also see many regions that could be improved. The most pressing is a proper treatment of the degrees of freedom ignored by the bond fermion method (specifically, triplet fluctuations). Without this, the experimentally important region of small interaction is difficult to describe. This should also allow for calculations on more realistic models (e.g. ones with local spins greater than 1/2), as at present the method is very reliant on the specifics of the KLM, whose simplicity makes it inherently unable to describe the many complicated and varied phase transitions real systems display.

Bibliography

[1] A. A. Abrikosov. "Electron scattering on magnetic impurities in metals and anomalous resistivity effects". In: *Physics Physique Fizika* 2 (1965), 5–20. DOI: 10/jpc5.

[2] A. A. Abrikosov et al. *Methods of quantum field theory in statistical physics*. New York, NY: Dover, 1975.

[3] Y. Akagi and Y. Motome. "Spin Chirality Ordering and Anomalous Hall Effect in the Ferromagnetic Kondo Lattice Model on a Triangular Lattice". In: *Journal of the Physical Society of Japan* 79 (2010), 083711. DOI: 10.1143/JPSJ.79.083711.

[4] Y. Akagi and Y. Motome. "Ground-state phase diagram of the Kondo lattice model on triangular-to-kagome lattices". In: *Journal of the Korean Physical Society* 63 (2013), 405–408. DOI: 10.3938/jkps.63.405.

[5] P. W. Anderson. "Localized Magnetic States in Metals". In: *Physical Review* 124 (1961), 41–53. DOI: 10.1103/PhysRev.124.41.

[6] D. Aoki, W. Knafo, and I. Sheikin. "Heavy fermions in a high magnetic field". In: *Comptes Rendus Physique* 14 (2013), 53–77. DOI: 10.1016/j.crhy.2012.11.004.

[7] H. Aoki et al. "Transition of f electron nature from itinerant to localized: Metamagnetic transition in $CeRu_2Si_2$ studied via the de Haas–van Alphen effect". In: *Physical Review Letters* 71 (1993), 2110–2113. DOI: 10.1103/PhysRevLett.71.2110.

[8] S. Araki et al. "Fermi surface instability in $CeRh_2Si_2$ under pressure". In: *Physical Review B* 64 (2001), 224417. DOI: 10.1103/PhysRevB.64.224417.

[9] F. F. Assaad. "Quantum Monte Carlo Simulations of the Half-Filled Two-Dimensional Kondo Lattice Model". In: *Physical Review Letters* 83 (1999), 796–799. DOI: 10.1103/PhysRevLett.83.796.

[10] M. W. Aulbach, F. F. Assaad, and M. Potthoff. "Dynamical mean-field study of partial Kondo screening in the periodic Anderson model on the triangular lattice". In: *Physical Review B* 92 (2015), 235131. DOI: 10.1103/PhysRevB.92.235131.

[11] R. Ballou. "Geometric frustration in Rare Earth antiferromagnetic compounds". In: *Journal of Alloys and Compounds* 275-277 (1998), 510–517. DOI: 10/fj7vpt.

[12] S. E. Barnes. "New method for the Anderson model". In: *Journal of Physics F: Metal Physics* 6 (1976), 1375–1383. DOI: 10/bjxx8h.

[13] S. E. Barnes. "New method for the Anderson model. II. The $U = 0$ limit". In: *Journal of Physics F: Metal Physics* 7 (1977), 2637–2647. DOI: 10/d5rn92.

[14] J. G. Bednorz and K. A. Müller. "Possible High T_c Superconductivity in the Ba-La-Cu-O system". In: *Zeitschrift für Physik B Condensed Matter* 64 (1986), 189–193. DOI: 10.1007/BF01303701.

[15] M. Bercx and F. F. Assaad. "Metamagnetism and Lifshitz transitions in models for heavy fermions". In: *Physical Review B* 86 (2012), 075108. DOI: 10.1103/PhysRevB.86.075108.

[16] B. Bernu, C. Lhuillier, and L. Pierre. "Signature of Néel order in exact spectra of quantum antiferromagnets on finite lattices". In: *Physical Review Letters* 69 (1992), 2590–2593. DOI: 10.1103/PhysRevLett.69.2590.

[17] B. Bernu et al. "Exact spectra, spin susceptibilities, and order parameter of the quantum Heisenberg antiferromagnet on the triangular lattice". In: *Physical Review B* 50 (1994), 10048–10062. DOI: 10.1103/PhysRevB.50.10048.

[18] J. H. de Boer and E. J. W. Verwey. "Semi-conductors with partially and with completely filled 3d-lattice bands". In: *Proceedings of the Physical Society* 49 (1937), 59–71. DOI: 10/fsftj5.

[19] J. Bünemann, F. Gebhard, and W. Weber. "Gutzwiller-correlated wave functions for degenerate bands: exact results in infinite dimensions". In: *Journal of Physics: Condensed Matter* 9 (1997), 7343–7358. DOI: 10.1088/0953-8984/9/35/009.

[20] J. Bünemann et al. "Numerical minimisation of Gutzwiller energy functionals". In: *Physica Status Solidi B* 249 (2012), 1282–1291. DOI: 10.1002/pssb.201147585.

[21] L. Capriotti, A. E. Trumper, and S. Sorella. "Long-Range Néel Order in the Triangular Heisenberg Model". In: *Physical Review Letters* 82 (1999), 3899–3902. DOI: 10.1103/PhysRevLett.82.3899.

[22] D. Ceperley, G. V. Chester, and M. H. Kalos. "Monte Carlo simulation of a many-fermion study". In: *Physical Review B* 16 (1977), 3081–3099. DOI: 10.1103/PhysRevB.16.3081.

[23] A. M. Clogston et al. "Local Magnetic Moment Associated with an Iron Atom Dissolved in Various Transition Metal Alloys". In: *Physical Review* 125 (1962), 541–552. DOI: 10.1103/PhysRev.125.541.

[24] P. Coleman. "Heavy Fermions: Electrons at the Edge of Magnetism". In: *Handbook of Magnetism and Advanced Magnetic Materials*. John Wiley & Sons, Ltd, 2007. DOI: 10/bmtkvs.

[25] L. N. Cooper. "Bound Electron Pairs in a Degenerate Fermi Gas". In: *Physical Review* 104 (1956), 1189–1190. DOI: 10.1103/PhysRev.104.1189.

[26] W. S. Corak et al. In: *Physical Review* 98 (1955), 1699–1707. DOI: 10.1103/PhysRev.98.1699.

[27] N. Costa, J. Lima, and R. R. dos Santos. "Spiral magnetic phases on the Kondo Lattice Model: A Hartree–Fock approach". In: *Journal of Magnetism and Magnetic Materials* 423 (2017), 74–83. DOI: 10.1016/j.jmmm.2016.09.061.

[28] R. Daou, C. Bergemann, and S. R. Julian. "Continuous Evolution of the Fermi Surface of $CeRu_2Si_2$ across the Metamagnetic Transition". In: *Physical Review Letters* 96 (2006), 026401. DOI: 10.1103/PhysRevLett.96.026401.

[29] W. de Haas, J. de Boer, and G. van dën Berg. "The electrical resistance of gold, copper and lead at low temperatures". In: *Physica* 1 (1934), 1115–1124. DOI: 10/df2ggp.

[30] M. Deppe et al. "Pronounced first-order metamagnetic transition in the paramagnetic heavy-fermion system CeTiGe". In: *Physical Review B* 85 (2012), 060401. DOI: 10.1103/PhysRevB.85.060401.

[31] S. Doniach. "The Kondo lattice and weak antiferromagnetism". In: *Physica B+C* 91 (1977), 231–234. DOI: 10/cknqgd.

[32] R. Eder. "Quasiparticle band structure and spin excitation spectrum of the Kondo lattice". In: *Physical Review B* 99 (2019), 085134. DOI: 10.1103/PhysRevB.99.085134.

[33] R. Eder, K. Grube, and P. Wróbel. "Antiferromagnetic phases of the Kondo lattice". In: *Physical Review B* 93 (2016), 165111. DOI: 10.1103/PhysRevB.93.165111.

[34] R. Eder, O. Rogojanu, and G. Sawatzky. "Many-body band structure and Fermi surface of the Kondo lattice". In: *Physical Review B* 58 (1998), 7599–7611. DOI: 10.1103/PhysRevB.58.7599.

[35] R. Eder, O. Stoica, and G. A. Sawatzky. "Single-particle excitations of the Kondo lattice". In: *Physical Review B* 55 (1997), R6109–R6112. DOI: 10.1103/PhysRevB.55.R6109.

[36] M. Fabrizio. "Gutzwiller description of non-magnetic Mott insulators: Dimer lattice model". In: *Physical Review B* 76 (2007), 165110. DOI: 10.1103/PhysRevB.76.165110.

[37] T. Fujita et al. "Specific heat of the dense Kondo compound $CeCu_6$". In: *Journal of Magnetism and Magnetic Materials* 47-48 (1985), 66–68. DOI: 10/c5wxk9.

[38] F. Gebhard. "Gutzwiller correlated wave functions in finite dimensions d: A systematic expansion in $1/d$". In: *Physical Review B* 41 (1990), 9452–9473. DOI: 10.1103/PhysRevB.41.9452.

[39] S. K. Goh et al. "Fermi-Surface Reconstruction in $CeRh_{1-x}Co_xIn_5$". In: *Physical Review Letters* 101 (2008), 056402. DOI: 10.1103/PhysRevLett.101.056402.

[40] M. C. Gutzwiller. "Effect of Correlation on the Ferromagnetism of Transition Metals". In: *Physical Review Letters* 10 (1963), 159–162. DOI: 10.1103/PhysRevLett.10.159.

[41] P. Haen et al. "Metamagnetic-like transition in $CeRu_2Si_2$?" In: *Journal of Low Temperature Physics* 67 (1987), 391–419. DOI: 10.1007/BF00710351.

[42] D. Hall et al. "Electronic structure of $CeRhIn_5$: de Haas–van Alphen and energy band calculations". In: *Physical Review B* 64 (2001), 064506. DOI: 10.1103/PhysRevB.64.064506.

[43] S. Hayami, M. Udagawa, and Y. Motome. "Partial Disorder in the Periodic Anderson Model on a Triangular Lattice". In: *Journal of the Physical Society of Japan* 80 (2011), 073704. DOI: 10.1143/JPSJ.80.073704.

[44] S. Hayami, M. Udagawa, and Y. Motome. "Carrier doping to a partially disordered state in the periodic Anderson model on a triangular lattice". In: *Journal of Physics: Conference Series* 400 (2012), 032018. DOI: 10/jpcv.

[45] S. Hayami, M. Udagawa, and Y. Motome. "Partial Disorder and Metal–Insulator Transition in the Periodic Anderson Model on a Triangular Lattice". In: *Journal of the Physical Society of Japan* 81 (2012), 103707. DOI: 10.1143/JPSJ.81.103707.

[46] H. Hegger et al. "Pressure-Induced Superconductivity in Quasi-2D $CeRhIn_5$". In: *Physical Review Letters* 84 (2000), 4986–4989. DOI: 10.1103/PhysRevLett.84.4986.

[47] A. C. Hewson. *The Kondo problem to heavy fermions*. Cambridge University Press, 1993.

[48] J. E. Hirsch and R. M. Fye. "Monte Carlo Method for Magnetic Impurities in Metals". In: *Physical Review Letters* 56 (1986), 2521–2524. DOI: 10.1103/PhysRevLett.56.2521.

[49] J. Hornung et al. "Anomalous quantum oscillations of $CeCoIn_5$ in high magnetic fields". In: *Physical Review B* 104 (2021), 235155. DOI: 10.1103/PhysRevB.104.235155.

[50] J. Hubbard. "Electron correlations in narrow energy bands". In: *Proceedings of the Royal Society of London A* 276 (1963), 238–257. DOI: 10.1098/rspa.1963.0204.

[51] M. Jarrell. "Hubbard model in infinite dimensions: A quantum Monte Carlo study". In: *Physical Review Letters* 69 (1992), 168–171. DOI: 10.1103/PhysRevLett.69.168.

[52] S. G. Johnson. *The NLopt nonlinear-optimization package*. 2011. URL: http://ab-initio.mit.edu/nlopt.

[53] C. Jurecka and W. Brenig. "Bond-operator mean-field theory of the half-filled Kondo lattice model". In: *Physical Review B* 64 (2001), 092406. DOI: 10.1103/PhysRevB.64.092406.

[54] K. Kamioka et al. "NMR studies of CePdAl below 1K". In: *Physica B: Condensed Matter* 259-261 (1999), 121–122. DOI: 10/dgbjtt.

[55] T. Kasuya. "A Theory of Metallic Ferro- and Antiferromagnetism on Zener's Model". In: *Progress of Theoretical Physics* 16 (1956), 45–57. DOI: 10.1143/PTP.16.45.

[56] M. Keßler and R. Eder. "Magnetic phases of the triangular Kondo lattice". In: *Physical Review B* 102 (2020), 235125. DOI: 10.1103/PhysRevB.102.235125.

[57] M. Keßler and R. Eder. "Combining bond particles with the Gutzwiller approximation: A variational theory of the Kondo lattice". In: *Physical Review B* 106 (2022), 045122. DOI: 10.1103/PhysRevB.106.045122.

[58] G. Knebel et al. "Phase diagram of $CeCu_2(Si_{1-x}Ge_x)_2$". In: *Physical Review B* 53 (1996), 11586–11592. DOI: 10.1103/PhysRevB.53.11586.

[59] G. Knopp et al. "Magnetic order in a Kondo lattice: A neutron scattering study of $CeCu_2Ge_2$". In: *Zeitschrift für Physik B Condensed Matter* 77 (1989), 95–104. DOI: 10.1007/BF01313625.

[60] J. Kondo. "Resistance Minimum in Dilute Magnetic Alloys". In: *Progress of Theoretical Physics* 32 (1964), 37–49. DOI: 10.1143/PTP.32.37.

[61] T. Koopmans. "Über die Zuordnung von Wellenfunktionen und Eigenwerten zu den Einzelnen Elektronen Eines Atoms". In: *Physica* 1 (1934), 104–113. DOI: 10/dd5bdj.

[62] G. Kotliar and A. E. Ruckenstein. "New Functional Integral Approach to Strongly Correlated Fermi Systems: The Gutzwiller Approximation as a Saddle Point". In: *Physical Review Letters* 57 (1986), 1362–1365. DOI: 10.1103/PhysRevLett.57.1362.

[63] P. Kratzer and J. Neugebauer. "The Basics of Electronic Structure Theory for Periodic Systems". In: *Frontiers in Chemistry* 7 (2019). DOI: 10.3389/fchem.2019.00106.

[64] K. Kubo. "Ferromagnetism and Fermi surface transition in the periodic Anderson model: Second-order phase transition without symmetry breaking". In: *Physical Review B* 87 (2013), 195127. DOI: 10.1103/PhysRevB.87.195127.

[65] C. Lacroix. "Some exact results for the Kondo lattice with infinite exchange interaction". In: *Solid State Communications* 54 (1985), 991–994. DOI: 10/dmkzfp.

[66] C. Lacroix, B. Canals, and M. D. Núñez-Regueiro. "Kondo Screening and Magnetic Ordering in Frustrated UNi_4B". In: *Physical Review Letters* 77 (1996), 5126–5129. DOI: 10.1103/PhysRevLett.77.5126.

[67] C. Lacroix. "Frustrated Metallic Systems: A Review of Some Peculiar Behavior". In: *Journal of the Physical Society of Japan* 79 (2010), 011008. DOI: 10.1143/JPSJ.79.011008.

[68] N. Lanatà, P. Barone, and M. Fabrizio. "Fermi-surface evolution across the magnetic phase transition in the Kondo lattice model". In: *Physical Review B* 78 (2008), 155127. DOI: 10.1103/PhysRevB.78.155127.

[69] N. Lanatà et al. "Efficient implementation of the Gutzwiller variational method". In: *Physical Review B* 85 (2012), 035133. DOI: 10.1103/PhysRevB.85.035133.

[70] B. K. Lee et al. "Magnetic ordering in frustrated $Ce_5Ni_2Si_3$". In: *Physical Review B* 70 (2004), 224409. DOI: 10.1103/PhysRevB.70.224409.

[71] S. Lucas et al. "Entropy Evolution in the Magnetic Phases of Partially Frustrated CePdAl". In: *Physical Review Letters* 118 (2017), 107204. DOI: 10.1103/PhysRevLett.118.107204.

[72] J. M. Luttinger. "Fermi Surface and Some Simple Equilibrium Properties of a System of Interacting Fermions". In: *Physical Review* 119 (1960), 1153–1163. DOI: 10.1103/PhysRev.119.1153.

[73] J. M. Luttinger and J. C. Ward. "Ground-State Energy of a Many-Fermion System. II". In: *Physical Review* 118 (1960), 1417–1427. DOI: 10.1103/PhysRev.118.1417.

[74] D. van der Marel and G. A. Sawatzky. "Electron-electron interaction and localization in d and f transition metals". In: *Physical Review B* 37 (1988), 10674–10684. DOI: 10.1103/PhysRevB.37.10674.

[75] I. Martin and C. D. Batista. "Itinerant Electron-Driven Chiral Magnetic Ordering and Spontaneous Quantum Hall Effect in Triangular Lattice Models". In: *Physical Review Letters* 101 (2008), 156402. DOI: 10.1103/PhysRevLett.101.156402.

[76] L. C. Martin and F. F. Assaad. "Evolution of the Fermi Surface across a Magnetic Order-Disorder Transition in the Two-Dimensional Kondo Lattice Model: A Dynamical Cluster Approach". In: *Physical Review Letters* 101 (2008), 066404. DOI: 10.1103/PhysRevLett.101.066404.

[77] L. C. Martin, M. Bercx, and F. F. Assaad. "Fermi surface topology of the two-dimensional Kondo lattice model: Dynamical cluster approximation approach". In: *Physical Review B* 82 (2010), 245105. DOI: 10.1103/PhysRevB.82.245105.

[78] S. A. M. Mentink et al. "Magnetic Ordering and Frustration in Hexagonal UNi_4B". In: *Physical Review Letters* 73 (1994), 1031–1034. DOI: 10.1103/PhysRevLett.73.1031.

[79] W. Metzner and D. Vollhardt. "Analytic calculation of ground-state properties of correlated fermions with the Gutzwiller wave function". In: *Physical Review B* 37 (1988), 7382–7399. DOI: 10.1103/PhysRevB.37.7382.

[80] J. J. Moré, B. S. Garbow, and K. E. Hillstrom. *User guide for MINPACK-1*. Tech. rep. Argonne National Laboratory, 1980. URL: https://cds.cern.ch/record/126569.

[81] Y. Motome et al. "Partial Kondo Screening in Frustrated Kondo Lattice Systems". In: *Physical Review Letters* 105 (2010), 036403. DOI: 10.1103/PhysRevLett.105.036403.

[82] R. Movshovich et al. "Second Low-Temperature Phase Transition in Frustrated UNi_4B". In: *Physical Review Letters* 83 (1999), 2065–2068. DOI: 10.1103/PhysRevLett.83.2065.

[83] Y. Nagaoka. "Ferromagnetism in a Narrow, Almost Half-Filled s Band". In: *Physical Review* 147 (1966), 392–405. DOI: 10.1103/PhysRev.147.392.

[84] J. W. Negele and H. Orland. *Quantum Many-Particle Systems*. Westview Press, 1988.

[85] K. Noda et al. "Partial Kondo Screening in a Geometrically Frustrated Heavy Electron System". In: *Proceedings of the International Conference on Strongly Correlated Electron Systems (SCES2013)*. DOI: 10.7566/JPSCP.3.014019.

[86] M. Núñez-Regueiro, C. Lacroix, and B. Canals. "Magnetic ordering in the frustrated Kondo lattice compound CePdAl". In: *Physica C: Superconductivity* 282-287 (1997), 1885–1886. DOI: 10/fvg5m4.

[87] N. Oeschler et al. "Magnetic phase diagram of $CeCu_2(Si_{1-x}Ge_x)_2$ measured with low-temperature thermal expansion". In: *Physical Review B* 71 (2005), 094409. DOI: 10.1103/PhysRevB.71.094409.

[88] Y. Ōnuki et al. "Kondo Lattice Formation in $Ce_xLa_{1-x}Cu_6$". In: *Journal of the Physical Society of Japan* 54 (1985), 1964–1974. DOI: 10.1143/JPSJ.54.1964.

[89] M. Oshikawa. "Topological Approach to Luttinger's Theorem and the Fermi Surface of a Kondo Lattice". In: *Physical Review Letters* 84 (2000), 3370–3373. DOI: 10.1103/PhysRevLett.84.3370.

[90] A. Oyamada et al. "NMR studies of the partially disordered state in a triangular antiferromagnet UNi_4B". In: *Journal of Physics: Condensed Matter* 19 (2007), 145246. DOI: 10/brk72f.

[91] A. K. Pankratova, P. A. Igoshev, and V. Y. Irkhin. "Incommensurate magnetic order in rare earth and transition metal compounds with local moments". In: *Journal of Physics: Condensed Matter* 33 (2021), 375802. DOI: 10/jpcw.

[92] R. Peters and N. Kawakami. "Ferromagnetic state in the one-dimensional Kondo lattice model". In: *Physical Review B* 86 (2012), 165107. DOI: 10.1103/PhysRevB.86.165107.

[93] R. Peters and N. Kawakami. "Large and small Fermi-surface spin density waves in the Kondo lattice model". In: *Physical Review B* 92 (2015), 075103. DOI: 10.1103/PhysRevB.92.075103.

[94] R. Peters and N. Kawakami. "Competition of striped magnetic order and partial Kondo screened state in the Kondo lattice model". In: *Physical Review B* 96 (2017), 115158. DOI: 10.1103/PhysRevB.96.115158.

[95] R. Peters, N. Kawakami, and T. Pruschke. "Spin-Selective Kondo Insulator: Cooperation of Ferromagnetism and the Kondo Effect". In: *Physical Review Letters* 108 (2012), 086402. DOI: 10.1103/PhysRevLett.108.086402.

[96] H. Pfau et al. "Thermoelectric transport across the metamagnetic transition of $CeRu_2Si_2$". In: *Physical Review B* 85 (2012), 035127. DOI: 10.1103/PhysRevB.85.035127.

[97] M. J. Powell. *The BOBYQA algorithm for bound constrained optimization without derivatives*. Tech. rep. Department of Applied Mathematics and Theoretical Physics, University of Cambridge, 2009. URL: https://www.damtp.cam.ac.uk/user/na/NA_papers/NA2009_06.pdf.

[98] M. A. Ruderman and C. Kittel. "Indirect Exchange Coupling of Nuclear Magnetic Moments by Conduction Electrons". In: *Physical Review* 96 (1954), 99–102. DOI: 10.1103/PhysRev.96.99.

[99] M. P. Sarachik, E. Corenzwit, and L. D. Longinotti. "Resistivity of Mo-Nb and Mo-Re Alloys Containing 1% Fe". In: *Physical Review* 135 (1964), A1041–A1045. DOI: 10.1103/PhysRev.135.A1041.

[100] J. R. Schrieffer and P. A. Wolff. "Relation between the Anderson and Kondo Hamiltonians". In: *Physical Review* 149 (1966), 491–492. DOI: 10.1103/PhysRev.149.491.

[101] H. Shishido et al. "Fermi Surface, Magnetic and Superconducting Properties of $LaRhIn_5$ and $CeTIn_5$ (T: Co and Rh)". In: *Journal of the Physical Society of Japan* 71 (2002), 276–278. DOI: 10.1143/JPSJS.71S.276.

[102] H. Shishido et al. "A Drastic Change of the Fermi Surface at a Critical Pressure in $CeRhIn_5$: dHvA Study under Pressure". In: *Journal of the Physical Society of Japan* 74 (2005), 1103–1106. DOI: 10.1143/JPSJ.74.1103.

[103] M. Sigrist et al. "Ferromagnetism in the strong-coupling regime of the one-dimensional Kondo-lattice model". In: *Physical Review B* 46 (1992), 13838–13846. DOI: 10.1103/PhysRevB.46.13838.

[104] G. R. Stewart. "Heavy-fermion systems". In: *Reviews of Modern Physics* 56 (1984), 755–787. DOI: 10.1103/RevModPhys.56.755.

[105] O. Stockert et al. "Nature of the *A* Phase in $CeCu_2Si_2$". In: *Physical Review Letters* 92 (2004), 136401. DOI: 10.1103/PhysRevLett.92.136401.

[106] H. U. R. Strand. "Correlated Materials – Models & Methods". PhD thesis. University of Gothenburg, 2013. URL: http://hdl.handle.net/2077/32118.

[107] A. Sumiyama et al. "Coherent Kondo State in a Dense Kondo Substance: CexLa1-xCu6". In: *Journal of the Physical Society of Japan* 55 (1986), 1294–1304. DOI: 10.1143/JPSJ.55.1294.

[108] A. M. Tsvelick and P. B. Wiegmann. "Exact results in the theory of magnetic alloys". In: *Advances in Physics* 32 (1983), 453–713. DOI: 10/bws5v8.

[109] S. Viola Kusminskiy et al. "Mean-field study of the heavy-fermion metamagnetic transition". In: *Physical Review B* 77 (2008), 094419. DOI: 10.1103/PhysRevB.77.094419.

[110] P. Wagner, P. Wróbel, and R. Eder. "Ferromagnetism in the Kondo-lattice". In: *The European Physical Journal B* 93 (2020), 58. DOI: 10.1140/epjb/e2020-100549-0.

[111] H. Watanabe and M. Ogata. "Fermi-Surface Reconstruction without Breakdown of Kondo Screening at the Quantum Critical Point". In: *Physical Review Letters* 99 (2007), 136401. DOI: 10.1103/PhysRevLett.99.136401.

[112] G. C. Wick. "The Evaluation of the Collision Matrix". In: *Physical Review* 80 (1950), 268–272. DOI: 10.1103/PhysRev.80.268.

[113] A. S. Wills, R. Ballou, and C. Lacroix. "Model of localized highly frustrated ferromagnetism: The kagomé spin ice". In: *Physical Review B* 66 (2002), 144407. DOI: 10.1103/PhysRevB.66.144407.

[114] K. G. Wilson. "The renormalization group: Critical phenomena and the Kondo problem". In: *Reviews of Modern Physics* 47 (1975), 773–840. DOI: 10.1103/RevModPhys.47.773.

[115] Y. X. Yao et al. "Comparative study of the electronic and magnetic properties of $BaFe_2As_2$ and $BaMn_2As_2$ using the Gutzwiller approximation". In: *Physical Review B* 84 (2011), 245112. DOI: 10.1103/PhysRevB.84.245112.

[116] K. Yosida. "Magnetic Properties of Cu-Mn Alloys". In: *Physical Review* 106 (1957), 893–898. DOI: 10.1103/PhysRev.106.893.

[117] K. Yosida. "Bound State Due to the $s-d$ Exchange Interaction". In: *Physical Review* 147 (1966), 223–227. DOI: 10.1103/PhysRev.147.223.